

Copyright

by

Tianhao Yang

2020

**THE DISSERTATION COMMITTEE FOR TIANHAO YANG CERTIFIES THAT
THIS IS THE APPROVED VERSION OF THE FOLLOWING DISSERTATION:**

**RATE-DEPENDENT FRACTURE OF A SILICON/EPOXY
INTERFACE UNDER MIXED-MODE LOADING CONDITIONS**

Committee:

Kenneth M. Liechti, Supervisor

Rui Huang, Co-Supervisor

Krishnaswamy Ravi-Chandar

Gregory J. Rodin

Roger T. Bonnecaze

**RATE-DEPENDENT FRACTURE OF A SILICON/EPOXY INTERFACE UNDER
MIXED-MODE LOADING CONDITIONS**

by

Tianhao Yang

Dissertation

Presented to the Faculty of the Graduate School of

The University of Texas at Austin

in Partial Fulfillment

of the Requirements

for the Degree of

Doctor of Philosophy

The University of Texas at Austin

May 2020

DEDICATION

To my family, for their love and support.

Acknowledgements

On completion of this dissertation, thanks are owed to many people who have made this possible. First of all, I would like to express my deepest appreciation to my supervisor Dr. Kenneth Liechti for his invaluable suggestions and relentless support throughout my Ph.D. career. I would also like to extend my deepest gratitude to my co-supervisor Dr. Rui Huang, for his insightful guidance and discussions that inspire me significantly. My sincere gratitude is also due to other members of my dissertation committee: Dr. Krishnaswamy Ravi-Chandar, Dr. Gregory Rodin and Dr. Roger Bonnecaze. I want to thank them for their time and effort in reviewing my dissertation and the constructive advice during my defense.

The work in this dissertation was conducted with financial support from the National Science Foundation and Semiconductor Research Corporation. I would also like to acknowledge the partial support by the University of Texas at Austin.

I gratefully acknowledge the assistance of our technical staff: Joseph Pokluda, Steven Sanders, Pablo Cortez and Scott Messec, for their efficient work in tackling the technical issues in both experimental and computational facilities. Special thanks go to Joseph Pokluda for his help in the specimen preparation.

I want to thank Vatsa Gandhi for his contribution to the development of the dual-actuator loading device. I am also grateful to Xingwei Yang for his help in the implementation of the finite difference method. I am fortunate to work with the talented fellow graduate students in our department: Dr. Seung Ryul Na, Dr. Chenglin Wu, Dr. Daniel Ferreira, Dr. Peng Wang, Dr. Dongjie Jiang, Dr. Chenglin Yang, Dr. Shixuan Yang,

Dr. Shutao Qiao, Dr. Liu Wang, Dr. Zhaohe Dai, Yu-sheng Lo, Si Chen, Zhanrui Zhang, Hongrui Yu, Sivasakthya Mohan and Eui Seop Kim.

Finally, I want to say thank you from the bottom of my heart to my parents for their unwavering support throughout the years. This thesis is dedicated to my fiancée, Dr. Lingyu Zeng, for her sacrifice and endless love. Thank you for bringing out the best in me.

RATE-DEPENDENT FRACTURE OF A SILICON/EPOXY INTERFACE UNDER- MIXED MODE LOADING CONDITIONS

Tianhao Yang, Ph.D.

The University of Texas at Austin, 2020

Supervisor: Kenneth M. Liechti

Co-Supervisor: Rui Huang

Rate-dependent fracture has been observed for many polymer-based interfaces, where both the interfacial strength and adhesion energy (or fracture toughness) often increase with increasing separation rates, while the opposite trend typically defines the behavior of the bulk polymer. This dissertation mainly addresses the following two aspects: the characterization of the rate-dependent fracture for a silicon/epoxy interface under mixed-mode loading conditions, and the development of a multiscale, mechanism-based model for simulating rate-dependent fracture at interfaces.

First, nominally mode-I fracture experiments were conducted with double cantilever beam (DCB) specimens. Symmetric displacement control was enforced at the loading point, while the separation rate was varied in order to examine the rate dependence. A beam on elastic foundation (BEF) analysis was adopted for estimating the crack length

and J-integral. An iterative approach was used to extract the interfacial traction-separation relations (TSR), which exhibited a noticeable rate dependence as both the interfacial strength and fracture toughness increased with increasing separation rates. Motivated by this observation, a rate dependent cohesive zone model was developed, where the damage evolution within the cohesive zone is determined by a thermally activated bond rupture process. The rate-dependent cohesive zone model was implemented via a finite difference method to solve the DCB problem numerically. The model parameters were extracted by comparing the numerical results with measurements.

Next, to improve the modeling of the rate-dependent fracture, a multiscale mechanism-based approach was proposed to include the entropic effects of polymer chains and a nonlinear energy barrier for bond rupture. A rate-dependent cohesive zone model was developed from the bottom up at four levels: the bond level, the chain level, the interface level, and the specimen level. Bonds are described by a potential energy function (e.g., Lennard-Jones potential) with an equilibrium bond length and a bond energy. A series of bonds form a molecular chain, which is modeled as a freely jointed chain (FJC) with stretchable bonds. Then, with a large number of molecular chains at the interface level, the chain survival probability follows the thermally activated bond rupture kinetics with a microscopic time scale, leading to a rate-dependent damage process for the interface. Here, an interface with statistically distributed chain lengths is also considered. To compare with the fracture experiments at the specimen level, the interface model was implemented via a user-defined surface interaction subroutine (UINTER) in the finite element package ABAQUS for numerical simulations. With a few parameters extracted for the molecular

structures of the interface, the model was able to reproduce the rate-dependent fracture of the silicon/epoxy interface under mode-I conditions.

Finally, the rate-dependent fracture for the same interface was examined under mixed-mode loading conditions. A dual-actuator loading device was designed and developed to achieve a full range of the mode-mix with DCB specimens, where the two displacements at the loading end can be controlled independently. For each mode mix, the ratio of the end displacements between the upper and lower beams was kept a constant, while the rate effect was examined by varying the displacement rates proportionally. The nominal phase angle of mode mix at the initial crack tip was correlated to the displacement ratio based on the linear elastic fracture mechanics (LEFM) analysis. The balance condition was naturally satisfied via the symmetry of the specimen configuration (silicon/epoxy/silicon), so that the direct extraction of the crack-tip TSRs was made possible by a decoupled beam interaction analysis using only the far-field measurements including forces, displacements and rotations at the loading end of the specimen. The mixed-mode interfacial fracture was found to be rate dependent as both normal and shear components of the interfacial strength and toughness increased with increasing displacement rates. A BEF analysis with an extension for shear interactions was used to estimate the crack growth and the local separation rates in both the normal and tangential directions. It turned out that the local separation rates varied as damage evolved across the interface, thus leading to a locally history dependent fracture behavior. These findings underline the importance of the local separation rate and history on the interfacial properties and provide insights for further model developments.

Table of Contents

LIST OF TABLES.....	XIV
LIST OF FIGURES	XV
CHAPTER 1 INTRODUCTION.....	1
1.1 Interface mechanics	2
1.2 Mixed-mode fracture	5
1.3 Rate dependent fracture	7
1.4 Bond rupture kinetics.....	9
1.5 Research scope.....	11
CHAPTER 2 MODE-I RATE-DEPENDENT INTERFACIAL FRACTURE	13
2.1 Double cantilever beam (DCB) experiment	13
2.1.1 Material properties	13
2.1.2 Experimental procedures	16
2.2 Analysis	17
2.2.1 Mode-mix analysis.....	18

2.2.2	Beam on elastic foundation analysis.....	20
2.2.3	Bilinear traction-separation relations by iterative method.....	23
2.2.4	A kinetic bond rupture model	26
2.2.5	A rate-dependent DCB model.....	30
2.3	Results and Discussion	38
2.4	Summary	50
CHAPTER 3 A MULTISCALE MECHANISM-BASED MODEL FOR RATE-DEPENDENT INTERFACIAL FRACTURE		53
3.1	Bond level: Lennard-Jones potential	54
3.2	Chain level: A modified freely jointed chain model.....	56
3.3	Interface level: Thermally activated damage process.....	60
3.4	Effect of statistically distributed chain lengths.....	71
3.5	Specimen level: Mode-I fracture of a silicon/epoxy interface.....	76
3.6	Summary	88
CHAPTER 4 MIXED-MODE RATE DEPENDENT INTERFACIAL FRACTURE		90
4.1	Design of Experiment	90

4.1.1	Dual-actuator loading device	91
4.1.2	Specimen preparation.....	94
4.2	Analysis	94
4.2.1	Critical load envelopes.....	95
4.2.2	Mode mix analysis	98
4.2.3	Crack tip displacements and J-integrals.....	101
4.3	Results and Discussion	102
4.3.1	Direct measurements and crack tip traction-separation relations	103
4.3.2	Loading rate effect	110
4.3.3	Global rate vs local rate	113
4.3.4	Loading mode effect	116
4.3.5	Finite element validation.....	122
4.3.6	A simple extension of the rate-dependent cohesive zone model	126
4.4	Summary	127

CHAPTER 5	CONCLUSIONS AND FUTURE WORK.....	130
APPENDIX A: BEAM ON ELASTIC FOUNDATION MODEL		135
APPENDIX B: A FINITE DIFFERENCE IMPLEMENTATION OF BOND RUPTURE KINEMATICS IN A DCB SPECIMEN.....		141
APPENDIX C: A FINITE ELEMENT IMPLEMENTATION OF THE MULTISCALE RATE- DEPENDENT COHESIVE ZONE MODEL		144
APPENDIX D: USER-DEFINED INTERFACE SUBROUTINE (UINTER).....		146
REFERENCES.....		150
VITA		160

List of Tables

Table 2.1 Mode mix of DCB specimens with different epoxy thickness	19
Table 2.2 Values of the rate-dependent properties of the silicon/epoxy interface associated with the bilinear traction-separation relations obtained from the BEF analysis	44
Table 2.3 Values of the parameters for the silicon/epoxy interface associated with the rate-dependent cohesive zone model	45
Table 3.1 Parameters used in the model at different separation rates.....	78
Table 3.2 Model parameters determined and used in numerical simulations.....	85
Table 4.1 Actuator specifications and property descriptions.....	93
Table 4.2 Relevant specimen geometry and materials properties.....	93
Table 4.3 Loading configurations and corresponding mode angle (estimated by LEFM)	100
Table 4.4 Stiffness of the elastic foundation in normal and tangential directions	110
Table 4.5 Interfacial stiffness in the normal and tangential directions	117

List of Figures

Figure 1.1 Selective transfer of graphene using rate effects of graphene/epoxy interface [2].	2
Figure 1.2 Fracture energies as a function of induced loading rate [109].	9
Figure 1.3 Schematic of a polymer chain lying across the plane of crack propagation [112].	9
Figure 2.1 Stress-strain behavior of EP30 characterized by a uniaxial tension test: (a) loading-unloading-reloading curve; (b) at different strain rates.	15
Figure 2.2 Stress-strain behavior of EP30 characterized by an Arcan shear test under multiple strain rates.	15
Figure 2.3 Schematic of a DCB specimen and loading tabs.	16
Figure 2.4 Load-displacement curves of two specimens with the same initial crack length, one with the Au/Pd coating for a sharp initial crack and the other without a coating.	17
Figure 2.5 (a) Measured load-displacement response for a DCB specimen, with the initial linear portion fitted by Eq. (2.2) using the measured initial crack length and the stiffness of the elastic foundation. (b) Crack length determined by Eq. (2.3) versus the applied displacement; (c) J-integral by Eq. (2.4) versus the applied displacement; (d) The fracture resistance curve.	22
Figure 2.6 Schematic of a bilinear traction-separation relation.	24

Figure 2.7 Comparisons between load-displacement curves from finite element solutions and experimental data. (a) The descending portion varies with the fracture toughness; (b) The response near the peak force varies with the strength of the interface.....	25
Figure 2.8 (a) Normalized traction-separation relations and (b) damage evolution, for different local separation rates; (c) Rate-dependent fracture toughness and strength predicted by the kinetic model; (d) Effect of the normalized bond energy on the traction-separation relation.....	28
Figure 2.9 (a) Schematics of a symmetric DCB specimen; (b) Deflection of one beam with tractions ahead of the crack tip.	31
Figure 2.10 Numerical results from the rate-dependent DCB model: (a) load-time response; (b) crack-tip opening displacement; (c) damage parameters along the interface at different times; (d) crack growth; (e) traction-separation relations at different locations along the interface; (f) normalized J-integral versus the change of crack length as the fracture resistance curve obtained by equations (2.26) and (2.27).....	37
Figure 2.11 (a) Damage evolution and (b) normal traction distributions along the interface with the origin at the crack tip as the crack grows.....	38
Figure 2.12 Effect of (a) the critical stress and (b) the bond energy on the load-displacement responses of DCB specimens by the rate-dependent DCB model.....	38

Figure 2.13 The load-displacement responses of all specimens, comparing the experimental data (markers) and the numerical results by the rate-dependent DCB model (lines): (a-e) DCB specimens with five applied separation rates: 0.042 mm/s, 0.42 mm/s, 2.1 mm/s, 4.2 mm/s, and 8.4 mm/s.....	46
Figure 2.14 (a) Load-displacement curves of five specimens with different separation rates, symbols for the measured data and solid lines for the numerical results obtained by the rate-dependent DCB model; (b) Resistance curves for different separation rates by the BEF analysis. Rate dependence of (c) steady-state fracture toughness and (d) interfacial strength obtained by the three methods (the BEF results were averaged over all specimens at each separation rate with error bars showing the standard deviations). (e) Bilinear traction-separation relations obtained by the iterative method; (f) Crack tip traction-separation relations obtained by the rate-dependent DCB model.	47
Figure 2.15 Plot the effects of epoxy thickness on the extracted stiffness (K_0), steady-state toughness (Γ_{ss}), and strength (σ_0) from the BEF analysis. Evidently, the epoxy thickness has little effect on the extracted properties. On the other hand, the toughness and strength are both rate dependent, whereas the stiffness is rate independent.	48
Figure 2.16 The load-displacement responses of five specimens at different applied separation rates, comparing the experimental data (markers) and the numerical results by the iterative method (lines).....	49

Figure 2.17 The critical stress of the interface versus the local separation rate for all specimens.....	49
Figure 2.18 (a) Steady-state fracture toughness and (b) interfacial strength obtained by the three methods, versus the local separation rates at the crack tip.....	50
Figure 3.1 Comparison of the LJ potential and two approximations: (a) the potential energy; (b) the bond force.....	55
Figure 3.2 Modified FJC model with the LJ potential for the bonds: (a) bond stretch versus chain stretch and (b) end force versus chain stretch.	59
Figure 3.3 Modified FJC model with the logarithmic potential for the bonds: (a) bond stretch versus chain stretch and (b) end force versus chain stretch.	60
Figure 3.4 (a) Normalized free energy of a chain ($\bar{\varepsilon} = 10$ and $n = 50$) subject to various forces; (b) Normalized energy barrier as a function of the normalized force at various values of the normalized bond energy.	62
Figure 3.5 (a) Damage evolution and (b) normalized separation over time under constant tractions for $\bar{\varepsilon} = 50$	67
Figure 3.6 Predicted time to failure versus the normalized traction for different values of the bond energy ($\bar{\varepsilon} = 10, 30, 50$).....	67
Figure 3.7 Predicted damage evolution and traction-separation relations under constant separation rates with $\bar{\varepsilon} = 50$. (a-b) for relatively low separation rates, and (c-d) for relatively high separation rates. The dotted lines in (b) and (d) are for the linear Gaussian chain model with $\bar{\sigma} = 3\bar{\delta}$, and the dashed lines are for the nonlinear Langevin model with: $\bar{\sigma} = \mathcal{L}^{-1}(\bar{\delta})$, both independent of the separation rate with no damage ($D = 0$).....	69

Figure 3.8 (a) Normalized strength and (b) toughness versus the normalized separation rate at different values of the normalized bond energy.....71

Figure 3.9 Normalized traction-separation relations (a-b), chain length distributions (c-d), and damage evolution (e-f) under a constant separation rate. (a,c,e) for a relatively low separation rate, while (b,d,f) for a high separation rate.75

Figure 3.10 Effects of the relative deviation in statistically distributed chain lengths on the predicted interfacial properties: (a) the initial stiffness, (b) the strength, and (c) the toughness, all normalized with respect to the corresponding properties for a constant chain length ($\bar{\chi} = 0$).....76

Figure 3.11 Schematic of a double cantilever beam (DCB) specimen, direct measurements including forces, displacements and rotations at the loading end.....77

Figure 3.12 (a) Force-displacement curves under different separation rates (measurements in symbols and simulations in solid lines); (b) CTOD versus the end displacement (symbols by Eq. (6.1) and solid lines by simulations); (c) J-integral versus CTOD (data fitted by functions plotted as dashed lines); (d) Extracted crack tip traction-separation relations.81

Figure 3.13 (a) Correlation between the normalized toughness and strength predicted by the model, intersecting the dashed line with $\bar{\Gamma}/\bar{\sigma}_p^2 = 0.25$ for one specimen ($\dot{\Delta} = 0.625$ mm/s); (b) Comparison of the force-displacement curves from experiment ($\dot{\Delta} = 0.625$ mm/s) and numerical simulations with different deviations of the chain lengths.....83

Figure 3.14 (a) Traction-separation relations at the initial crack tip; (b) Steady-state traction-separation relations; (c) Resistance curve obtained by Eq. (3.34)	86
Figure 3.15 Rate-dependent fracture toughness (a) and strength (b) of the silicon/epoxy interface predicted by the model, in comparison with the values extracted directly from the DCB experiments (Table 3.1) and from the previous work [139].	87
Figure 3.16 Schematic of the multiscale rate-dependent cohesive zone model.	88
Figure 4.1 (a) Dual-Actuator Loading Device; (b) Specimen grips and installation; (c) An image of the DIC target taken by the camera during the experiment.	91
Figure 4.2 Loading configurations and free-body diagrams of the laminated beam (epoxy layer neglected).	96
Figure 4.3 (a) Critical load envelope and (b) displacement envelope for different fracture toughness ratios (mode I fracture toughness assumed: 10 J/m ²)	98
Figure 4.4 (a) Mode angle as a function of crack length (dotted lines obtained by beam theory and symbols obtained by LEFM analysis that included the epoxy); (b) Mode angle as a function of the prescribed displacement ratio ($a_0/L = 0.33$).	100
Figure 4.5 For both upper and lower beams: (a) Applied normal displacements compared with DIC measurements at the loading points; (b) Reaction forces at the loading points; (c) Tangential displacements obtained by DIC; (d) Rotations obtained by DIC. (For figures b-d, data are denoted by symbols and finite element results are denoted by dashed lines).	104

Figure 4.6 (a) Force difference (\tilde{P}) versus the normal separation ($\tilde{\Delta}$) at the loading point (red dashed line obtained by Eq. (A.16), blue dashed line obtained by FEM); (b) Force combination (\bar{P}) versus the tangential separation (\tilde{U}) at the loading point (red dashed line obtained by Eq. (A.19), blue dashed line obtained by FEM); (c) Crack lengths estimated by Eq. (A.16) and Eq. (A.19) (dashed line labeling $a_t = a_n$); (d) A comparison for J_1 obtained by Eq. (4.13) and Eq. (4.17).....	106
Figure 4.7 (a) Variation of J-integral components with applied displacement; (b) Resistance curve.....	107
Figure 4.8 (a) J-integrals plotted versus the (initial) crack tip separations; (b) Crack tip traction-separation relations.....	108
Figure 4.9 The variation in mode angle as the cohesive zone develops, based on beam theory (BT), LEFM, J-integral (Eq. (4.2)) and crack tip displacements (Eq. (4.19)).....	109
Figure 4.10 Resistance curves for specimens tested at different applied displacement rates.....	112
Figure 4.11 (a) Normal and (b) shear components of the traction-separation relations at the initial crack tip.	112
Figure 4.12 Crack tip mode angle at different applied displacement rates, (a) comparing mode angle measures at the initial crack length and (b) the effect of applied displacement rate on mode angle, based on J-integral and crack tip displacements, as the cohesive zone develops.....	113

Figure 4.13 (a) Crack tip vectorial separation rate and its normal and shear components;
(b) Toughness ($J = J_1 + J_2$) versus local separation rate ($\dot{\delta}^* = \sqrt{\dot{\delta}_n^2 + \dot{\delta}_t^2}$)
at five displacement rates; (c) Steady state toughness (Γ_{ss}) versus the local
separation rate with the slopes labeled as $e_1 = 0.32$ for the two lower
rates, $e_2 = 0.072$ for the three higher rates.....115

Figure 4.14 (a) Average values and deviation of mode angles ($\Psi = \tan^{-1} \sqrt{J_2 / J_1}$)
obtained at the initial crack length compared with results from LEFM
(with epoxy) and beam theory analyses; (b) Variation in mode angles
during crack growth at five prescribed displacement ratios.118

Figure 4.15 For all specimens, double logarithmic plots of the initiation toughness
versus crack tip separation rate: (a) normal toughness versus normal rate,
(b) shear toughness versus tangential rate and (c) total toughness versus
vectorial rate (upper and lower bounds fitted by power law functions with
exponents labeled).119

Figure 4.16 Surface plots of (a) normal strength (σ_{n0}^*), (b) normal critical separation (δ_{nc}^*), (c) shear strength (σ_{t0}^*) and (d) tangential critical separation (δ_{tc}^*),
versus corresponding crack tip separation rates and mode angles.....121

Figure 4.17 Loading path by (a) J-integrals and (b) crack tip displacements, at five
prescribed displacement ratios with highest global rate.122

Figure 4.18 (a) Shear traction versus normal traction at the initial crack tip obtained by
FEM; (b) Equivalent stress by von Mises yield criterion and Tresca yield
criterion.125

Figure 4.19 Schematic of chains being stretched with an angle θ127

Chapter 1 Introduction

Interfaces abound in many technologically important applications that range from primary structural adhesively bonded joints in aerospace, naval and automotive structures to the multiple interfaces that are common in microelectronics devices. One potential failure mode in all these cases, no matter how general the loading conditions (multiaxial loading, loading rates, etc.) are or how much the environmental conditions (temperature, humidity, solvent concentration) may change, is interfacial delamination. To assure the durability of a system with interfaces, a thorough understanding of the fracture process at the interface is required.

As one out of the many features of the interface fracture, rate dependence is the main focus of this dissertation. The rate-dependent fracture of interfaces has been exploited for selective delamination in transfer printing [1] and dry transfer of graphene from its growth substrate to an epoxy [2, 3]. In both cases, an increase in the separation rate increased the interfacial toughness, but for different reasons. The transfer printing referred to made use of a polymer in its rubbery state and increasing the separation rate could be [4] and has been [5] linked to bulk viscoelastic processes. In contrast, the cited examples of dry transfer (Fig. 1.1) made use of a glassy polymer (epoxy) whose bulk fracture toughness decreases with increasing separation rate [6]. The increasing toughness associated with delamination between interfaces involving glassy polymers must therefore be attributed to the interfacial behavior of such polymers.

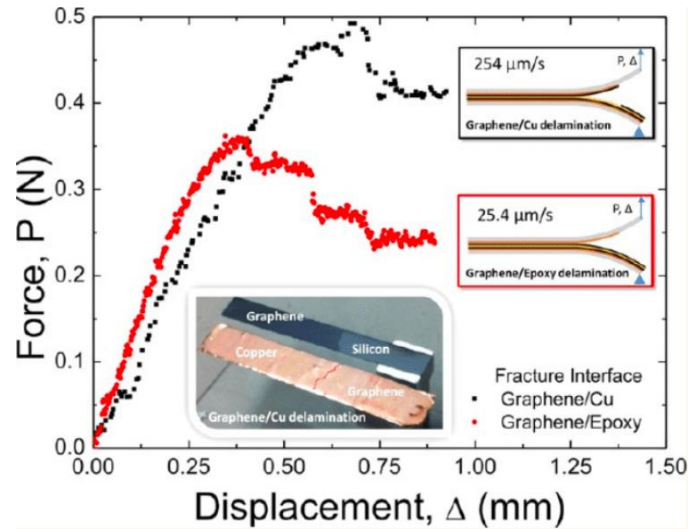


Figure 1.1 Selective transfer of graphene using rate effects of graphene/epoxy interface [2].

1.1 Interface mechanics

Delamination models were initially based on interfacial fracture mechanics concepts, which were pioneered by Williams [7] and effectively put into practice by Rice [8] and Hutchinson and Suo [9]. A striking feature of interfacial fracture mechanics is that the toughness of an interface is often a function of the mode mix, defined by the relative amount of tensile and shear tractions on the interface [10-12]. The toughening of interfaces with an increasing shear component has commonly been attributed to asperity locking [13] or increased plastic or viscoplastic dissipation [12, 14] near the crack front. This so-called linearly elastic fracture mechanics (LEFM) approach is generally sufficient in accounting for the behavior of preexisting flaws as long as the fracture process zone is sufficiently small [15, 16]. However, limitations to this approach can arise for fracture with large yielding or process zones where nonlinear effects are critically important.

On the other hand, cohesive zone modeling is a more general approach that can work with larger fracture process zones and without the requirement of a preexisting flaw

[17]. Cohesive zone modeling has been commonly utilized to approximate the nonlinear fracture phenomena and to predict initiation and propagation of interfacial cracks. The ideas behind cohesive zone modeling were originally proposed by Dugdale [18] and Barenblatt [19] in order to mitigate the stress singularities [7, 20] that are the hallmark of LEFM. Since then, it has been applied to a wide range of interfacial fracture problems [21-25], such as delamination in adhesively bonded joints [26-33], laminated, fiber-reinforced composite materials [34-38] and thin films [39-45] as well as adhesive contact problems [46-51], as a few examples in an extensive array of literature.

One of the fundamental aspects in cohesive zone modeling is to define a traction-separation relation (TSR) across the interface, which approximates the nonlinear fracture process. Unlike LEFM where the microscopic mechanisms of fracture are essentially ignored, the TSR in the cohesive zone model depends on the material and the associated fracture mechanism. The methods to extract TSRs are generally classified as either a direct method [52-56] or an iterative method [23, 28, 53, 57]. The direct method usually requires measurements at or near the crack tip, such as crack tip opening displacements and crack extension, which can be challenging and may suffer from resolution issues as well as locating the crack front. For materials that are transparent to visible or infrared radiation, crack opening interferometry has been used to characterize the crack tip behavior [23, 55, 58]. The method can have a resolution of 20 nm and the full crack front can be observed. However, only normal crack tip displacements can be measured. The iterative method, on the other hand, depends on far field measurements, such as force and displacement at the loading point, and determines TSRs by comparing numerical results with experimental data, which has been frequently employed in the past [23, 28, 53, 57]. Gowrishankar, et al. [55] used a three-step procedure in an iterative method to determine the key parameters for

the TSR and concluded that both methods compared reasonably well, while the direct method offers the ease of parameter extraction with little cost in accuracy.

The implementation of the cohesive zone model with a specific TSR in finite element analysis is relatively easy, either by embedding one layer of cohesive elements or by defining a cohesive surface interaction. To complete a typical TSR, a minimum requirement includes four pieces of information: the interfacial toughness, the strength (maximum traction), the initial stiffness and a shape parameter that defines the softening part of the TSR. It has been shown that the shape parameter is not as important in some cases [59, 60] but is important in others [61, 62]. Exponential softening was found to be optimal in terms of the degree of approximation achieved. Gowrishankar, et al. [55] showed that the measurement of the crack tip displacement was needed to determine the shape parameter of the TSR. Although the exponential softening is often found to be optimal in terms of the degree of approximation, a bilinear TSR achieved the best compromise between the computational cost and the finite element approximation.

In spite of the popularity, some numerical issues in cohesive zone modeling have not been fully solved. For example, when extreme values of the parameters are assigned to the simulations, numerical instabilities and convergence difficulties are still common at the onset of the crack propagation [63, 64]. Following the idea of Kanninen [65], analytical solutions were derived from the beam theory by introducing springs in the normal and tangential directions holding the upper and lower surfaces. The TSRs are used to describe the constitutive law of the springs. The solutions are available in different experimental settings: mode-I double cantilever beam (DCB) tests [66, 67], mode-II end notch flexure (ENF) tests [68] and mixed-mode tests [69, 70]. In most of the solutions, the interactions between the surfaces were assumed to be linearly elastic with no damage. The nonlinear

traction-separation relations were considered by Jain, et al. [71] and Xie, et al. [72]. The former assumed a linear softening for the damage and reduced the complex beam theory to simpler scaling equations that are used to determine the critical load and fracture process zone length. The latter dealt with general TSRs by linearization and proposed a numerical framework for solving the mixed-mode fracture problems.

1.2 Mixed-mode fracture

Many test methods have been successfully developed for characterizing fracture at interfaces under all three fracture modes and combinations thereof. The most commonly used type of specimen for determining the fracture toughness of a bi-material system is the double cantilever beam (DCB) specimen as established by Kanninen [65]. As a logical evolution from quasi-static testing with DCB specimens, alternative specimen geometries, such as reinforced adherends [73, 74] and tapered adherends [75], were studied for measuring, among other reasons, the mode-I fracture toughness at high separation rates. One major challenge for using the classical DCB configuration at higher loading rates is that the specimen tends to open unsymmetrically [76], which changes the stress state at the crack tip from pure mode-I to mixed-mode opening. To address this issue, Hug, et al. [77] achieved pure mode-I conditions at higher velocities by transferring the vertical movement of the hydraulic piston into a horizontal opening displacement of a vertically mounted specimen, which reduced the influence of gravity to a minimum.

Mixed-mode fracture has been achieved by introducing asymmetries either in the specimen geometries or loading conditions. Specimen geometries, such as asymmetric DCB [78], four-point flexure and composite cylinder [79, 80], have been used to obtain specific phase angles of mode mix at the crack tip. Other commonly used mixed-mode test methods include the end loaded split [9, 81] and the compact tension shear specimens [82].

In particular, the latter configuration enables the variation of the mode-mix over the complete range but in coarse increments. Among all these techniques, the asymmetric DCB specimen has been widely accepted because it is easy to fabricate and covers a reasonable range of phase angles [83]. A recent work [56] on this matter was able to characterize the mixed-mode fracture for a silicon/epoxy interface with phase angles ranging from -53° to 87.5° .

Asymmetry can also be introduced by applying uneven loads to a symmetric laminate. Reeder and Crews [84] pursued such an approach to study mixed-mode fracture in laminated fiber reinforced composites. Similarly, Fernlund and Spelt [85] developed a complex loading jig consisting of a linkage system which induced an asymmetry in the forces acting on the upper and lower adherends. Davidson and Sediles [86] went a step further by developing a device that made use of bending and torsion on a laminate to produce all three fracture modes. Although none of these devices were used to extract TSRs, there were some questions from a theoretical standpoint [87] as to the suitability of applying uneven end loads rather than moments for providing fracture properties under large scale bridging conditions. Because configurations that employ uneven end moments [88-91] provide crack tip stress fields that are invariant with crack length, it was postulated that they would provide true material properties, uninfluenced by structural effects. This point has recently been addressed by Pappas and Botsis [92], who also developed a more convenient way to apply uneven bending moments. They found that applying uneven end loads or moments to an adhesively bonded laminate resulted in very similar TSRs even though the damage zone was relatively large. On the other hand, the same was not true of a laminated fiber reinforced polymer with a large and complex bridging zone.

All the approaches for controlling mode-mix that have been discussed so far are inherently proportional loading devices, which do not allow the effects of more complex mixed-mode loading paths to be followed. Biaxial loading devices [93-95] that apply uniform tension and shear to a bimaterial strip are certainly capable of achieving such a goal, but are complex. A conceptually simpler approach was provided by Singh, et al. [96] who used a dual actuator device to apply uneven end loads to a symmetric laminate.

1.3 Rate dependent fracture

Rate-dependent fracture of polymers and their interfaces may result from viscoelasticity and damage processes. The damage processes are often confined in a small region around the crack tip and may be described by rate-dependent traction-separation relations. Previously, Knauss and Losi [97] proposed a rate-dependent crack propagation model for craze-like fracture in polymers and failure of a bonded joint with a thin adhesive layer, where a nonlinear viscoelastic constitutive model was used in a narrow cohesive zone and the effect of void formation was accounted for by an experimentally determined damage function. Later, Rahul-Kumar, et al. [98] implemented a family of cohesive elements with rate-independent and rate-dependent TSRs for fracture at polymer interfaces. They described two rate-dependent cohesive zone models, one based on a rate-dependent craze-like fracture model [97] and the other based on a generalized viscous fluid model [99-101]. The rate-dependent toughness of elastic-viscoplastic materials was analyzed in Landis, et al. [102] using a viscoplastic TSR that follows a similar functional form as the constitutive relation for the bulk material. Based on their experiments, Liechti and Wu [103] used a nonlinear viscoelastic Kelvin unit to simulate rate-dependent cohesive forces between rubber and steel under mixed-mode loading at different rates. Similarly, a nonlinear spring in parallel with a linear Maxwell element was used in a rate-dependent

cohesive zone model [104] for crack growth in adhesive joints. Zhang, et al. [105] proposed a cohesive zone model consisting of a plastic region and a damage region, each of which was described by a rate-dependent TSR with a linear viscosity. Giambanco and Fileccia Scimemi [106] formulated a rate-dependent interface model in the framework of viscoplasticity considering hardening, softening and friction in presence of shear and tensile tractions. Based on compact tension tests of bulk epoxy, Makhecha, et al. [6] developed two rate-dependent traction-separation relations, each with one rate-dependent parameter, to simulate the stick-slip fracture in an adhesively bonded aluminum double cantilever beam. A direct approach was used by Zhu, et al. [54] to determine the mode-I and mode-II TSRs of a polyurea/steel interface, which exhibited strong rate dependence. Marzi, et al. [107] used bilinear traction-separation relations with rate-dependent parameters directly extracted from experiments for failure of structural adhesive joints loaded in mode-I. A similar approach was followed by Mohammed, et al. [108] in their study of pressure-sensitive adhesives, which also suggested that the rate dependence in their experiments was dominated by the rate-dependent interfacial properties, rather than the bulk viscoelasticity. This circumstances may fall into the so-called “interphase” fracture as described by Rakestraw, et al. [109]. They also found a pattern (Fig. 1.2) that altering the loading rate can cause the failure to change modes: slower loading rates tended to cause interfacial failures by reducing the interfacial toughness but increasing the cohesive toughness, while cohesive failures were frequently observed at higher loading rates.

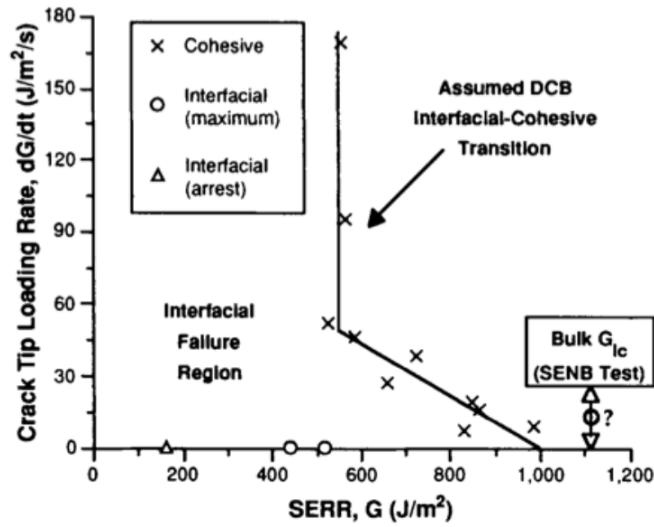


Figure 1.2 Fracture energies as a function of induced loading rate [109].

1.4 Bond rupture kinetics

The traction-separation relations are essentially continuum descriptions of the bimaterial interfaces subject to tensile and/or shear tractions. Such descriptions are phenomenological but could, in principle, be linked to atomistic or molecular mechanisms [98, 100, 101, 110, 111], which would provide more fundamental understanding of the interactions during fracture.

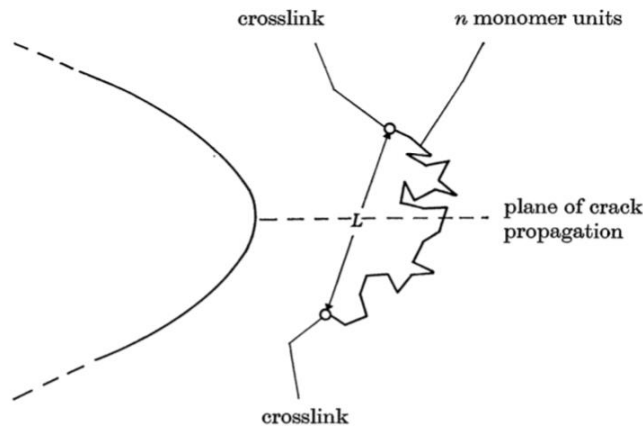


Figure 1.3 Schematic of a polymer chain lying across the plane of crack propagation [112].

Following the Griffith theory of fracture, Rivlin and Thomas [113] defined and experimentally measured the “tearing energy” that is independent of the shape of the specimen configuration and the loading conditions. This characteristic energy then was linked to the rupture of the polymer chains that are lying across the plane of crack propagation (Fig. 1.3) by Lake and Thomas [112]. Their idea also explains the discrepancy in the magnitude between the tearing energy and the bond strength by considering that all bonds need to be equally stretched to a critical level before the rupture of a chain. The brittle manner of the fracture led to the assumption of the critical bond strength, while other de-bonding processes were believed to occur diffusively rather than ballistically [114]. The framework proposed by Kramers [115] established the thermodynamic equilibrium states through a diffusion process and a probability was calculated to determine the state of equilibrium from one to another based on the potential barrier. In line with the Kramers’ theory, Zhurkov [116] examined the dependence of the lifetime of solids on the external force and temperature, and proposed a kinetic equation, where the energy barrier linearly decreases with the external force and the decrease of the energy barrier accelerates the fracture process. The kinetic theory was adopted and extended by Bell [117] to develop a theoretical framework for studying the cell adhesion through bond formation and separation between molecules. Evans and Ritchie [118] further discussed the influence of the applied force to the energy landscape during the force-driven dissociation of bonds, and elaborated in detail the effect of the loading rate to the strength of bonds. More recently, the concept of the bond survival probability was established by Freund [119] and related to the off-rate in chemical reactions. The statistical description allows the material separation to be determined by the breaking of chemical bonds in terms of bonding parameters, instead of requiring material failure conditions. The efforts to solve continuum level problems by bonding kinetics were continued, examples including the detachment of

a sphere from an elastic half space by Wei [120] and the peeling of an elastic strip by Qian, et al. [121].

The entropic contribution from stretching a chain was usually neglected because it was found to be small compared to the internal energy due to bond deformation [112]. However, this argument seems to be inconsistent with the classical ideal chain model [122], where the change in the free energy was dominated by the chain entropy. Mao, et al. [123] made an effort to reconcile the two classical theories by relaxing the bond rigidity in the ideal chain model so that each bond in a chain can deform and the deformation of a bond is determined by minimizing the total free energy. Their model behaves similarly to the freely jointed chain model (FJC) at relatively low stretch levels and predicts the increase of the internal energy during large deformation. The transition in between was determined by only one parameter, the bond energy. Following this idea, Mao and Anand [124] developed a theory for the fracture of polymeric gels, in which the coupled diffusion-deformation-fracture problem for ideal gel network was addressed. A recent work by Li and Bouklas [125] started from the same idea but considered the distribution of chain lengths, and finally coupled to a phase-field model for fracture in polydisperse elastomers.

1.5 Research scope

This dissertation presents an experimental characterization of the rate-dependent fracture of a silicon/epoxy interface and a theoretical modeling of the rate effect on the interfacial properties. Different experimental schemes were explored for the beam-like specimen configurations, including development of a novel dual-actuator loading device. Theoretical work includes an investigation of the previous methods for interfacial fracture analysis and development of a multiscale mechanism-based cohesive zone model with rate dependence. This dissertation is organized as the follows.

Chapter 2 focuses on the mode-I rate-dependent fracture of the silicon/epoxy interface. A total of 17 DCB specimens were tested over a wide range of separation rates. A direct method based on the beam on elastic foundation (BEF) model was used to extract the interfacial properties directly from the measurements, followed by an iterative approach to determine the rate-dependent TSRs. A rate-dependent cohesive zone model was then proposed based on thermally activated bond rupture kinetics assuming linear relations for the bond force and the energy barrier.

Chapter 3 continues the effort in developing a multiscale mechanism-based cohesive zone model from bottom up, consisting of four different scale levels (bond, chain, interface, and specimen). The model relates the measurable interfacial properties (toughness and strength) to the molecular structures of the interface in terms of the bond energy, chain length and chain density. With a numerical implementation of the model, finite element simulations of the mode-I DCB experiments were conducted and compared to the measurements.

Chapter 4 presents the design and development of a dual-actuator loading device and its implementation through a series of mixed-mode fracture experiments. The crack tip traction-separation relations were extracted by a direct method only using the far-field measurements and validated by numerical simulations. The dependence of the local separation rate, crack tip mode angle and crack length on the interfacial fracture were examined based on the extracted interfacial properties. Possible extension of the multiscale cohesive zone model for the mixed-mode fracture is discussed.

Chapter 5 summarizes the results from the present study and remarks on potential directions for future work.

Chapter 2 Mode-I rate-dependent interfacial fracture

This chapter focuses on rate-dependent fracture of a silicon/epoxy interface under nominally mode-I conditions. Fracture experiments were conducted at 5 different separation rates, ranging from 0.042 to 8.5 mm/s. For each separation rate, the interfacial properties were extracted by a beam on elastic foundation model and an iterative method, assuming a bilinear traction-separation relation. Rate dependence is observed for the silicon/epoxy interface as both the interfacial toughness and strength increased with the separation rates, which is opposite to the rate-dependent fracture behavior of the bulk epoxy in its glassy state. Motivated by this observation, a rate-dependent cohesive zone model is proposed based on a thermally activated bond rupture mechanism. This model relates interfacial fracture to the breakage of molecular bonds at the interface, and the rate effect develops naturally from the kinetics of damage evolution via the statistical concept of bond survival probability. The double cantilever beam problem with the interfacial bond rupture kinetics was then solved numerically, and the model parameters were extracted by fitting the numerical results to the experimental data.

2.1 Double cantilever beam (DCB) experiment

2.1.1 *Material properties*

In the mode-I DCB experiment, N-type silicon strips (Young's modulus 169 GPa and Poisson's ratio 0.22) with (111) surfaces were used as the adherend material because silicon with this orientation has the smoothest surface and densest atomic arrangement, thereby also minimizing any fracture of the silicon. A dicing machine (Disco, DAD 321) was used to cut 100mm diameter silicon wafers ($500 \pm 25\mu\text{m}$ in thickness) into $40 \times 5\text{mm}$ strips. It is necessary to polish the side faces of the silicon strips when the thickness is

relatively small. During the dicing process, many cracks and defects can be created at the side faces, which increases the stress concentration when the silicon strip undergoes bending deformation in the experiment. This may cause the breaking of the silicon ahead of the interface fracture. In this work, we polished the silicon strips on a variable speed grinder machine (Ecomet 3, Buehler) with two steps: a coarse polish with the silicon carbide 600 grit size (particle size 15 μm) and then a fine polish with the diamond compound (particle size 3 μm). The silicon strips were then cleaned individually by ultrasonication in de-ionized water to remove any particles that might have accumulated during the polishing.

The epoxy (EP30, Master Bond Inc.) was prepared by mixing the resin and hardener thoroughly in a 4:1 ratio by weight. The mixing process was consistently controlled over 10 minutes. A shorter time can cause insufficient mixing, which affects the strength of the epoxy following cure. The mixture of resin and hardener was degassed in a vacuum chamber to remove trapped bubbles formed during the mixing process.

The mechanical behavior of the EP30 was characterized by conducting uniaxial tensile tests and Arcan shear tests [126, 127] in a universal testing machine (Instron). The stress-strain curve in normal direction is shown in Fig. 2.1a. The Young's modulus of the epoxy obtained from the unloading (or second loading) curve was 2.4 GPa. The yield strength of the epoxy was estimated to be 36 MPa. The uniaxial tensile test was conducted with another two strain rates (Fig. 2.1b). The epoxy behaved rather glassy when the strain rate was relatively high ($\dot{\epsilon} > 10^{-4}$). During the DCB experiment, the local strain rate turned out to be fairly large ($\dot{\epsilon} \sim 10^{-2}$) near the crack tip of the silicon/epoxy interface so that the epoxy was assumed to be in its glassy state and hence linearly elastic. The Arcan tests were also conducted under three strain rates. The corresponding stress-strain curves

were shown in Fig. 2.2. Several key findings about the epoxy are summarized as: (1) the shear modulus increased with increasing strain rates, however, the variation was small, especially between $10^{-6}/s$ and $10^{-4}/s$; (2) the 0.2% yield strength (~ 24 MPa) was the same among the different separation rates. The significance of the shear behavior of the epoxy is not seen in the mode-I fracture experiments; however, it is an essential component in the mixed-mode experiments as to check if the plasticity in the epoxy layer had been triggered by the relatively large shear stress at the silicon/epoxy interface.

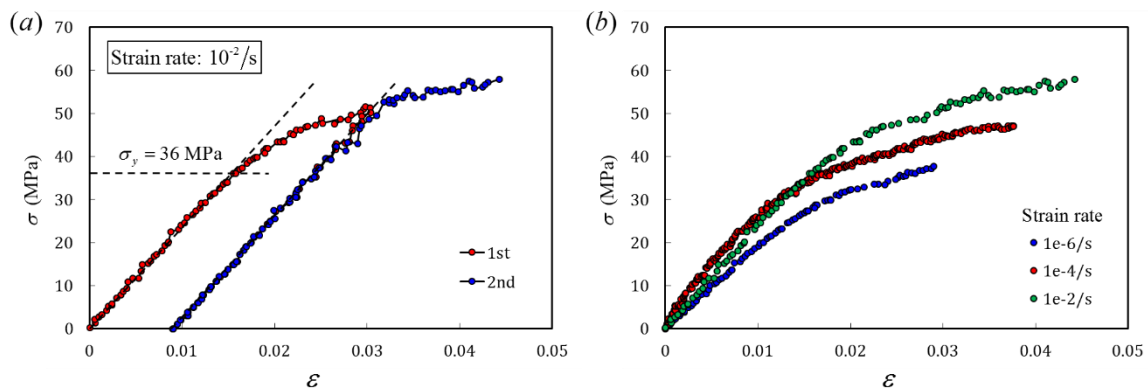


Figure 2.1 Stress-strain behavior of EP30 characterized by a uniaxial tension test: (a) loading-unloading-reloading curve; (b) at different strain rates.

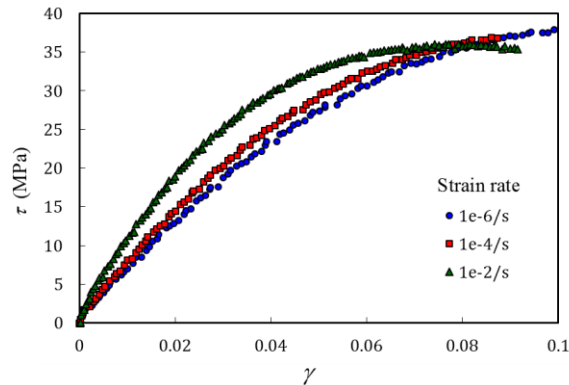


Figure 2.2 Stress-strain behavior of EP30 characterized by an Arcan shear test under multiple strain rates.

2.1.2 Experimental procedures

In the mode-I experiments, a sandwich double cantilever beam specimen consists of two layers of silicon bonded by an epoxy (Fig. 2.3). The silicon strips were bonded to aluminum tabs at the opening end (Fig. 2.3 inset), which were connected to a servo hydraulic, universal testing machine through two pins. The displacement rate control was applied at the opening end of the specimen and the bonded end was free. The reaction force was measured by a load cell (45N range, Omega). One silicon adherend was coated with an Au/Pd film (~ 15 nm) from one end of the strip to a length of 15–20 mm. The purpose of the Au/Pd coating is to form a sharp crack between silicon and epoxy, with minimal damage ahead of the initial crack front, because the adhesion energy between Au/Pd coating and the epoxy is relatively small (~ 0.07 J/m²) compared to the silicon/epoxy interface. The sharp crack reduces the crack blunting effect by minimizing the shear yielding around the crack tip [128, 129], and thus plane strain behavior dominates and steady-state crack growth is expected. The effect of the coating layer can be observed from the measured load-displacement curve as seen in Fig. 2.4. When there is no coating, the force required to initiate a crack from the bimaterial corner at the epoxy terminus is apparently larger than that required for the sharp crack produced by the Au/Pd coating. The two responses eventually converge for steady-state crack growth.

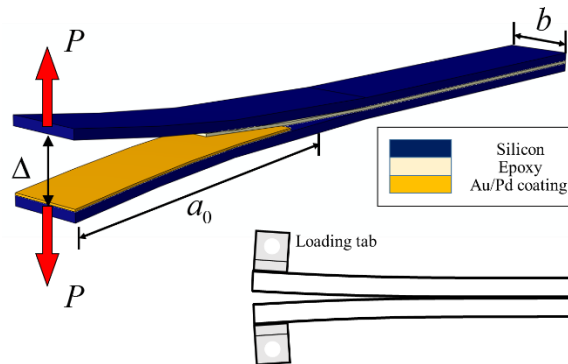


Figure 2.3 Schematic of a DCB specimen and loading tabs.

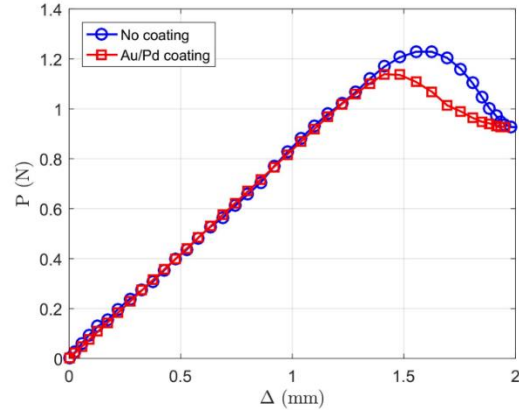


Figure 2.4 Load-displacement curves of two specimens with the same initial crack length, one with the Au/Pd coating for a sharp initial crack and the other without a coating.

Fracture experiments were conducted at 5 different separation rates, ranging from 0.042 to 8.5 mm/s. For each separation rate, at least 3 specimens were tested to provide a measure of the reliability of the data. We note that, while the applied separation rate was controlled at the opening end of the specimen, the local separation rate at the crack tip depends on the initial crack length as well as the interfacial properties, which cannot be directly controlled in the experiments.

2.2 Analysis

In this section, we present a series of analyses of the DCB experiments. First, we conduct a mode-mix analysis following LEFM to confirm that the DCB experiment is nominally mode-I. Then, a beam on elastic foundation (BEF) model is adopted to directly, but approximately, interpret the experimental data. Next, we describe the iterative method that was used to extract the traction-separation relation for cohesive zone modeling of the silicon/epoxy interface at each separation rate. Finally, we propose a rate-dependent cohesive zone model based on the thermally activated bond breaking kinetics and numerically solve the DCB problem at different separation rates.

2.2.1 Mode-mix analysis

Both the specimen structure and loading conditions were designed to be symmetric for the purpose of maintaining a nominally mode-I fracture experiment. However, because the crack propagated along one of the silicon/epoxy interfaces, the presence of the epoxy layer induced a shear component at the interface. In addition, although the thickness of the epoxy layer was within $\pm 2 \mu\text{m}$ for each specimen, it ranged from 5 to 40 μm from specimen to specimen. Accordingly, a series of finite element analyses were conducted to determine the effect of the epoxy layer on the mode-mix of the interfacial fracture in the DCB experiments.

Two-dimensional (2D) finite element analyses were conducted using ABAQUS, similar to previous studies [55]. The silicon and epoxy were both assumed to be linearly elastic and isotropic. The thickness of each silicon strip was set to be 0.5 mm, while the epoxy thickness was varied from 1 to 40 μm . Based on LEFM concepts, the interfacial crack has a complex stress intensity factor, $K = K_1 + iK_2$, and the phase angle of fracture mode-mix is defined by

$$\psi = \tan^{-1} \left(\frac{\text{Im}(Kl^{i\varepsilon})}{\text{Re}(Kl^{i\varepsilon})} \right) \quad (2.1)$$

where $\varepsilon = \frac{1}{2\pi} \ln \left(\frac{1-\beta}{1+\beta} \right)$ with Dundurs' parameter $\beta = \frac{1}{2} \frac{\mu_1(1-2\nu_2) - \mu_2(1-2\nu_1)}{\mu_1(1-\nu_2) + \mu_2(1-\nu_1)}$ and μ_i ($i = 1, 2$) are the shear moduli of silicon and epoxy, respectively. For $\beta \neq 0$, the phase angle of mode-mix is determined by introducing a reference length l [8], and the choice of different length scales leads to a shift in the phase angle. In the present study, we take the reference length to be the epoxy layer thickness, i.e., $l = h_e$. The interfacial stress intensity factors for the DCB specimens with different epoxy thicknesses were obtained directly

from the finite element analysis and the phase angles of mode-mix were determined by Eq. (2.1) as tabulated in Table 2.1.

Table 2.1 Mode mix of DCB specimens with different epoxy thickness

Epoxy thickness (μm)	Mode-mix ($^{\circ}$)
1	13.6
5	13.5
10	13.3
20	12.9
30	12.5
40	12.2

As expected, the presence of an epoxy layer gives rise to a mode-mix of $13.0 \pm 0.52^{\circ}$ over the range of epoxy layer thickness that were considered in the present study. The variation of mode-mix is small for this range of epoxy thickness, and it is close to the theoretical limit of 12.8° [9] for an interfacial crack in a sandwich structure with a thin epoxy layer between two infinitely thick silicon substrates subjected to symmetric remote loading. In previous studies of similar epoxy interfaces, the interfacial fracture toughness was found to be essentially independent of the mode mix for the range $-30^{\circ} \leq \psi \leq 45^{\circ}$ [10, 12, 14, 23, 126, 130]. Hence, we may assume that the fracture toughness and traction-separation relations for the DCB specimens in the present study are essentially mode-I, independent of the epoxy thickness. Hereafter, we treat the DCB fracture experiments with

the silicon/epoxy/silicon sandwich specimens as mode-I and neglect the effects of shear.¹ Moreover, the effect of any small variation in epoxy thickness does not contribute to the difference in the interfacial properties, and our focus is on the rate effect.

2.2.2 *Beam on elastic foundation analysis*

In the DCB experiment, both the specimen structure and loading conditions were designed to be symmetric for the purpose of maintaining a nominally mode I fracture at the interface. Therefore, the shear stress at the interface of the DCB specimen was negligible, leaving the normal stress as the primary traction between the silicon and epoxy. Considering only the normal traction, a beam on elastic foundation model (see details in Appendix A) as presented in previous studies [55, 58] was adopted to determine the crack growth and the J-integral based on the measurements of the applied load and displacement (Fig. 2.5). The beam on elastic foundation model predicts the load-displacement response at the loading point as:

$$P = \frac{3\bar{E}_1 I_1 \Delta}{2a^3} \left(1 + \frac{3}{\lambda a} + \frac{3}{(\lambda a)^2} + \frac{3}{2(\lambda a)^3} \right)^{-1} \quad (2.2)$$

where P and Δ are applied force and the opening displacement at the loading point, a is the crack length (measured from the loading point to the crack tip; see Fig. 2.3), $I_1 = b_1 h_1^3 / 12$ for the silicon beam with width b_1 and thickness h_1 , $\bar{E}_1 = E_1 / (1 - \nu_1^2)$, and $\lambda = (6K_0 / (\bar{E}_1 h_1^3))^{1/4}$ with K_0 being the stiffness of the elastic foundation. In this chapter, $P = P_1 = -P_2$ and $\Delta = \Delta_1 - \Delta_2 = 2\Delta_1$ due to the symmetry conditions in the

¹ The shear effect will be considered in Chapter 4 with asymmetric loading on the DCB specimens.

mode-I fracture experiments, where P_i and Δ_i are the forces and displacements at the loading points with $i = 1$ and 2 for the upper and lower beams, respectively.

For the sandwich beam specimen with an epoxy layer, the stiffness K_0 was approximately taken as $K_0 = \bar{E}_e/h_e$ in the previous study [56]. In this work, a different approach was used to determine the stiffness. By measuring the distance from the epoxy terminus to the loading point on the specimen after the silicon was peeled off, the initial crack length a_0 was determined. Then, with the crack length a_0 , the initial linear portion of the load-displacement response can be used to determine the stiffness by Eq. (2.2) (shown as the red solid line in Fig. 2.5a). The value of the stiffness was found to be $K_0 = 7.5 \times 10^{12} \text{ N/m}^3$, which is about two orders of magnitude smaller than the value used in the previous study [56].

Based on Eq. (2.2), the crack length (beyond the initial length) can be determined from the measurements of P and Δ as

$$a(P, \Delta) = \frac{1}{\lambda} \left[\left(\frac{3\lambda^3 \bar{E}_1 I_1 \Delta}{2P} - \frac{1}{2} \right)^{1/3} - 1 \right]. \quad (2.3)$$

The corresponding J-integral for the DCB specimen is [55]

$$J(P, \Delta) = \frac{12P^2}{\lambda^2 \bar{E}_1 b_1^2 h_1^3} \left[\frac{3\lambda^3 \bar{E}_1 I_1 \Delta}{2P} - \frac{1}{2} \right]^{2/3}. \quad (2.4)$$

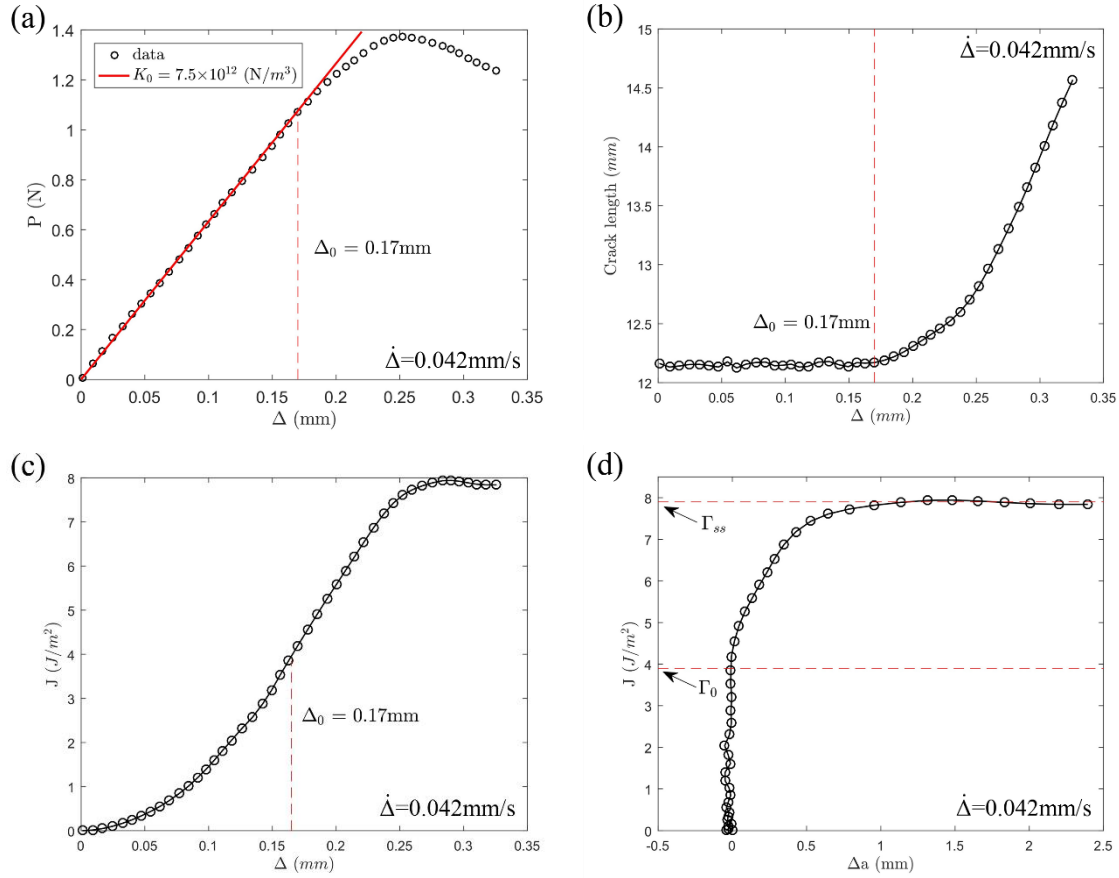


Figure 2.5 (a) Measured load-displacement response for a DCB specimen, with the initial linear portion fitted by Eq. (2.2) using the measured initial crack length and the stiffness of the elastic foundation. (b) Crack length determined by Eq. (2.3) versus the applied displacement; (c) J-integral by Eq. (2.4) versus the applied displacement; (d) The fracture resistance curve.

As shown in Fig. 2.5, based on the measured load-displacement response (Fig. 2.5a) for a DCB specimen, the crack length (Fig. 2.5b) and the J-integral (Fig. 2.5c) were calculated by Eq. (2.3) and Eq. (2.4), respectively. The fracture resistance curve (Fig. 2.5d) was then obtained for each specimen, where the crack extension is defined as $\Delta a = a - a_0$. In all cases, the crack did not grow until the J-integral reached a critical value ($J = \Gamma_0$) corresponding to a critical separation (Δ_0), beyond which the crack grew as the J-

integral continued increasing. Eventually, a steady state was reached with a constant J-integral ($J = \Gamma_{ss}$), commonly taken as the fracture toughness of the interface. Moreover, the strength of the interface can be defined as the critical traction for the initiation of crack growth, which may be estimated as $\sigma_0 = \sqrt{2K_0\Gamma_0}$ (assuming a linear traction-separation relation up to the critical traction). As discussed in Section 2.3, it was found that the fracture resistance curve, the steady-state toughness and the strength are all rate dependent.

2.2.3 *Bilinear traction-separation relations by iterative method*

Next, we assume a bilinear traction-separation relation (Fig. 2.6) for each specimen and determine the parameters by an iterative method. To fully determine a bilinear traction-separation relation, three parameters are required: the elastic stiffness K_0 , the interfacial strength σ_0 , and the fracture toughness Γ_{ss} . A damage parameter D is used to describe the state of the interface as it evolves from 0 to 1 depending on the local separation:

$$D = \frac{\delta_c(\delta_m - \delta_0)}{\delta_m(\delta_c - \delta_0)}. \quad (2.5)$$

Here, $\delta_0 = \sigma_0/K_0$ is the critical separation for damage initiation, $\delta_c = 2\Gamma_{ss}/\sigma_0$ is the critical separation for fracture, and δ_m is the maximum separation experienced by the interface element. The bilinear traction-separation relation is then given by

$$\sigma = (1 - D)K_0\delta. \quad (2.6)$$

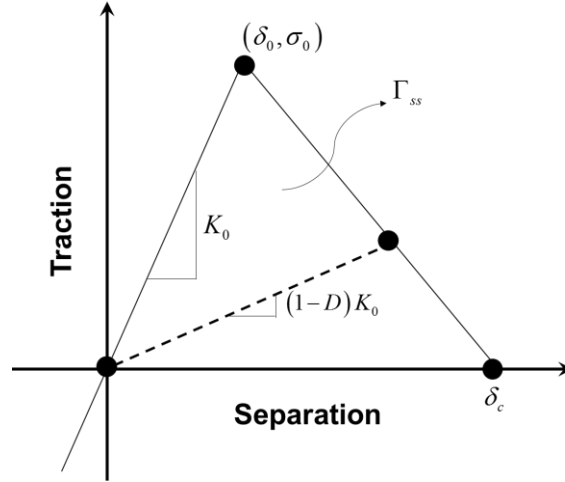


Figure 2.6 Schematic of a bilinear traction-separation relation.

The bilinear traction-separation relation was adopted for the silicon/epoxy interface in a 2D finite element model using the surface interaction module in ABAQUS. Both silicon strips and the epoxy layer were modeled by four-node plane strain elements (CPE4). For the applied strain rates in this study, the epoxy is assumed to be in its glassy state and hence linearly elastic, and plastic yielding of the epoxy is negligible because the strength of the interface in the present study is well below the yield strength of the epoxy (~36 MPa).

For each DCB specimen, we first estimate the three parameters for the bilinear traction-separation relation based on the BEF analysis as discussed in Section 2.2.2. To improve the accuracy, an iterative approach was then adopted to determine the traction-separation relation of the silicon/epoxy interface at each separation rate by comparing the results of the finite element simulation with the measurements. In particular, the initial stiffness K_0 was fully determined by the linear portion of the load-displacement curve (Fig. 2.5a), which was nearly independent of the separation rate. The other two parameters

(Γ_{SS} and σ_0) were determined iteratively following the process outlined by Gowrishankar, et al. [55].

As an example, consider the steps that were taken to identify the parameters for the traction-separation relation at a separation rate of 0.042 mm/s (Fig. 2.7). The descending portion (Fig. 2.7a) of the load-displacement curve from the numerical simulations depends sensitively on the value of the fracture toughness. As the first step, $\sigma_0^{(0)}$ was fixed at 7.7 MPa and $\Gamma_{SS}^{(1)}$ was established as 8 J/m². Figure 2.7b shows the effect of the interfacial strength on the load-displacement curve near the peak force with the fracture toughness now fixed at $\Gamma_{SS}^{(1)} = 8$ J/m², where $\sigma_0^{(1)} = 8.5$ MPa was selected as the strength value. In this case, convergence was achieved (error less than 1%) with only one iteration and thus the two parameters ($\sigma_0 = 8.5$ MPa and $\Gamma_{SS} = 8$ J/m²) along with $K_0 = 7.5 \times 10^{12}$ N/m³ give a satisfactory traction-separation relation for this specimen. The same procedure was followed for all specimens in the present study and the results are presented in Section 2.3.

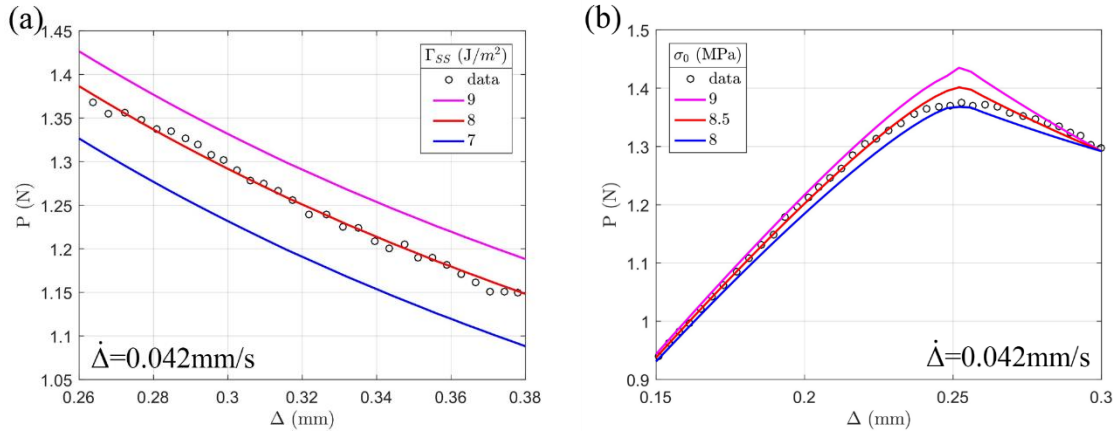


Figure 2.7 Comparisons between load-displacement curves from finite element solutions and experimental data. (a) The descending portion varies with the fracture toughness; (b) The response near the peak force varies with the strength of the interface.

2.2.4 A kinetic bond rupture model

The bilinear traction-separation relations determined by the iterative method indicate the rate-dependent fracture of the silicon/epoxy interface, which are specific to the applied separation rates in the DCB experiments. To understand possible origins of the rate dependence and to predict fracture at different rates, a mechanism-based model is needed. In this subsection, we propose a rate-dependent cohesive zone model based on the kinetic bond rupture mechanism, following the spirit of Bell [117] and Freund [119].

The fracture of an interface is considered to be the result of thermally activated bond breaking processes. Let $N(t)$ be the number of intact bonds per unit area of the interface at the time t . The rate of thermally activated bond breaking follows the Arrhenius law, namely

$$\frac{\dot{N}(t)}{N(t)} = -\frac{1}{t_0} \exp\left(-\frac{E_b}{k_B T}\right), \quad (2.7)$$

where E_b is the energy barrier that depends on the specific bonds and the force applied to the bonds, and t_0 is a microscopic time scale that depends on temperature T and can be taken as $t_0 = \hbar/k_B T$ [131], with Boltzmann constant $k_B = 1.38 \times 10^{-23}$ J/K and Planck constant $\hbar = 6.626 \times 10^{-34}$ J·s. Eq. (2.7) is essentially the same as Bell's model for cell adhesion but without the bond formation term on the right hand side. Moreover, Eq. (2.7) follows the classical transition-state theory, which turns out to be a special case and upper bound for the more general reaction-rate theory [131].

As noted by Freund [119], the statistics of bond breaking for a large number of nominally identical bonds can be re-interpreted equivalently as the survival probability of each single bond. Define the bond survival probability as

$$R(t) = N(t)/N_0, \quad (2.8)$$

where N_0 is the initial number of intact bonds (per unit area). Combining Eq. (2.7) and Eq. (2.8), the bond survival probability follows a rate equation as

$$\frac{\dot{R}(t)}{R(t)} = -\frac{1}{t_0} \exp\left(-\frac{E_b}{k_B T}\right). \quad (2.9)$$

A damage parameter D can be defined as the proportion of the broken bonds, which is related to the bond survival probability as:

$$D = 1 - R. \quad (2.10)$$

Then, the evolution of the damage parameter follows a similar rate equation through:

$$\frac{\partial D}{\partial t} = \frac{1-D}{t_0} \exp\left(-\frac{E_b}{k_B T}\right). \quad (2.11)$$

The traction transmitted across the interface is proportional to the number of intact bonds per unit area, i.e. $\sigma = N f_b$, with f_b being the force per bond, which can be written as a function of both the separation and the damage parameter, namely,

$$\sigma(\delta, D) = (1 - D)f(\delta), \quad (2.12)$$

where $f(\delta)$ is a function that describes the traction-separation relation when there is no bond breaking ($D = 0$). With Eqs. (2.11) and (2.12), we formulate a rate-dependent cohesive zone model, where the energy barrier E_b and $f(\delta)$ may be determined for specific bonds or interactions. As a simple example, we assume linear functions for both $f(\delta)$ and E_b as follows:

$$f(\delta) = K_0 \delta, \quad (2.13)$$

$$E_b = \varepsilon_0 \left(1 - \frac{\sigma}{\sigma_c(1-D)}\right). \quad (2.14)$$

With Eq. (2.13), Eq. (2.12) becomes the same as Eq. (2.6) with an initial stiffness K_0 (which can be related to the individual bond stiffness S_b as $K_0 = N_0 S_b$), but the damage

evolution in Eq. (2.11) is rate dependent and different from Eq. (2.5). By Eq. (2.14), the energy barrier for bond breaking is assumed to decrease linearly with the force acting on each bond $f_b = \sigma/N$, similar to Bell's model [117], where ε_0 is the equilibrium bond energy and σ_c is a critical stress for instantaneous bond breaking ($\sigma_c = N_0 f_{bc}$), with f_{bc} being the critical force for each bond). When the traction is tensile ($\sigma > 0$), the interfacial bonds are stretched, and the energy barrier is reduced, thus increasing the probability of bond breaking.

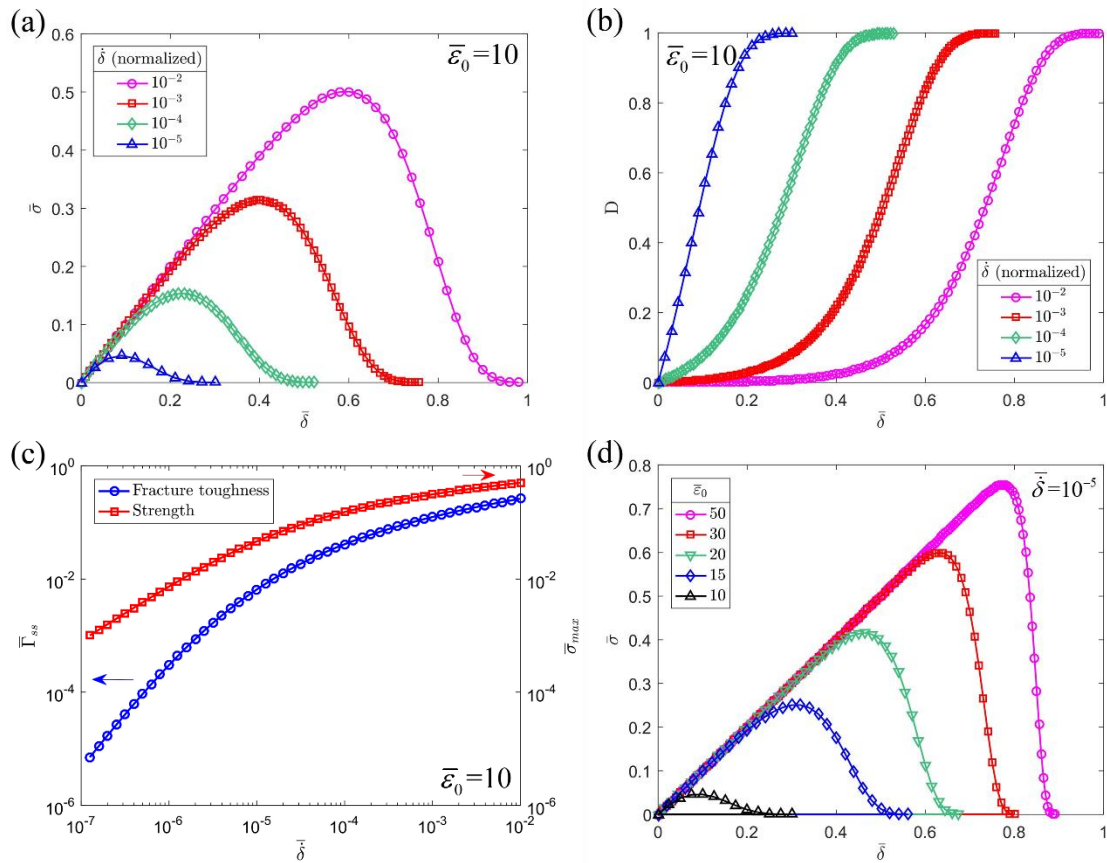


Figure 2.8 (a) Normalized traction-separation relations and (b) damage evolution, for different local separation rates; (c) Rate-dependent fracture toughness and strength predicted by the kinetic model; (d) Effect of the normalized bond energy on the traction-separation relation.

A length scale can be defined as: $l_0 = \sigma_c/K_0$, which is the critical separation for instantaneous bond breaking when $D = 0$. Normalizing the traction by σ_c , the separation by the length scale l_0 , the time by the time scale t_0 , we obtain

$$\bar{\sigma}(\bar{\delta}, D) = (1 - D)\bar{\delta}, \quad (2.15)$$

$$\frac{\partial D}{\partial \bar{t}} = (1 - D) \exp\left(-\frac{\bar{\varepsilon}_0}{k_B T} (1 - \bar{\delta})\right). \quad (2.16)$$

Now consider the case with a constant separation rate $\dot{\delta}$. By Eqs. (2.15) and (2.16), the normalized traction-separation relation depends on two parameters, the normalized separation rate $\bar{\delta} = \dot{\delta}t_0/l_0$ and the bond energy $\bar{\varepsilon}_0 = \varepsilon_0/k_B T$. For a given bond energy ($\bar{\varepsilon}_0 = 10$), the traction-separation relations (Fig. 2.8a) and damage evolution processes (Fig. 2.8b) are both rate dependent. The initial stiffness (K_0) is rate independent, corresponding to the early stage of separation with $D \approx 0$. As the thermally activated bond rupture takes place at the interface, the damage increases and the tangent stiffness decreases. Consequently, the traction first increases and then decreases after a peak value (strength), eventually approaching zero when all bonds are broken ($D = 0$ and $\sigma = 0$). Integrating the traction-separation relation yields the fracture toughness, namely

$$\Gamma_{ss} = \int_0^\infty \sigma d\delta. \quad (2.17)$$

Evidently, both the strength (peak traction) and the toughness increase with increasing separation rate (Fig. 2.8c), qualitatively in agreement with the DCB experiments. By dimensional considerations, the normalized interfacial strength and toughness can be written as

$$\frac{\sigma_{max}}{\sigma_c} = \bar{\sigma}_{max}(\bar{\delta}, \bar{\varepsilon}_0), \quad (2.18)$$

$$\frac{\Gamma}{\sigma_c l_0} = \bar{\Gamma}(\bar{\delta}, \bar{\varepsilon}_0) \quad (2.19)$$

The effect of the normalized bond energy is presented in Fig. 2.8d. As the ratio between the bond energy and the thermal energy ($k_B T$) increases, the softening part of the traction-separation relation becomes more abrupt. In the limiting case when $\bar{\epsilon}_0 \rightarrow \infty$ (e.g., $T = 0$ K), the thermally activated bond rupture mechanism would be completely suppressed so that there is no damage evolution, and the traction would increase linearly up to the critical stress σ_c and then drop to zero as all bonds would break instantaneously. For $\bar{\epsilon}_0 < \infty$, the bond breaking process is thermally activated before the traction reaches the critical level, leading to lower strength and lower toughness. The range of interaction is also reduced as the traction drops to zero before the bonds are stretched to the critical level. This result suggests a temperature effect through the normalized bond energy ($\bar{\epsilon}_0 = \epsilon_0/k_B T$). For a given bond energy ϵ_0 , the interfacial strength and toughness decreases with increasing temperature. It should be noted that the temperature also affects the time scale, $t_0 = \hbar/k_B T$, which would influence the normalized separation rate.

2.2.5 *A rate-dependent DCB model*

In the DCB experiments, the displacements and separation rates were controlled at the loading points, far away from the crack tip. The local separation rate at the crack tip however was different and not controlled. The relation between the global and local separation rates would generally depend on the specific interactions and bond breaking processes, which may be simulated by a cohesive zone model. In a previous study [55], we solved the DCB problem with a rate-independent, bilinear traction-separation relation. Here, with the rate-dependent cohesive zone model (Section 2.2.4), we solve the DCB problem (Fig. 2.9) to simulate the experiments with different separation rates applied at the loading points, which would allow us to directly compare the model predictions with the experiments.

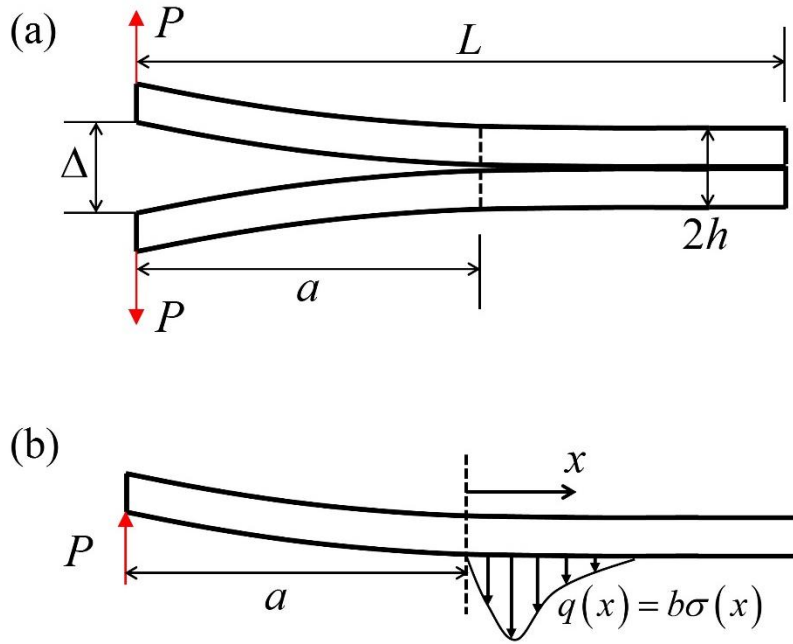


Figure 2.9 (a) Schematics of a symmetric DCB specimen; (b) Deflection of one beam with tractions ahead of the crack tip.

For a symmetric DCB specimen, the deflection of each beam (Fig. 2.9b) is related to the interfacial traction by the simple beam equation:

$$\kappa \frac{\partial^4 w}{\partial x^4} = -b\sigma \quad (2.20)$$

where $\kappa = \bar{E}_1 I_1$ is the bending modulus of the beam, and by symmetry the interfacial separation is: $\delta = 2w$. The epoxy layer between the two beams is ignored for this analysis. For the interfacial strength and toughness levels that are encountered here, this has been shown to be a reasonable assumption [56].

Let $x = 0$ at the initial crack tip ($t = 0$). The DCB specimen is loaded at $x = -a$ with a ramp displacement: $w(x = -a, t) = \dot{\Delta}t/2$, where $\dot{\Delta}$ is the global separation rate.

For $-a < x < 0$, the interface is fractured with $D = 1$ (no bonding) and $\sigma = 0$. By Eq. (2.20), the normal crack opening displacement (NCOD) is obtained as [55]

$$\delta(x, t) = \delta^*(t) - x\theta^*(t) + \frac{P(t)a^3}{3\kappa} \left(3 \left(\frac{x}{a} \right)^2 + \left(\frac{x}{a} \right)^3 \right) \quad (2.21)$$

where $\delta^*(t)$ is the crack-tip opening displacement (CTOD) and $\theta^*(t)$ is the crack-tip opening angle (CTOA), both depending on the interactions ahead of the crack tip. At $x = -a$, $\delta = \dot{\Delta}t$ and the applied force is:

$$P(t) = \frac{3\kappa}{2a^3} [\dot{\Delta}t - \delta^*(t) - a\theta^*(t)] \quad (2.22)$$

For $x \geq 0$, the simple beam equation (2.20) is coupled with the rate-dependent traction-separation relation given by Eqs. (2.15) and (2.16) in the normalized form. The boundary conditions are: (1) At the crack tip ($x = 0$), the continuity conditions are applied for deflection ($\delta = \delta^*$), rotation ($\delta' = -\theta^*$), bending moment ($\delta'' = 2Pa/\kappa$) and shear force ($\delta''' = 2P/\kappa$); and (2) at the end of the beam ($x = L - a$), the clamped conditions are assumed by setting $\delta = 0$ and $\delta' = 0$. The boundary value problem was then solved numerically by a finite difference method (Appendix B).

When there is no damage evolution ($D = 0$), the DCB problem reduces to the beam on elastic foundation model, with Eq. (2.2) for the load-displacement response. A characteristic length scale for the BEF model is: $l_1 = 1/\lambda$, where $\lambda = (K_0b/2\kappa)^{1/4}$. This length scale is typically much larger than the microscopic length scale for bond breaking ($l_0 = \sigma_c/K_0$). In addition, the crack length and the beam length are often larger than l_1 . To bridge the length scales, we normalize x and the crack length a by l_1 , but normalize the beam deflection and separation by l_0 . Consequently, the beam equation (2.20) becomes

$$\frac{\partial^4 \bar{\delta}}{\partial \bar{x}^4} = -4\bar{\sigma} \quad (2.23)$$

Similarly, in addition to the microscopic time scale (t_0) for the thermally activated bond rupture, the applied global separation rate defines an experimental time scale: $t_1 = l_0/\dot{\Delta}$, which is typically much larger than the microscopic time scale. It is thus desirable to re-normalize the rate equation (2.16) using the experimental time scale (t_1) as:

$$\frac{\partial D}{\partial \bar{t}} = \frac{t_1}{t_0} (1 - D) \exp\left(-\frac{\varepsilon_0}{k_B T} (1 - \bar{\delta})\right) \quad (2.24)$$

where the ratio t_0/t_1 is essentially the normalized separation rate applied at the loading point. After re-normalization, the DCB problem depends on four dimensionless parameters: t_0/t_1 (normalized separation rate), $\bar{\varepsilon}_0 = \varepsilon_0/(k_B T)$ (normalized bond energy), $\bar{a} = \lambda a$ (normalized initial crack length), and $\bar{L} = \lambda L$ (normalized specimen length).

Solving the normalized equations in the (2.23), (2.24) and (2.15) with normalized boundary conditions (see Appendix B), we obtain a normalized load-displacement response for a DCB specimen as shown in Fig. 2.10a. Here, we take $t_1/t_0 = 10^{10}$, $\bar{\varepsilon}_0 = 30$, $\bar{a} = 15$ and $\bar{L} = 50$. For a constant separation rate ($\dot{\Delta}$), the normalized separation at the loading point is identical to the normalized time ($\bar{\Delta} = \dot{\Delta}t/l_0 = t/t_1 = \bar{t}$). The force at the loading point (Fig. 2.10a) first increases almost linearly and then decreases, like the experiments (Fig. 2.5a). The crack-tip opening displacement (CTOD) increases with time monotonically (Fig. 2.10b), but the local separation rate changes. Initially, when the damage is nearly zero, the CTOD increases almost linearly with a constant local separation rate, as expected from the BEF analysis [55]:

$$\dot{\delta}^* = \dot{\Delta} \left(\frac{2}{3} (1 + \bar{a})^2 + \frac{1}{3(1 + \bar{a})} \right)^{-1} \quad (2.25)$$

With $\bar{a} \gg 1$, the local separation rate at the crack tip is much smaller than the applied separation rate ($\dot{\delta}^* \ll \dot{\Delta}$). The separation rate at the crack tip starts increasing as the damage accumulates. The damage evolution near the initial crack tip is shown in Fig. 2.10c. The damage at the crack tip reaches 1 at $\bar{t} = 36.7$, beyond which the crack starts to grow. The change of crack length is shown in Fig. 2.10d. Interestingly, even after the crack starts growing, the force at the loading point keeps increasing until $\bar{t} \sim 50$ (Fig. 2.10a), at which point the crack has grown by $\Delta\bar{a} \sim 1$ (Fig. 2.10d).

The normalized traction-separation relations are shown in Fig. 2.10e at different locations of the interface ahead of the initial crack tip ($\bar{x} = 0 \sim 4$). Interestingly, the traction-separation relation varies with the location up to $\bar{x} = 2$, after which it becomes independent of the location. As noted earlier, the local separation rate at the initial crack tip is not a constant for the DCB specimen, unlike the case (stretch a single bond) in Fig. 2.8. Moreover, the loading history could be different at different locations ahead of the initial crack tip, resulting in different traction-separation relations. Eventually, the crack growth reaches a steady-state, after which the traction-separation relation follows the same curve (e.g., $\bar{x} = 3, 4$), indicating the same loading history for every point ahead of the crack tip during the steady-state fracture. In this case (Fig. 2.10e), the steady state is reached when the crack tip advanced to $\bar{x} = 2$ (or $\Delta\bar{a} \sim 2$), corresponding to $\bar{t} \sim 60$. The steady state can also be seen from the damage distribution in Fig. 2.10c, where a damage zone can be identified ahead of the crack tip with $0 < D < 1$ and remains nearly identical in the steady state. More clearly, by shifting the damage distribution curves to the left by the distance of crack growth, we replot in Fig. 2.11a the development of the damage zone ahead of the crack tip, where the damage distributions during the steady state collapse onto the same curve. Moreover, we plot the traction distributions ahead of the crack tip in Fig. 2.11b, corresponding to the damage distributions before and after the steady state.

The J-integral of a DCB specimen, by its definition, can be calculated with a contour enclosing the interface from the crack tip ($\bar{x} = 0$) to the clamped end ($\bar{x} = \bar{L} - \bar{a}$), which leads to

$$\bar{J} = \int_0^{\bar{L}-\bar{a}} \bar{\sigma} \cdot \frac{\partial \bar{\delta}}{\partial \bar{x}} d\bar{x} \quad (2.26)$$

where $\bar{J} = J/(\sigma_c l_0)$ is the normalized J-integral. If the traction-separation relation is identical for all points along the interface, the J-integral in Eq. (2.26) can be reduced to an integral of the traction-separation relation at the initial crack tip, namely

$$\bar{J} = \int_0^{\bar{\delta}^*} \bar{\sigma} d\bar{\delta} \quad (2.27)$$

Eq. (2.27) has been widely used to extract traction-separation relations for rate-independent cohesive zone models [55, 58]. However, for the rate-dependent cohesive zone model considered here, the traction-separation relation at the initial crack tip is different from that in the steady state (Fig. 2.10e). As a result, Eq. (2.27) is generally incorrect, and Eq. (2.26) should be used instead. As shown in Fig. 2.10f, by Eq. (2.27), the J-integral remains constant after crack growth, which is actually the J-integral for crack initiation ($J = \Gamma_0$). By Eq. (2.26), the J-integral increases and reaches a steady state value, a typical behavior for a fracture resistance curve (R-curve). Apparently, the J-integral for crack initiation corresponds to the traction-separation relation at the initial crack tip, and the J-integral for the steady state corresponds to the steady-state traction separation relation at a location ahead of the initial crack tip (e.g., $\bar{x} = 3, 4$). We note that, for the rate-independent cohesive zone models, the same traction-separation relation is often assumed for the entire interface, and to predict the R-curve, crack growth is assumed to initiate at the peak traction. For the bilinear traction-separation relation (Fig. 2.6), the J-integral for crack initiation would be $\Gamma_0 = \sigma_0^2/(2K_0)$ and the steady-state toughness is $\Gamma_{ss} = \sigma_0 \delta_c/2$.

Such assumptions are unnecessary for the rate-dependent cohesive zone model, which naturally predicts a rate-dependent R-curve as a result of the kinetic damage evolution process.

The rate-dependent cohesive zone model predicts different load-displacement responses as shown in Fig. 2.12a for different global separation rates ($t_1/t_0 = 10^{11}, 10^{10}, 10^9$), and the corresponding R-curves are shown in Fig. 2.12b. With the same parameters for an interface, ($t_0, K_0, \varepsilon_0, \sigma_c$), as the applied separation rate increases (t_1/t_0 decreasing), the normalized peak force increases and the interface shows more resistance to crack growth, with both the initiation and steady-state J-integrals increasing, similar to the R-curves obtained from the DCB experiments.

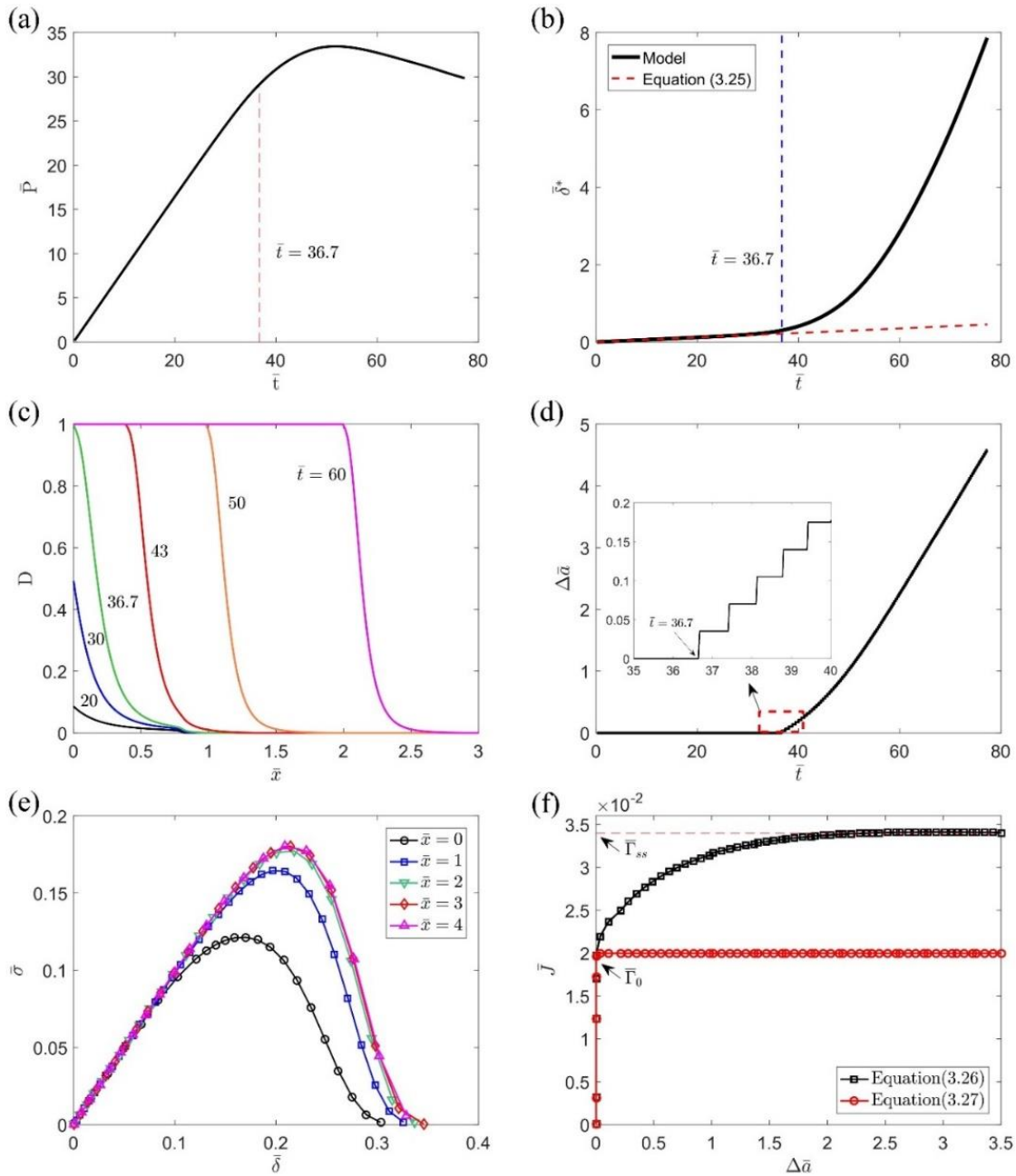


Figure 2.10 Numerical results from the rate-dependent DCB model: (a) load-time response; (b) crack-tip opening displacement; (c) damage parameters along the interface at different times; (d) crack growth; (e) traction-separation relations at different locations along the interface; (f) normalized J-integral versus the change of crack length as the fracture resistance curve obtained by equations (2.26) and (2.27).

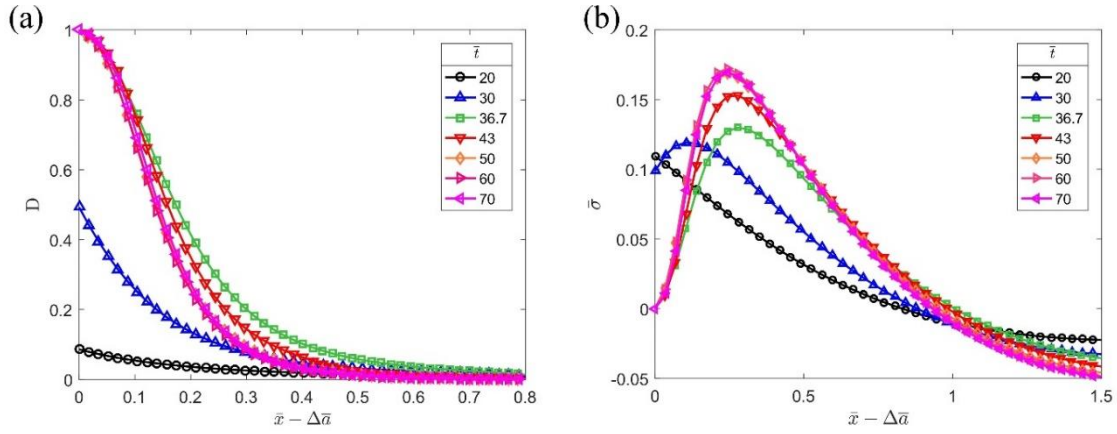


Figure 2.11 (a) Damage evolution and (b) normal traction distributions along the interface with the origin at the crack tip as the crack grows.

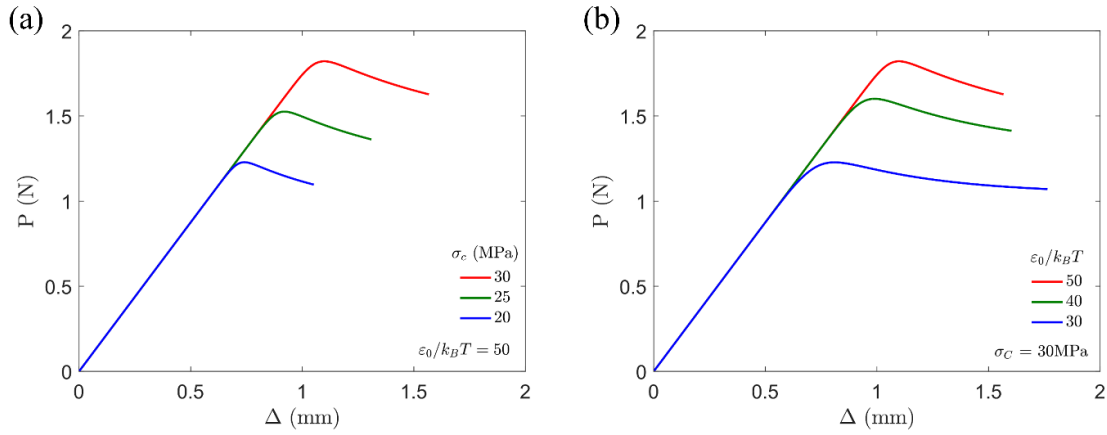


Figure 2.12 Effect of (a) the critical stress and (b) the bond energy on the load-displacement responses of DCB specimens by the rate-dependent DCB model.

2.3 Results and Discussion

A total of 17 DCB specimens were used in experiments with at least 3 specimens for each of the 5 applied separation rates (Table 2.2). The load-displacement response was measured for each specimen (Fig. 2.13), and Fig. 2.14a features five of them, one for each separation rate. In Section 2.2, we presented three methods to analyze the DCB experiments. First, a direct method based on the beam on elastic foundation (BEF) model

can be used to estimate the crack growth and the J-integral. The stiffness of the elastic foundation was determined by fitting the linear portion of the load-displacement curve (Fig. 2.5a) for each specimen. The results show similar stiffness for different separation rates (Table 2.2 and Fig. 2.15a), and the average value, $K_0 = (7.5 \pm 0.5) \times 10^{12} \text{ N/m}^3$, was then used as the rate-independent stiffness for the subsequent analyses. We note that, by Eq. (2.2), the initial slope of the load-displacement response (Fig. 2.14a) depends on the initial crack length, which varies from specimen to specimen. In addition, the critical value of the J-integral for initiation of crack growth (Γ_0) and the steady-state fracture toughness (Γ_{ss}) can be estimated directly from the resistance curves (Fig. 2.14b) following the procedure presented in Section 2.2.2 (Fig. 2.5). Then, the strength of the interface can be estimated as $\sigma_0 = \sqrt{2K_0\Gamma_0}$ assuming a bilinear traction-separation relation (Fig. 2.6). The results for all specimens are summarized in Table 2.2. Furthermore, we plot the interfacial properties versus the epoxy thickness at each separation rate (Fig. 2.15). Based on these results, we find: (1) the stiffness (K_0) is independent of the rate or the epoxy thickness (Fig. 2.15a), and thus can be treated as a constant; (2) the steady-state toughness (Γ_{ss}) and the interfacial strength (σ_0) are independent of epoxy thickness (Fig. 2.15b-c) but depend on the separation rate (Fig. 2.14c-d); (3) there is no clear dependence of the difference between Γ_0 and Γ_{ss} on the epoxy thickness (Fig. 2.15d). Overall, the epoxy thickness has a negligible effect on the interfacial properties obtained by the direct method. For all the specimens, the obtained values for the interfacial strength are well below the expected yield strength of the epoxy of $\sim 36 \text{ MPa}$. Therefore, we do not expect any significant plastic deformation in the epoxy. On the other hand, if the strength of the interface were higher than the strength of epoxy, similar to the cases considered by Tvergaard and Hutchinson [132], large-scale yielding of the epoxy would be expected and the results would then depend on the epoxy thickness. Moreover, since the epoxy is in its glassy state at the room

temperature, the effect of bulk viscoelasticity is negligible, and thus the rate dependency is primarily due to the interfacial fracture process.

The values of K_0 , σ_0 , and Γ_{ss} obtained from the BEF analysis provide the first guess for a bilinear traction-separation relation for each specimen. Then, by the iterative method (Section 2.2.3), we adjusted the values of σ_0 and Γ_{ss} in the finite element simulations to best fit the load-displacement responses (Fig. 2.16), although the same stiffness, $K_0 = 7.5 \times 10^{12} \text{ N/m}^3$, was used in all cases. The traction-separation relations thus obtained are rate dependent as shown in Fig. 2.14e for the five specimens corresponding to those in Fig. 2.14a (specimens no. 1, 8, 9, 13, 16 in Table 2.2). Similar to the BEF results, both the strength and toughness of the silicon/epoxy interface increased as the applied separation rate increased (Fig. 2.14c-d).

The increase in interfacial toughness and strength with increasing separation rate is interesting because the epoxy being considered here is in its glassy state and the toughness of bulk epoxy specimens decreases with separation rate [6]. The results presented here for interfacial fracture parallel those presented in Rakestraw, et al. [109] for steel/epoxy interfaces. Thus, it appears that the noted rate dependence may be related to an interphase region [40, 133-137] or the pullout of epoxy ligaments [130, 138]. In either of these scenarios, bond rupture must be a feature of interfacial failure.

For the third method, we proposed a rate-dependent cohesive zone model based on the kinetic bond rupture mechanism (Section 2.2.4) and solved the DCB problem numerically (Section 2.2.5). Ideally, with four parameters, $(t_0, K_0, \varepsilon_0, \sigma_c)$, this model should be able to explain and predict the rate-dependent fracture of a specific interface (e.g., the silicon/epoxy interface) in all specimens. However, in order to fit the experimental data, one of the four parameters (σ_c) had to be adjusted, whereas the other

three are constants. In particular, the stiffness is the same as that obtained by the BEF analysis: $K_0 = 7.5 \times 10^{12} \text{ N/m}^3$. The microscopic time scale is set by the temperature, $t_0 = \hbar/(k_B T)$ ($\sim 10^{-13} \text{ s}$). The bond energy ε_0 is found to be around 1.5 eV for all specimens. The values of the critical stress are listed in Table 2.3. Figure 2.14a shows the comparison of the load-displacement responses between the numerical results and the experiments for the five specimens at different separation rates. Similar comparisons for all specimens are shown in Fig. 2.13.

The bond energy of 1.5 eV is somewhat lower than the values associated with Si-C and Si-H bonds at 4.35 and 2.98 eV, respectively. The extracted critical stress values ranging from 14 to 25 MPa are also lower than the 36 MPa yield strength of this epoxy. These comparisons suggest that the interfacial bonds are not all covalent bonds and could be a mixture of primary and secondary bonds. In addition, bond breaking models that are targeted at specific bonds, as identified, for example, by X-Ray Photoelectron spectroscopy of fracture surfaces [130] may reconcile some of the differences noted here.

The critical stress of the interface may depend on the local separation rate. As noted in Fig. 2.10b, by the rate-dependent cohesive zone model, the local separation rate at the initial crack tip (δ^*) is nearly a constant up to the initiation of crack growth. According to Eq. (2.25), the local separation rate depends on the initial crack length (a_0) of the DCB specimen and the applied separation rate ($\dot{\Delta}$). By plotting the critical stress versus the local separation rate for all specimens as shown in Fig. 2.17, we observe an interesting transition: the critical stress is approximately constant at low and high separation rates, but undergoes a transition from about 15.5 MPa to 24.5 MPa for the intermediate separate rates (from 2 to 10 $\mu\text{m/s}$). This transition suggests possibly different mechanisms for the critical stress

at the low and high separation rates, which could be related to other mechanisms such as chain pull-out [100, 101].

With the rate-dependent cohesive zone model, the traction-separation relations at the initial crack tip are shown in Fig. 2.14f for the five specimens in comparison with the bilinear traction-separation relations in Fig. 2.14e. As noted in Fig. 2.10e, the traction-separation relation at the steady-state is different from that at the initial crack tip. Consequently, both the peak stress and the fracture toughness corresponding to the steady-state traction-separation relations are higher than those at the initial crack tip. Fig. 2.14c compares the steady-state fracture toughness obtained by all three methods and Fig. 2.14d compares the peak stress, both plotted versus the separation rate ($\dot{\Delta}$) applied at the opening end of the DCB specimen. More appropriately, the interfacial properties are plotted versus the local separation rate ($\dot{\delta}^*$) in Fig. 2.18.

The fracture toughness and strength obtained by the three methods are comparable overall. The BEF model allowed direct extraction of the interfacial properties, although the damage process during fracture was not explicitly accounted for. By assuming a bilinear traction-separation relation, the iterative method considers the damage process in a particular way, with which the numerical results by finite element analyses could fit the experimental data very well. However, as a phenomenological model, the parameters of the bilinear traction-separation relation must be determined for each specific separation rate and may be limited to specific specimen geometry. Thus, without any specific underlying mechanisms, the phenomenological model would not be predictive of the rate dependence.

By assuming a thermally activated bond rupture mechanism, we have proposed a rate-dependent cohesive zone model, which can be used to explain the rate dependence in

the DCB experiments and may be used to predict time and rate-dependent failure of the same interface in other geometries. The comparison with the DCB experiments is promising, although one of the four parameters had to be adjusted for different rates. This caveat may be related to statistical uncertainties with the specimen, where the interfacial bonds may not be identical or intact in all specimens as prepared. It is also possible that other mechanisms not considered in this model may be at play. Nevertheless, the proposed model is intrinsically rate dependent, and the DCB experiments provided clear evidence of similar rate dependency but also revealed the necessity of considering additional mechanisms in order to fully understand the rate-dependent fracture of the specific interface.

Table 2.2 Values of the rate-dependent properties of the silicon/epoxy interface associated with the bilinear traction-separation relations obtained from the BEF analysis

$\dot{\Delta}$ (mm/s)	Specimen No.	h_e (μm)	a_0 (mm)	K_0 ($\times 10^{12} \text{N/m}^3$)	Γ_0 (J/m ²)	Γ_{ss} (J/m ²)	σ_0 (MPa)
0.042	1	1.2	12.2	7.5	3.9	7.8	7.7
	2	5.1	12.9	6.6	5.3	6.5	8.4
	3	13.3	15.8	7.1	6.8	8.6	9.8
	4	39.3	13.4	7.5	6.1	7.3	9.5
0.42	5	8.0	12.3	8.1	8.0	11.5	11.4
	6	10.2	13.1	6.9	8.1	10.5	10.6
	7	22.0	13.9	7.5	7.1	9.0	10.3
	8	25.7	17.8	6.8	8.0	10.0	11.0
2.1	9	4.5	21.8	7.7	12.5	19.0	13.7
	10	5.1	23.7	6.9	11.0	15.0	12.3
	11	10.2	16.6	6.5	15.5	20.3	14.2
4.2	12	2.5	22.3	8.7	14.0	19.0	15.6
	13	9.0	21.3	8.1	15.4	21.3	15.2
	14	10.8	18.8	6.0	18.7	22.5	15.0
8.5 ²	15	5.7	17.3		20.9	22.0	17.7
	16	7.6	19.1	7.5	20.0	23.8	17.3
	17	19.1	17.6		20.5	24.5	17.5

² For the case with $\dot{\Delta}=8.5$ mm/s, the initial crack length was not measured directly. Instead, it was determined by Eq. (2.21) using the average stiffness of the interface, $K_0 = 7.5 \times 10^{12}$ N/m³, along with the initial slope of the load-displacement response.

Table 2.3 Values of the parameters for the silicon/epoxy interface associated with the rate-dependent cohesive zone model

$\dot{\Delta}$ (mm/s)	Specimen No.	h_e (μm)	a_0 (mm)	K_0 ($\times 10^{12} \text{N/m}^3$)	Γ_0 (J/m ²)	Γ_{ss} (J/m ²)	σ_0 (MPa)
0.042	1	12.2	0.256	15.7	6.66	7.50	9.68
	2	12.9	0.230	14.4	6.12	6.88	8.91
	3	15.8	0.264	16.3	6.91	7.78	10.1
	4	13.4	0.244	15.2	6.44	7.26	9.40
0.42	5	15.6	2.52	18.0	9.55	10.7	11.8
	6	13.1	2.24	17.3	9.60	10.3	11.3
	7	13.9	2.00	16.0	8.51	9.48	10.5
	8	17.8	1.25	17.0	8.56	9.92	11.0
2.1	9	21.8	4.24	22.3	15.9	18.3	14.8
	10	12.7	3.61	20.5	14.6	16.8	13.6
	11	16.6	7.14	22.7	16.4	18.9	15.2
4.2	12	17.3	8.11	22.8	17.9	20.6	15.4
	13	21.3	8.86	23.5	18.6	21.3	15.9
	14	18.8	11.3	24.3	19.3	22.1	16.5
8.5	15	17.3	26.7	24.2	20.1	23.0	16.8
	16	19.1	22.1	24.7	20.4	23.3	17.0
	17	17.6	25.9	24.5	20.5	23.3	16.9

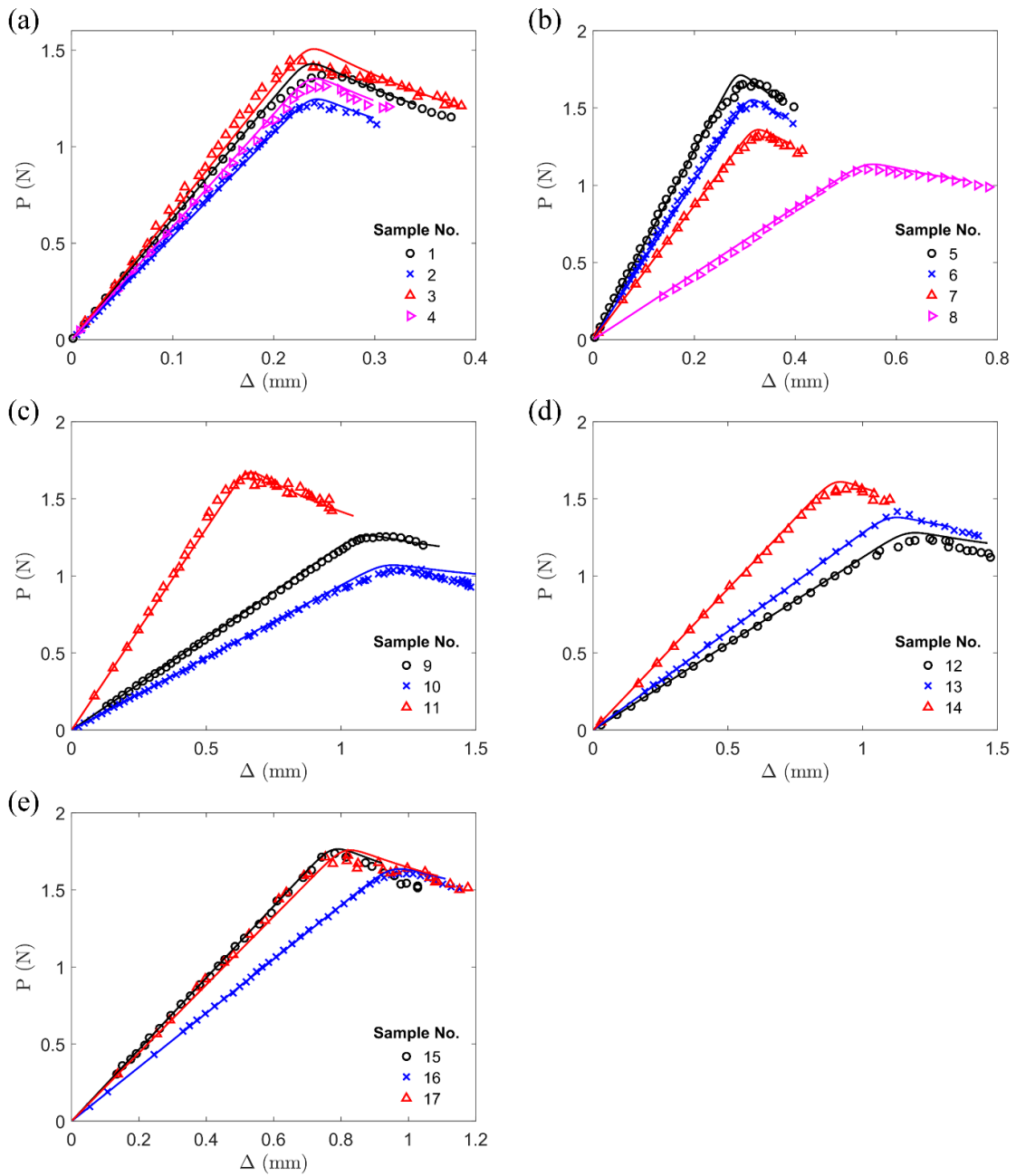


Figure 2.13 The load-displacement responses of all specimens, comparing the experimental data (markers) and the numerical results by the rate-dependent DCB model (lines): (a-e) DCB specimens with five applied separation rates: 0.042 mm/s, 0.42 mm/s, 2.1 mm/s, 4.2 mm/s, and 8.4 mm/s.

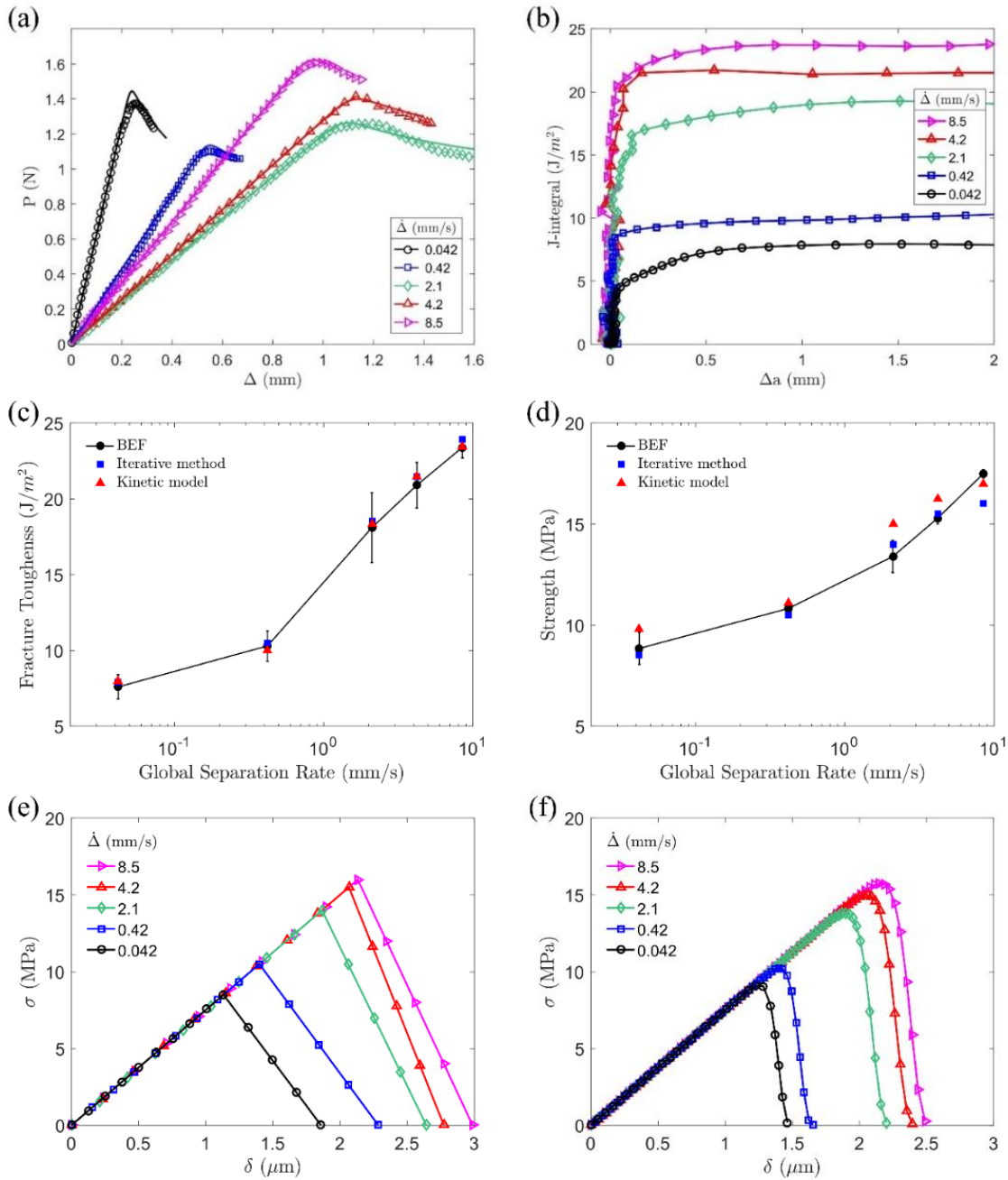


Figure 2.14 (a) Load-displacement curves of five specimens with different separation rates, symbols for the measured data and solid lines for the numerical results obtained by the rate-dependent DCB model; (b) Resistance curves for different separation rates by the BEF analysis. Rate dependence of (c) steady-state fracture toughness and (d) interfacial strength obtained by the three methods (the BEF results were averaged over all specimens at each

separation rate with error bars showing the standard deviations). (e) Bilinear traction-separation relations obtained by the iterative method; (f) Crack tip traction-separation relations obtained by the rate-dependent DCB model.

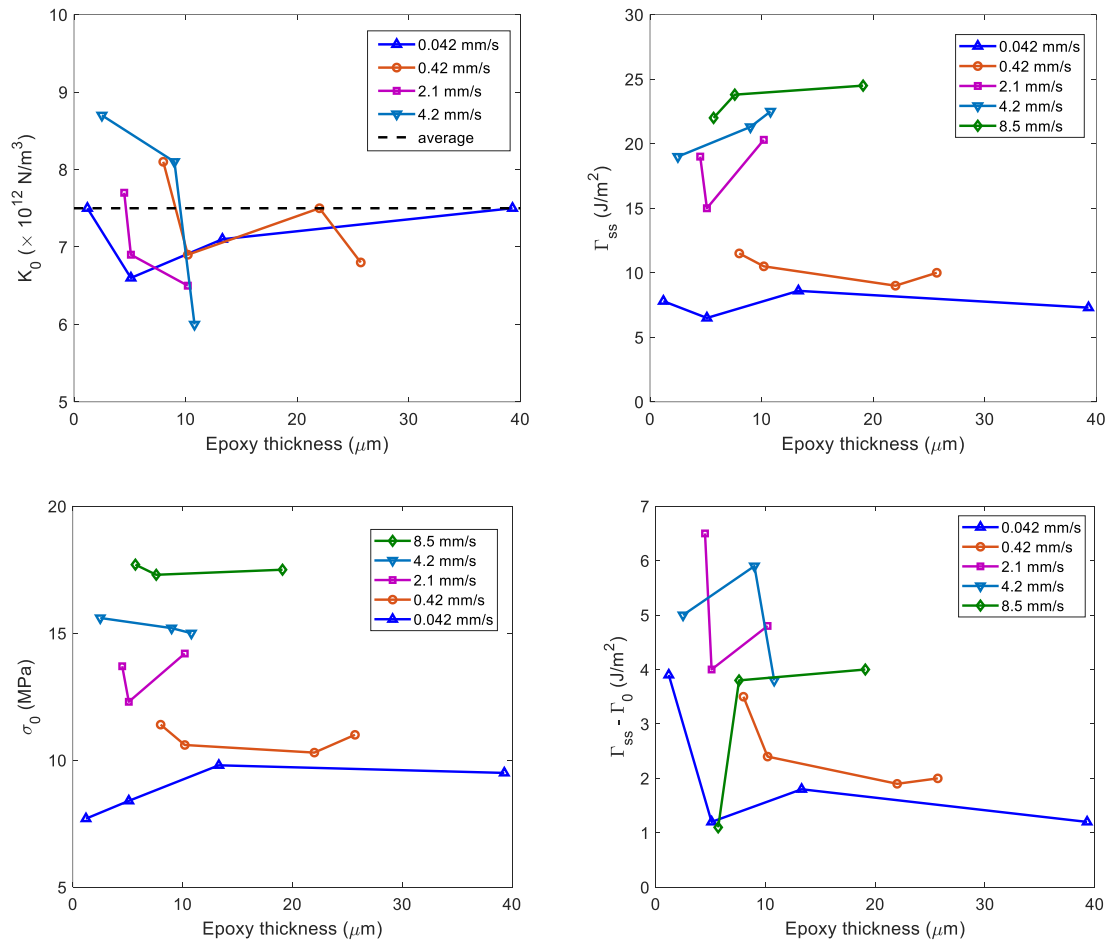


Figure 2.15 Plot the effects of epoxy thickness on the extracted stiffness (K_0), steady-state toughness (Γ_{ss}), and strength (σ_0) from the BEF analysis. Evidently, the epoxy thickness has little effect on the extracted properties. On the other hand, the toughness and strength are both rate dependent, whereas the stiffness is rate independent.

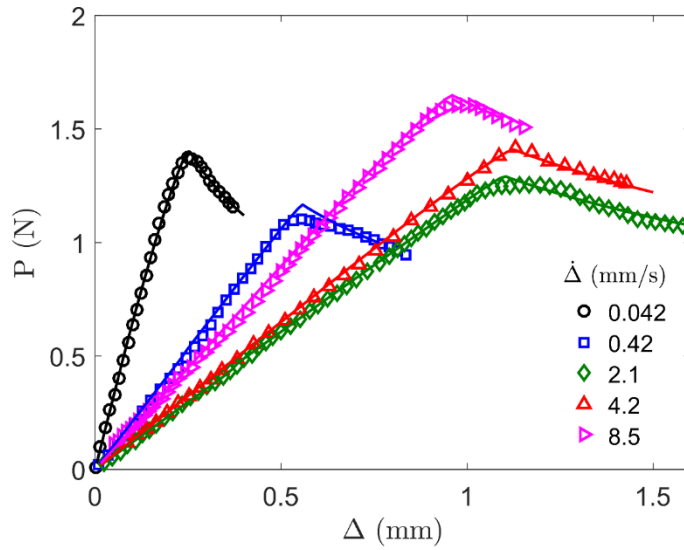


Figure 2.16 The load-displacement responses of five specimens at different applied separation rates, comparing the experimental data (markers) and the numerical results by the iterative method (lines).

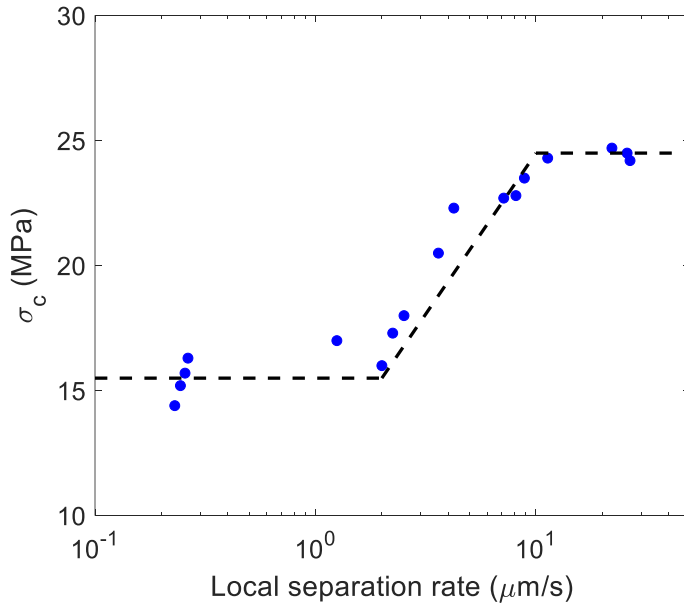


Figure 2.17 The critical stress of the interface versus the local separation rate for all specimens.

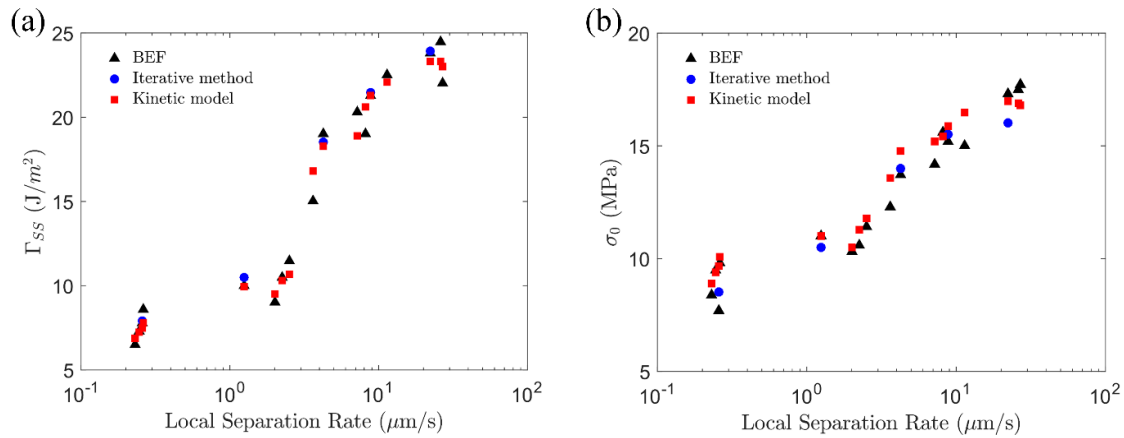


Figure 2.18 (a) Steady-state fracture toughness and (b) interfacial strength obtained by the three methods, versus the local separation rates at the crack tip.

2.4 Summary

Silicon/epoxy/silicon sandwich specimens were loaded under nominally mode I conditions over a range of separation rates with a view to examining the rate-dependent fracture of the silicon/epoxy interface. Three methods are used to extract the interfacial properties, including a direct method based on the BEF model, an iterative method with bilinear traction-separation relations, and an intrinsically rate-dependent cohesive zone model. The key findings are summarized as follows.

- The BEF model allowed direct extraction of the interfacial properties, although the damage process during fracture was not explicitly accounted for. The obtained fracture resistance curves are rate dependent for the DCB specimens, with both the steady-state toughness and the strength increasing as the applied separation rate increased.
- By assuming a bilinear traction-separation relation, the iterative method considers the damage process in a particular way, with which the numerical results by finite element analyses could fit the experimental data very well. Similar to the BEF results, both the

strength and toughness of the silicon/epoxy interface increased as the applied separation rate increased. However, as a phenomenological model, the parameters of the bilinear traction-separation relation must be determined for each separation rate and may be limited to specific specimen geometry. Without considering any specific mechanisms, such a phenomenological model does not have the capability of predicting the rate dependence.

- A specific mechanism is considered for the intrinsically rate-dependent cohesive zone model. As a fundamental departure from the typical cohesive zone models, the damage evolution is a kinetic process based on thermally activated bond rupture with a microscopic time scale. As a result, the predicted traction-separation relation depends on the local separation rate, with both the toughness and the strength increasing as the local separation rate increased.
- The DCB problem was solved numerically by incorporating the rate-dependent cohesive zone model. Interestingly, the predicted traction-separation relation varies along the interface from the initial crack tip to a particular distance until it reaches a steady state. This is in stark contrast with a typical cohesive zone model that assumes an identical traction-separation relation everywhere along the interface for each specimen. Consequently, rate-dependent fracture resistance curves are predicted by the proposed model, with the J-integral for crack initiation corresponding to the traction-separation relation at the initial crack tip and the steady-state toughness corresponding to the steady-state traction-separation relation at a location ahead of the initial crack tip.
- Ideally, with four parameters, $(t_0, K_0, \varepsilon_0, \sigma_c)$, the proposed rate-dependent cohesive zone model should be able to explain and predict the rate-dependent fracture of a specific interface (e.g., silicon/epoxy interface). However, to fit the experimental data,

one of the four parameters (σ_c) had to be adjusted. The critical stress (σ_c) is approximately constant at low and high separation rates, but undergoes a transition from about 15.5 MPa to 24.5 MPa for the intermediate local separate rates (from 2 to 10 $\mu\text{m/s}$).

- Finally, the rate-dependent cohesive zone model offers a promising step toward modeling rate-dependent fracture of interfaces. In addition, the same model could be used to study time or history dependent fracture such as delayed fracture under static loading and fatigue crack growth under cyclic loading conditions. In the next chapter, we continue the development of a multiscale mechanism-based model for rate-dependent fracture of interfaces with specific molecular structures.

Chapter 3 A Multiscale Mechanism-based Model for Rate-dependent Interfacial Fracture

Rate-dependent fracture and adhesion have been observed for a silicon/epoxy interface (Chapter 2), where both the interfacial strength and adhesion energy (or fracture toughness) increase with the separation rate, while the opposite is true for the bulk epoxy in its glassy state. Motivated by this observation, we propose a modeling framework for the multiscale interfacial fracture processes, consisting of four integrated levels (Fig. 3.16): bond level (energetics), chain level (entropy), interface level (traction-separation relation with statistical chain length distributions), and specimen level (load-displacement and crack growth). The framework is more than a determinate model with certain fitting parameters. Instead, each level can be considered independently with various modelling candidates (e.g., different bond or chain models) and then integrated with the other levels. As a result, this model relates the macroscopically measurable interfacial properties (toughness, strength, and traction-separation relations) to the molecular structures at the interface, and the rate dependence develops naturally from the kinetics of damage evolution via the statistical concept of bond/chain survival probability. The modeling results are compared to the DCB experiments presented in Chapter 2 as well as new data from the dual actuator loading device (Chapter 4). With a few parameters for the underlying molecular structures, the model is able to reproduce the rate-dependent fracture of the silicon/epoxy interface and predict fracture under other loading conditions (e.g., cyclic loading). This multiscale, mechanism-based model thus offers a promising approach for modeling the rate-dependent fracture and adhesion of polymers and soft materials.

3.1 Bond level: Lennard-Jones potential

The interaction between two atoms, often visualized as a bond, can be characterized by a minimum of two parameters: the equilibrium bond length r_0 and the bond energy ε_0 . When the bond length is stretched to an arbitrary length r , the potential energy of the bond (U_b) can be written as a function of the bond stretch, $\lambda_b = r/r_0$. For example, the well-known Lennard-Jones (LJ) potential function can be written as

$$U_b(\lambda_b) = \varepsilon_0(\lambda_b^{-12} - 2\lambda_b^{-6}) \quad (3.1)$$

The interaction force between the two atoms can be obtained from the potential energy function as $f_b = \frac{\partial U_b}{\partial r}$, which can also be written as a function of the bond stretch. Using the LJ potential, we obtain

$$f_b(\lambda_b) = \frac{12\varepsilon_0}{r_0}(\lambda_b^{-7} - \lambda_b^{-13}) \quad (3.2)$$

When the bond is slightly stretched, the potential energy is often approximated by assuming a linear spring constant as the bond stiffness. With the same bond stiffness as the LJ potential at $\lambda_b = 1$, the approximate potential energy is:

$$U_b(\lambda_b) \approx \varepsilon_0[36(\lambda_b - 1)^2 - 1] \quad (3.3)$$

and the corresponding bond force is linear, namely

$$f_b(\lambda_b) \approx \frac{72\varepsilon_0}{r_0}(\lambda_b - 1) \quad (3.4)$$

A slightly different approximation was recently suggested by Mao and Anand [124], where the potential energy is taken as a quadratic function of the logarithmic strain:

$$U_b(\lambda_b) \approx \varepsilon_0[36(\ln\lambda_b)^2 - 1] \quad (3.5)$$

and the corresponding bond force is nonlinear:

$$f_b(\lambda_b) \approx \frac{72\varepsilon_0}{r_0} \frac{\ln\lambda_b}{\lambda_b} \quad (3.6)$$

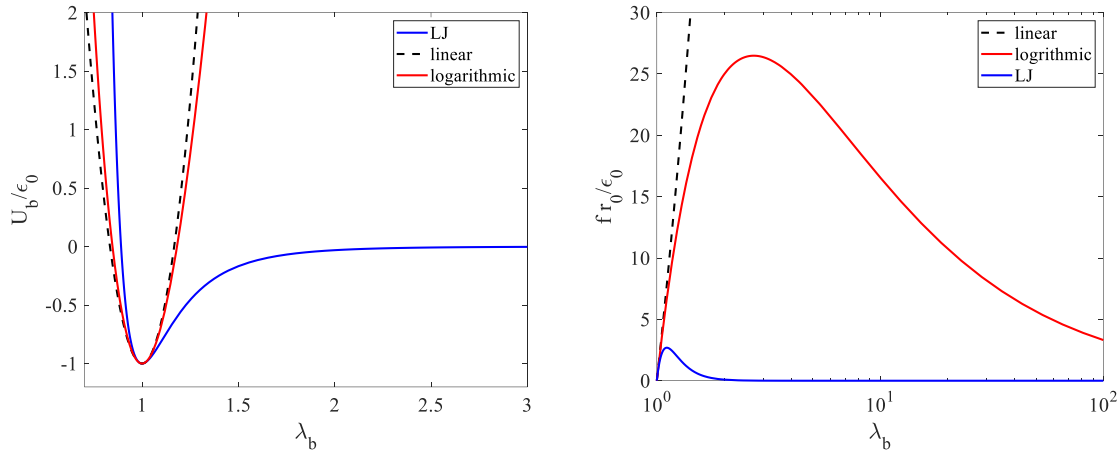


Figure 3.1 Comparison of the LJ potential and two approximations: (a) the potential energy; (b) the bond force.

In Fig. 3.1, we compare the LJ potential and the two approximations, where the normalized bond energy ($\bar{U}_b = U_b/\epsilon_0$) and force ($\bar{f}_b = f_b r_0/\epsilon_0$) are plotted versus the bond stretch. The LJ potential has three key features that are common for essentially all types of bonds: (1) the bond energy is minimized at an equilibrium distance ($r = r_0$ or $\lambda_b = 1$); (2) the bond energy becomes infinitely high as the two atoms approach each other ($r \rightarrow 0$ or $\lambda_b \rightarrow 0$); (3) the bond energy approaches zero as the two atoms are separated far apart from each other ($r \rightarrow \infty$ or $\lambda_b \rightarrow \infty$). As a result, the corresponding bond force first increases and then decreases toward zero as the bond stretch increases, and the work done by the force to break the bond equals the bond energy ϵ_0 . The linear spring approximation has only one of the three features and is valid only near the equilibrium state ($r \approx r_0$ or $\lambda_b \approx 1$). On the other hand, the logarithmic approximation retains the first two features, but the bond energy is unbounded as $r \rightarrow \infty$. Interestingly, the bond force by the logarithmic approximation does approach zero as $r \rightarrow \infty$, but with a much higher peak force (at $\lambda_b = e$) and much slower softening in comparison to the bond force by the LJ potential. In the remainder of this chapter, we use the LJ potential as a simple but generic

model for the bonds, although other potential functions for specific bonds can be used as well.

3.2 Chain level: A modified freely jointed chain model

Next consider a chain of bonds. Following the freely jointed chain (FJC) theory [122], the free energy of a single chain with n bonds is

$$\psi = nk_B T \left(\frac{l}{nr_0} \beta + \ln \left(\frac{\beta}{\sinh \beta} \right) \right) \quad (3.7)$$

where $\beta = \mathcal{L}^{-1}(l/(nr_0))$ and \mathcal{L}^{-1} is the inverse Langevin function; l denotes the average end-to-end distance of the chain. The classical FJC model assumes that each bond is a rigid link of length r_0 (Kuhn segment) so that the free energy is entirely entropic. We extend this model by relaxing the rigid-bond assumption and replacing r_0 with $r = \lambda_b r_0$, where λ_b is the bond stretch. In addition, we include as part of the free energy function the internal energy associated with the bond stretching [123]. The modified free energy is thus

$$\psi = nU_b(\lambda_b) + nk_B T \left(\frac{\lambda}{\lambda_b} \beta + \ln \left(\frac{\beta}{\sinh \beta} \right) \right) \quad (3.8)$$

with $\beta = \mathcal{L}^{-1}(\lambda/\lambda_b)$ and $\lambda = l/(nr_0)$ (called chain stretch).

Eq. (3.8) recovers Eq. (3.7) if $\lambda_b \equiv 1$ (rigid bonds) except for a constant internal energy term. To determine the bond stretch, the free energy in Eq. (3.8) is minimized by a value of λ_b as the equilibrium state at a prescribed chain stretch λ . Thus, we obtain λ_b as a function of λ by setting $\partial\psi/\partial\lambda_b = 0$, which yields

$$\frac{1}{k_B T} \frac{dU_b}{d\lambda_b} = \frac{\lambda}{\lambda_b^2} \mathcal{L}^{-1} \left(\frac{\lambda}{\lambda_b} \right). \quad (3.9)$$

As a result, the free energy is a function of the chain stretch, namely, $\psi = \psi(\lambda)$. Then, to maintain the chain stretch λ , the force applied at the ends of the chain can be obtained by

$$f = \frac{1}{nr_0} \frac{d\psi}{d\lambda} = \frac{k_B T}{\lambda_b r_0} \mathcal{L}^{-1} \left(\frac{\lambda}{\lambda_b} \right). \quad (3.10)$$

We note that, by Eqs. (3.9) and (3.10), the chain force and the bond force are related as: $f = \frac{\lambda_b}{\lambda r_0} \frac{dU_b}{d\lambda_b} = \frac{\lambda_b}{\lambda} f_b$.

We use the LJ potential (Eq. (3.1)) and the logarithmic approximation (Eq. (3.5)) for the bonds in this section to illustrate the modified FJC model. First, with the LJ potential, the bond stretch (λ_b) is shown in Fig. 3.2a as a function of the chain stretch (λ) for different values of the normalized bond energy ($\bar{\varepsilon} = \varepsilon_0/k_B T$), and correspondingly, the normalized end force ($\bar{f} = f r_0/k_B T$) applied to the chain is shown in Fig. 3.2b. When the normalized bond energy is relatively high (e.g., $\bar{\varepsilon} = 100$), the bond stretch remains nearly 1 (un-stretched) until the chain stretch reaches nearly 1, similar to the classical FJC model. However, unlike the classical FJC model where the chain stretch λ is always less than 1 with $\lambda_b \equiv 1$ (rigid bonds), the modified FJC model allows the chain stretch λ to be greater than 1 as the bond stretch increases almost linearly when $\lambda > 1$ for the case of $\bar{\varepsilon} = 100$. Correspondingly, the normalized force first increases slowly for $\lambda < 1$, primarily due to the entropic effect. As λ approaches 1, the chain stiffens and transitions to a response primarily due to the bond stretch, with a peak force followed by softening as a result of the LJ potential. When the normalized bond energy is relatively low (e.g., $\bar{\varepsilon} = 10$), the overall behavior is similar, but the bond stretch is larger at the same chain stretch. Interestingly, there exists a critical chain stretch (λ_{\max}), beyond which the free energy cannot be minimized by any value of the bond stretch. The critical chain stretch decreases as the normalized bond energy decreases and could be less than 1 for a very low bond

energy (e.g., $\bar{\epsilon} = 1$). In such cases, the bonds can be easily stretched, and the increase of the bond energy is small compared to the decrease of the entropic free energy. The competition between the two parts of the free energy (bond stretching vs entropic) also leads to an unstable solution for the bond stretch in Fig. 3.2a (dashed lines), where the free energy is locally maximized.

We compare the modified FJC model to two classical chain models, Gaussian and Langevin, both purely entropic with no contribution from bond stretching. The Gaussian chain model predicts a linear response, $\bar{f} = 3\lambda$, shown as the dotted line in Fig. 3.2b (inset). Independent of the normalized bond energy, the predictions by the modified FJC model agree with the Gaussian model when the chain stretch is very small ($\lambda \ll 1$). On the other hand, the Langevin model predicts a nonlinear response with a limiting stretch ($\lambda < 1$): $\bar{f} = \mathcal{L}^{-1}(\lambda)$, shown as the dashed line in Fig. 3.2b. The modified FTC model would recover the Langevin model if the normalized bond energy is infinitely large ($\bar{\epsilon} \rightarrow \infty$). For a relatively large bond energy ($\bar{\epsilon} = 100$), the modified FJC model is similar to the Langevin model when $\lambda < 1$, but the chain can be stretched further with the increasing bond stretch. For $\lambda > 1$, the chain behavior is dominated by bond stretching, with $\bar{f} = 12\bar{\epsilon}(\lambda^{-7} - \lambda^{-13})$ by the LJ potential. Thus, the modified FJC model predicts a transition from Langevin to LJ. When the bond energy is relatively small ($\bar{\epsilon} = 1, 10$), the effect of bond stretching competes with the entropic effects at small stretches ($\lambda < 1$), leading to a more compliant chain response.

With the logarithmic approximation (Eq. (3.5)) for the bonds in the modified FJC model, the bond stretch (Fig. 3.3a) and the normalized end force (Fig. 3.3b) are shown as functions of the chain stretch. Again, the predicted chain responses agree with the Gaussian model when the chain stretch is very small ($\lambda \ll 1$). When the normalized bond energy is

relatively high (e.g., $\bar{\epsilon} = 100$), the modified FJC model predicts a transition from the entropic Langevin response to predominantly bond stretching with the logarithmic potential energy. The transition becomes more gradual as the normalized bond energy decreases, but remains in place even for very small bond energy ($\bar{\epsilon} = 1$). Differing from the LJ potential, the logarithmic potential energy allows much larger bond stretches and much higher bond forces, leading to much larger chain stretches and peak forces. In this case, there is no maximum chain stretch, but there is a maximum force as the bond force softens after a peak.

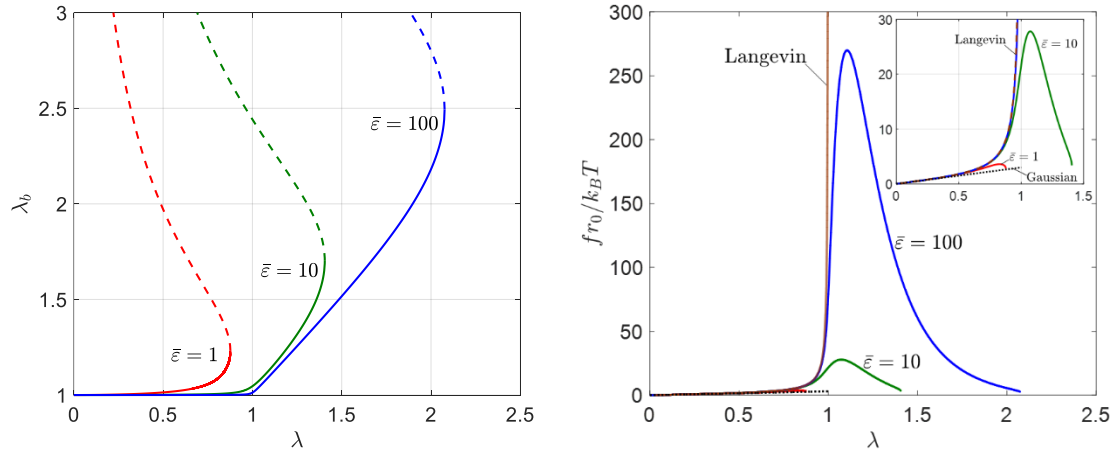


Figure 3.2 Modified FJC model with the LJ potential for the bonds: (a) bond stretch versus chain stretch and (b) end force versus chain stretch.

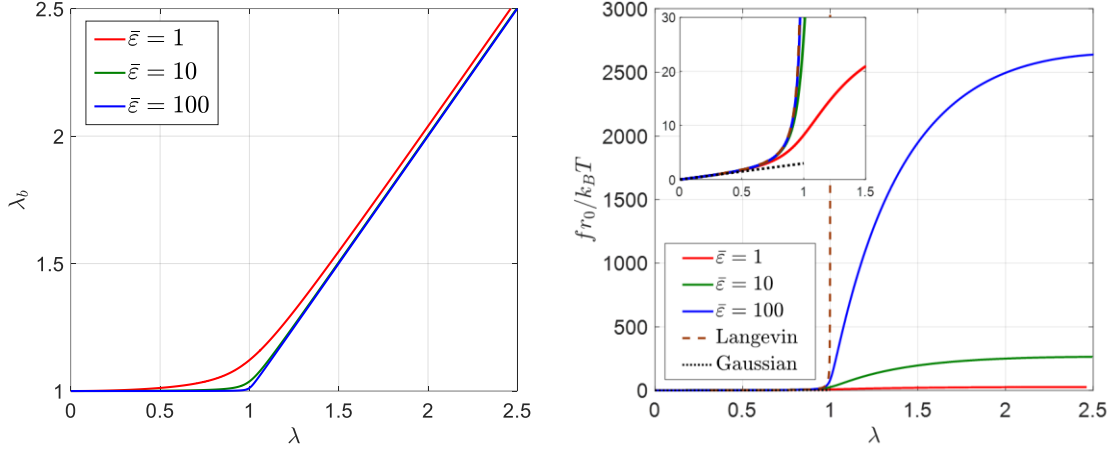


Figure 3.3 Modified FJC model with the logarithmic potential for the bonds: (a) bond stretch versus chain stretch and (b) end force versus chain stretch.

3.3 Interface level: Thermally activated damage process

Previous studies have considered the kinetics of thermally activated bond rupture in various materials and interfaces [116, 117, 119, 139]. Following the similar idea, we present here a kinetic model for thermally activated chain breaking. Consider a chain of n bonds subject to an external force f . The Gibbs free energy of the system including the chain and the external force can be written as

$$\phi = \psi(\lambda) - fl. \quad (3.11)$$

where $\psi(\lambda)$ is given in Eq. (3.8) by the modified FJC model and $l = nr_0\lambda$ is the end-to-end length of the chain (projected in the direction of the force).

For the modified FJC model with the LJ potential for the bonds (Fig. 3.2), there exists a maximum chain stretch (λ_{max}), beyond which an equilibrium bond stretch does not exist. Thus, for $\lambda > \lambda_{max}$, the chain must be broken and the Gibbs free energy becomes

$$\phi = -(n - 1)\epsilon_0 - fl, \quad (3.12)$$

where we assume only one of the bonds has been broken and the other bonds return to their equilibrium state with $\lambda_b = 1$; meanwhile, the chain is broken into two free chains with the maximum entropy ($\beta = 0$). Figure 3.4a shows the normalized free energy ($\bar{\phi} = \phi/nk_B T$) as a function of the chain stretch at various values of the normalized force ($\bar{f} = fr_0/k_B T$). When the force is zero ($\bar{f} = 0$), the free energy of the chain is minimized at the equilibrium ground state with $\lambda = 0$ and $\phi = -n\varepsilon_0$, while the broken chain ($\lambda > \lambda_{max}$) has a slightly higher free energy ($\phi = -(n - 1)\varepsilon_0$); in between, the free energy increases with increasing λ and reaches a maximum at $\lambda = \lambda_{max}$. Therefore, the chain at the equilibrium ground state is thermodynamically stable and chain breaking is unlikely with an energy barrier defined by the difference between the minimum and the maximum free energy. When a force is applied to the chain, an equilibrium chain stretch can be found as long as the force is less than a peak force (f_{max}) as shown in Fig. 3.2b. For $0 < \bar{f} < \bar{f}_{max}$, the free energy function has a local minimum (ϕ_{min}) at an equilibrium stretch ($0 < \lambda < \lambda_{max}$), while the free energy of a broken chain ($\lambda > \lambda_{max}$) decreases linearly with increasing λ ; in between, there exists a local maximum (ϕ_{max}) at $\lambda = \lambda_{max}$ or below. In this case, the chain is metastable at the equilibrium stretch ($0 < \lambda < \lambda_{max}$), but the state of a broken chain is thermodynamically favored to lower the free energy. The presence of a local maximum free energy between the two states suggests that chain breaking is possible via a thermally activated process with a finite energy barrier. Considering that a minimum of one bond must be ruptured to break the chain, we define the energy barrier for each bond as:

$$E_b = (\phi_{max} - \phi_{min})/n, \quad (3.13)$$

which is a function of the applied force as shown in Fig. 3.4b. Note that the free energy of a chain as given in Eq. (3.8) is proportional to n , and thus the energy barrier for each bond

is independent of n . As expected, the energy barrier decreases as the force increases. Thus, the action of an external force lowers the energy barrier, making the chain less stable and more likely to break. At zero force ($\bar{f} = 0$), the energy barrier is slightly greater than the bond energy due to the change of entropy from $\lambda = 0$ to $\lambda = \lambda_{max}$ (lower entropy leads to higher free energy). For a given bond energy, the energy barrier becomes zero at $\bar{f} = \bar{f}_{max}$ when chain breaking occurs instantaneously. For $\bar{f} \geq \bar{f}_{max}$, the free energy function decreases monotonically with increasing λ , with no local minimum for an equilibrium stretch. Therefore, the maximum force defines an ultimate strength of the chain, which is required to break the chain instantaneously. We note that both the energy barrier and the maximum force are nearly proportional to the bond energy (ε_0), as shown by re-plotting in the inset of Fig. 3.4b with the energy barrier and the force re-normalized using ε_0 . The results for various bond energy values almost collapse onto one curve, with small differences for relatively low bond energy (e.g., $\bar{\varepsilon} = 10$) due to the entropic effect in the free energy function.

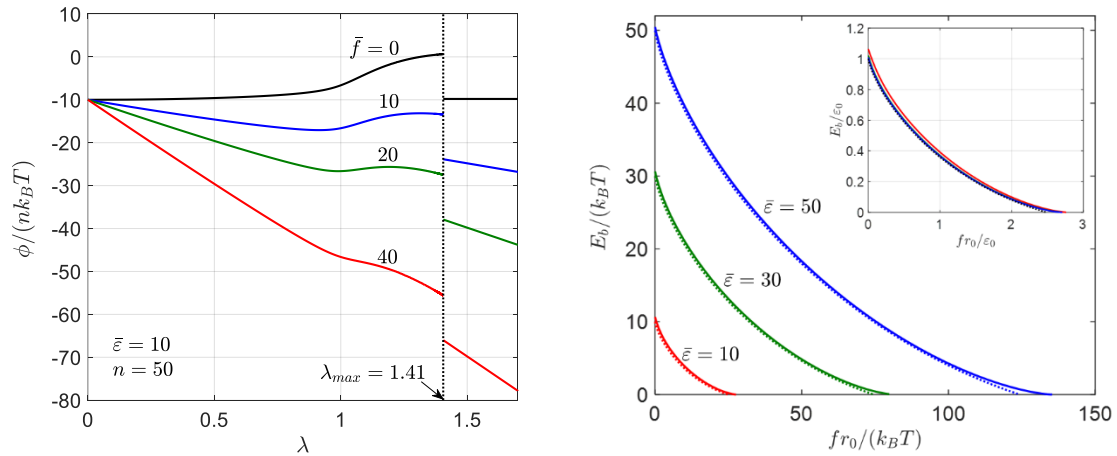


Figure 3.4 (a) Normalized free energy of a chain ($\bar{\varepsilon} = 10$ and $n = 50$) subject to various forces; (b) Normalized energy barrier as a function of the normalized force at various values of the normalized bond energy.

Following the kinetic theory for the strength of solids [116], Bell [117] assumed that the energy barrier for bond breaking decreases linearly with the applied force: $E_b = \varepsilon_0 - \gamma f$, where γ is an empirical parameter ($\gamma = \varepsilon_0/f_{max}$). Similar assumption has been commonly adopted in previous works [110, 139-142]. However, Fig. 3.4b shows that the energy barrier is a nonlinear function of the force. By ignoring the entropic effect, an approximate expression for the energy barrier can be obtained as

$$E_b \approx \varepsilon_0(1 - 1.664\hat{f}^{6/7} + \hat{f} + 0.0236\hat{f}^2) \quad (3.14)$$

where $\hat{f} = fr_0/\varepsilon_0$. The approximation is shown as the dotted lines in Fig. 3.4b. Note that the leading term on the right-hand side (after the constant term) of Eq. (3.14) is nonlinear ($\sim \hat{f}^{6/7}$), which yields an infinite slope at $\hat{f} = 0$. Thus, even for a small force ($\hat{f} \ll 1$), the linear approximation is not justified with this model.

Next consider the probability of chain breaking at the interface level. As noted by Freund [119], the statistics of bond breaking for a large number of nominally identical bonds can be interpreted equivalently as the survival probability of each single bond. The bond survival probability then follows the Arrhenius law as a result of the thermally activated bond breaking process [139], namely

$$\frac{\dot{R}_b}{R_b} = -\frac{k_B T}{\hbar} \exp\left(-\frac{E_b}{k_B T}\right) \quad (3.15)$$

where $\dot{R}_b = dR_b/dt$ is the rate of the bond survival probability (R_b), E_b is the energy barrier for bond breaking as discussed above, $k_B = 1.38 \times 10^{-23}$ J/K (Boltzmann constant), and $\hbar = 6.626 \times 10^{-34}$ J·s (Planck constant). Eq. (3.15) defines a microscopic time scale, $t_0 = \hbar/k_B T \sim 10^{-13}$ s, which is the reciprocal of the natural frequency of atomic oscillations. The right hand side of the Eq. (3.15) is often called bond dissociation (off) rate [117, 119] under the action of a force in a given environment. We

note that the energy barrier normalized by the thermal energy ($k_B T$) determines the rate of bond breaking and the survival probability. When the applied force is small, the energy barrier is high and the bond breaking takes long time. On the other hand, when the force is equal to or greater than the maximum force ($f \geq f_{\max}$), the energy barrier is zero so that the bond dissociation rate is extremely high (similar to atomic oscillations) and the bond breaks almost instantaneously. Eq. (3.15) is essentially the same as Eq. (2.9), but the energy barrier is no longer linear as assumed in Eq. (2.14).

For a chain of n identical bonds, the survival probability of the chain is related to the survival probability of each bond as

$$R_{chain} = R_b^n \quad (3.16)$$

because the chain survives only if all the bonds survive. Thus, the rate equation for the chain survival probability is:

$$\frac{\dot{R}_{chain}}{R_{chain}} = -\frac{n}{t_0} \exp\left(-\frac{E_b}{k_B T}\right) \quad (3.17)$$

Compared to the bond survival probability, the chain survival probability also depends on the chain length (n). The longer the chain, the more likely it breaks under the same thermomechanical conditions.

If an interface consists of a large number of nominally identical chains and is subject to an opening traction (force per unit area of the interface), $\sigma(t)$, some of the chains may have been broken and the others remain intact at a given time. Let $N(t)$ be the number of intact chains per unit area of the interface and $N_0 = N(t = 0)$ be the initial number density. Define the damage of the interface as:

$$D(t) = 1 - \frac{N(t)}{N_0} = 1 - R_{chain}(t) \quad (3.18)$$

Then, the rate equation for damage evolution of the interface is:

$$\frac{dD}{dt} = \frac{n}{t_0} (1 - D) \exp\left(-\frac{E_b}{k_B T}\right), \quad (3.19)$$

which is similar to Eq. (2.11) except for the energy barrier and the time scale (t_0/n).

At any given time, each of the intact chains is subject to a force, $f(t) = \sigma/N$. Thus, the traction can be related to the damage parameter as

$$\sigma = (1 - D)N_0 f(t), \quad (3.20)$$

where the force $f(t)$ can also be related to the chain stretch (Fig. 3.2b) or the opening separation of the interface, $\delta = \lambda n r_0$. Eq. (3.20) is similar to Eq. (2.12) but the force is no longer linearly related to the separation as assumed in Eq. (2.13).

With Eq. (3.10) for the force-stretch relation of a chain, Eq. (3.14) for the energy barrier, Eq. (3.19) for damage evolution, and Eq. (3.20) for the traction, we formulate a multiscale cohesive interface model, which is inherently time dependent, rate dependent and history dependent. Remarkably, such an interface model directly links the traction-separation relation to the underlying molecular structures in terms of the initial chain number density (N_0), the chain length (n) and the bond properties (r_0 and ε_0). Moreover, the thermally activated chain breaking mechanism naturally depends on temperature through both the energetics ($k_B T$ versus E_b) and the kinetics ($t_0 = \hbar/k_B T$). The effect of entropy is also accounted for through the modified FJC model. The same approach may be followed with different bond models and different chain models as parts of the multiscale interface model.

To illustrate how the present model works under various loading conditions, we consider two simple examples. First, subject to a constant traction (σ), the damage

increases over time by Eq. (3.19), the chain force increases by Eq. (3.20), and the energy barrier decreases with increasing chain force (Fig. 3.4b). Eventually, the damage reaches 1, meaning that all the chains have been broken at the interface. Similar to creep and creep rupture, the opening of the interface increases over time and the time to rupture the interface depends on the traction (Fig. 3.5 and Fig. 3.6), respectively. Here, we normalize all quantities as: $\bar{\sigma} = \sigma/\sigma_0$ (with $\sigma_0 = N_0 k_B T/r_0$), $\bar{\delta} = \delta/(nr_0) = \lambda$, and $\bar{t} = nt/t_0$. With this normalization, the results depend on two dimensionless parameters only: $\bar{\sigma}$ and $\bar{\epsilon}$, whereas the chain density (N_0) only affects the magnitude of the stress ($\sigma_0 = N_0 k_B T/r_0$) and the chain length (n) influences both the length scale (nr_0) and the time scale (t_0/n). Figure 3.5a shows that, for each constant traction, the damage first increases slowly and then accelerates towards 1. When the chain force reaches the maximum (f_{max}), the damage is: $D_{max} = 1 - \sigma/(N_0 f_{max})$, and the energy barrier becomes zero so that chain breaking occurs instantaneously as indicated by the cross markers. Similarly, Figure 3.5b shows that the opening displacement starts with an instantaneous value (with $D = 0$ and $\bar{f}(\bar{\delta}) = \bar{\sigma}$), then increases slowly over time, and accelerates to failure at the end, resembling the creep behavior. Increasing the traction increases the initial opening, expedites the damage evolution, and shortens the time to failure (t_f). Figure 3.6 shows that the time to failure ($\bar{t}_f = nt_f/t_0$) decreases rapidly with the increasing traction, resembling the creep rupture behavior. Remarkably, the normalized time to failure varies over a wide range (~ 20 decades), from essentially infinitely long time at very low traction to almost instantaneous failure ($t_f \sim t_0$) at a high traction close to the theoretical limit ($\sigma_{max} = N_0 f_{max}$). In addition, the effect of the bond energy and temperature can be predicted as well (Fig. 3.6). Notably, the temperature has a multitude of effects on the stress magnitude ($\sigma_0 = N_0 k_B T/r_0$), the time scale ($t_0 = \hbar/k_B T$), and the normalized bond energy ($\bar{\epsilon} = \epsilon_0/k_B T$). It can be seen

that the trend for the time to failure (Fig. 3.6) is very similar to that for the normalized energy barrier (Fig. 3.4b), as a result of the thermally activated chain rupture process.

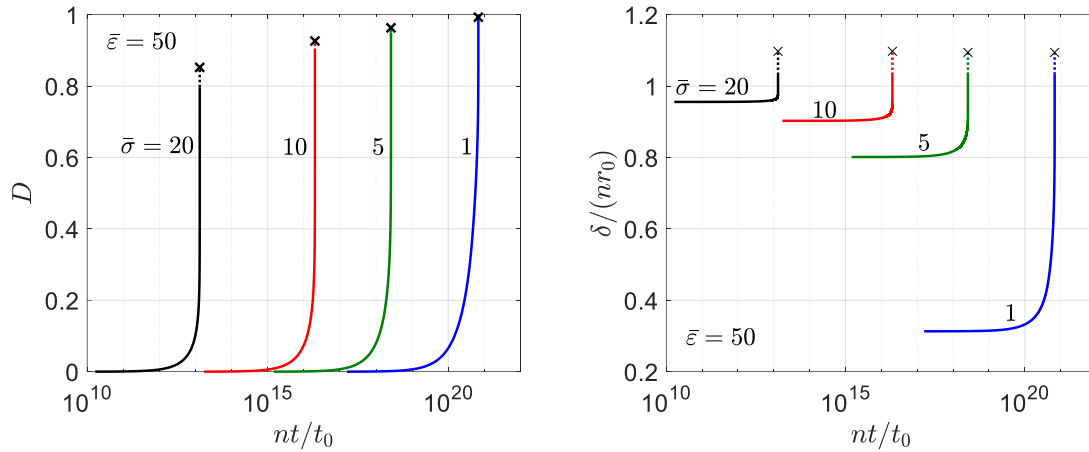


Figure 3.5 (a) Damage evolution and (b) normalized separation over time under constant tractions for $\bar{\varepsilon} = 50$.

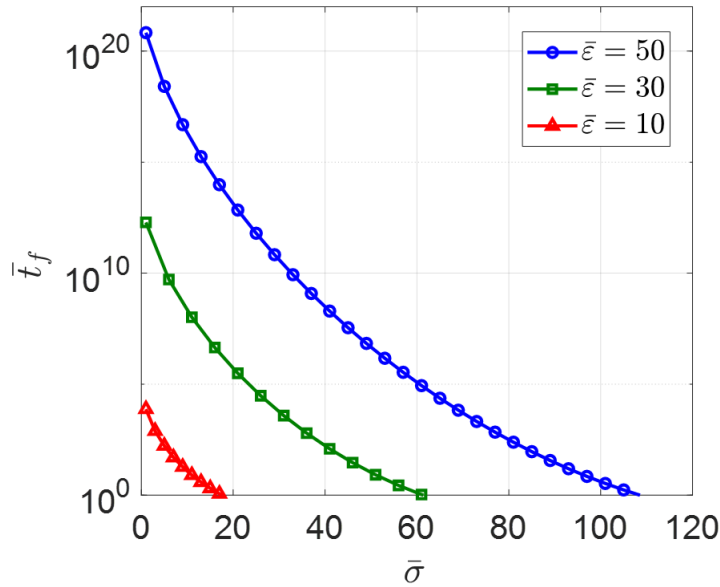


Figure 3.6 Predicted time to failure versus the normalized traction for different values of the bond energy ($\bar{\varepsilon} = 10, 30, 50$).

As another common loading condition, we consider a monotonic loading with a constant separation rate ($\dot{\delta}$), i.e., $\delta(t) = \dot{\delta}t$, and the normalized separation rate is: $\bar{\delta} = \dot{\delta}t_0/(n^2r_0)$. Here again, both the length scale (nr_0) and the time scale (t_0/n) depend on the chain length (n). In this case, we obtain rate-dependent damage evolution and traction-separation relations (Fig. 3.7). At a relatively low separation rate, the damage evolution is significant even at relatively small separation (Fig. 3.7a), which leads to a lower stiffness before the peak traction in the traction-separation relation (Fig. 3.7b). The initial stiffness can be predicted by the linear Gaussian chain model, with $\bar{\sigma} = 3\bar{\delta}$ for $D = 0$. Thus, the dimensional stiffness is: $K_0 = 3N_0k_B T/(nr_0^2)$, independent of the separation rate. With the continuous increase in damage, the traction peaks and becomes zero when the interface is fully damaged ($D = 1$). The softening part of the traction-separation relation is gradual at a low separation rate but becomes steeper as the separation rate increases. For a relatively high separation rate, the damage remains low until the separation is relatively large (Fig. 3.7c), which leads to a stiffening traction-separation relation (Fig. 3.7d), following the nonlinear Langevin mode with $\bar{\sigma} = \mathcal{L}^{-1}(\bar{\delta})$ (dashed lines). As the normalized separation ($\bar{\delta}$) or equivalently the chain stretch (λ) approaches 1, the damage increases sharply, leading to a peak traction followed by a steep softening in the traction-separation relation. Therefore, the rate-dependent damage evolution leads to the two types of traction-separation relations.

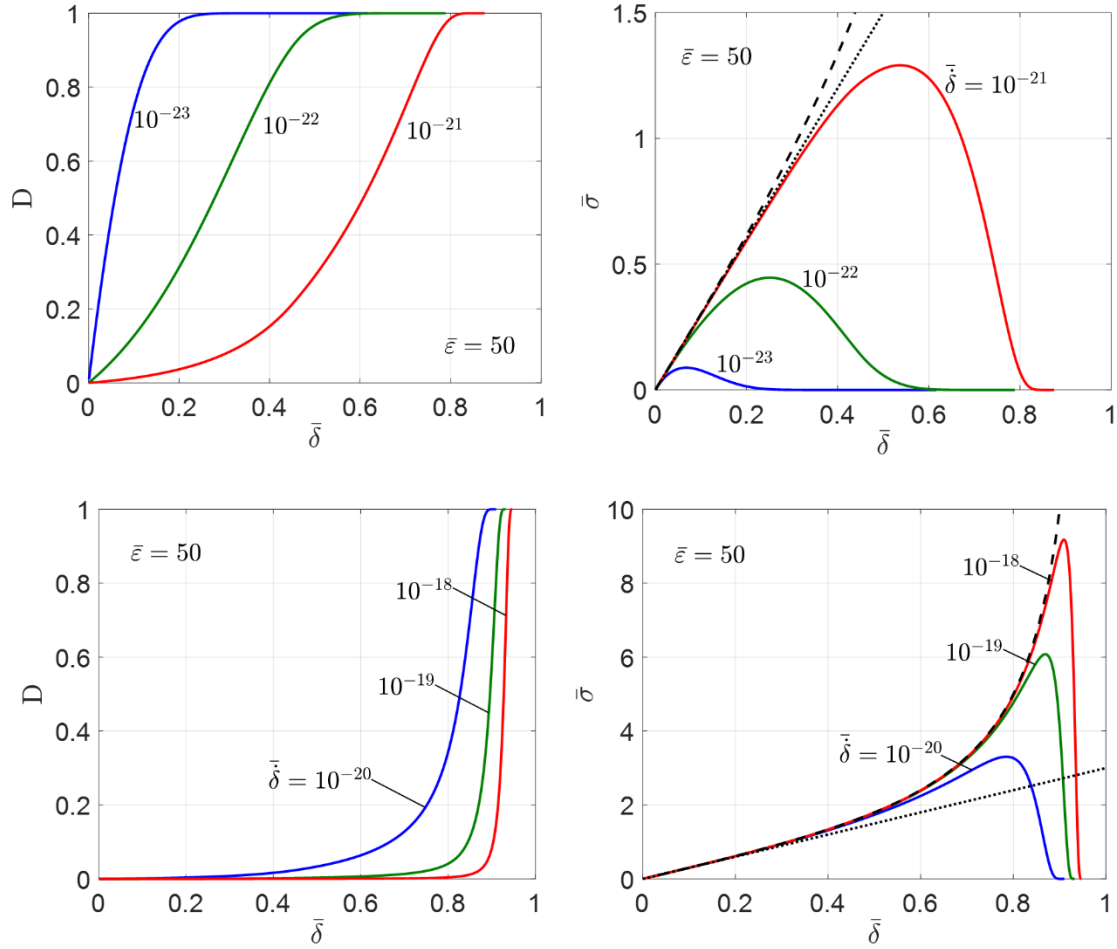


Figure 3.7 Predicted damage evolution and traction-separation relations under constant separation rates with $\bar{\epsilon} = 50$. (a-b) for relatively low separation rates, and (c-d) for relatively high separation rates. The dotted lines in (b) and (d) are for the linear Gaussian chain model with $\bar{\sigma} = 3\bar{\delta}$, and the dashed lines are for the nonlinear Langevin model with: $\bar{\sigma} = \mathcal{L}^{-1}(\bar{\delta})$, both independent of the separation rate with no damage ($D = 0$).

The key parameters for an interfacial traction-separation relation typically include: the initial stiffness (K_0), the peak traction or strength (σ_p), the maximum separation (δ_f), and the work of separation or toughness ($\Gamma = \int_0^{\delta_f} \sigma d\delta$, normalized by $\Gamma_0 = nr_0\sigma_0 = nN_0k_B T$). By the present model, except for the initial stiffness, the other three parameters are rate dependent, increasing as the separation rate increases. As shown in Fig. 3.8, for

each value of the normalized bond energy, both the strength and the toughness of the interface depend on the normalized separation rate, with two different regimes. For relatively low separation rates, both the strength and the toughness are low but depend sensitively on the separation rate, with orders of magnitude differences. In contrast, for relatively high separation rates, the rate dependence is less significant, typically within one order of magnitude. At very high separation rates ($\bar{\delta} \rightarrow 1$), the strength approaches a theoretical limit set by the bond model as $\sigma_{max} = N_0 f_{max}$ and $\bar{\sigma}_p \rightarrow \bar{f}_{max}$, and the toughness approaches a corresponding limit (up to the maximum bond force). We note that the predicted toughness by the present model is always less than that by the Lake-Thomas model [112] for elastomers. The latter assumes all the bonds in the chains reach the rupture point simultaneously so that the toughness is simply $\Gamma_{LT} = nN_0\varepsilon_0$ and $\bar{\Gamma}_{LT} = \bar{\varepsilon}$ after normalization. Considering the thermally activated chain breaking mechanism in the present model, the energy barrier for bond rupture drops to zero as the bond force reaches the maximum (f_{max}), at which point the chain breaks instantaneously. Therefore, the energy to break each bond equals the work done to stretch the bond up to the maximum force and does not include the work associated with the softening part of bond stretch (unstable); as a result, the theoretical limit for the bond rupture energy is only a fraction of the bond energy at the equilibrium state. Moreover, as a thermally activated process, the bonds and the chains could break before the bond force reaches the maximum, thus lowering the toughness further as the separation rate decreases.

According to Fig. 3.8, both the strength and the toughness decreases as the bond energy decreases. The effect of temperature is again more complicated as it affects the normalized bond energy as well as the normalized separation rate, the normalized strength and toughness.

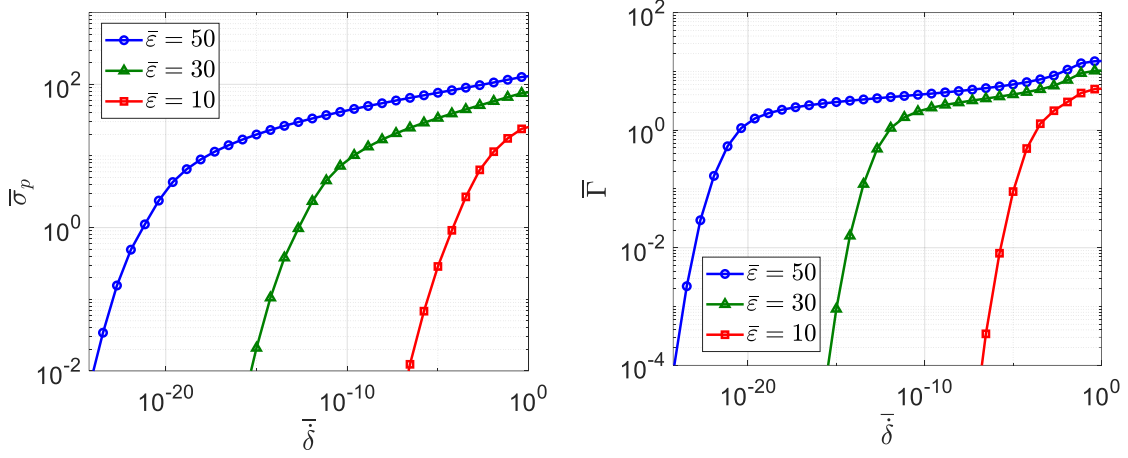


Figure 3.8 (a) Normalized strength and (b) toughness versus the normalized separation rate at different values of the normalized bond energy.

3.4 Effect of statistically distributed chain lengths

The previous section considers the thermally activated chain breaking by assuming an identical chain length (the number of bonds per chain) for all the chains at the interface level. More realistically, however, the chains may not have the same length. In this section, we assume a statistical distribution of the chain lengths as part of the multiscale interface model. We describe the initial statistical distribution using a continuous chain density function, $\rho_0(n)$, which gives the number of chains per unit area with the chain length between n and $n + dn$. Then, the total number of chains per unit area is:

$$N_0 = \int \rho_0(n) dn, \quad (3.21)$$

where n may range from 1 to infinity or any specific limits ($n > 0$). Subject to a traction or separation, some of the chains break, and the number density of the intact chains evolves over time, i.e., $\rho(n) = (1 - D_n)\rho_0(n)$, where D_n is the damage parameter for the chains of n bonds and follows the same evolution equation as in (3.19), namely

$$\frac{dD_n}{dt} = \frac{n}{t_0} (1 - D_n) \exp\left(-\frac{E_b}{k_B T}\right). \quad (3.22)$$

Assuming same separation (δ) for all the intact chains, the chain stretch ($\lambda_n = \delta/(nr_0)$) and the chain force (f_n) depend on the chain length. The traction at the interface is then

$$\sigma = \int (1 - D_n) f_n \rho_0(n) dn. \quad (3.23)$$

By Eqs. (3.22) and (3.23), along with Eq. (3.10) for the force-stretch relation of a chain and Eq. (3.13) for the energy barrier, the effect of statistically distributed chain lengths is accounted for in the interface model.

To be specific, we assume a normal distribution of the chain lengths as follows:

$$\rho_0(n) = \frac{N_0}{\sqrt{2\pi}\chi} \exp\left(-\frac{1}{2}\left(\frac{n-n_0}{\chi}\right)^2\right). \quad (3.24)$$

The chain density function is characterized by three parameters: the total chain density N_0 , the average chain length n_0 , and the standard deviation χ . Here, we assume that $n_0 - 3\chi > 1$ so that Eq. (3.21) holds for the range of the chain lengths ($n > 1$).

As noted in Section 3.3, both the length scale and the time scale depend on the chain length. With statistically distributed chain lengths, the length and time scales are no longer uniquely defined for all the chains. Nevertheless, we may use the average chain length (n_0) to define a length scale ($n_0 r_0$) and a time scale (t_0/n_0). Then, following similar normalization as: $\bar{\sigma} = \sigma/\sigma_0$ (with $\sigma_0 = N_0 k_B T/r_0$), $\bar{\delta} = \delta/(n_0 r_0)$, and $\bar{t} = n_0 t/t_0$, the resulting equations have only two dimensionless parameters: $\bar{\varepsilon}$ and $\bar{\chi} = \chi/n_0$ (relative deviation), where $\bar{\chi} = 0$ for the case of a constant chain length. If the interface is subject to a constant traction, the normalized creep-like behavior would depend on $\bar{\sigma}$, $\bar{\varepsilon}$, and $\bar{\chi}$, similar to Fig. 3.5 (where $\bar{\chi} = 0$). If the interface is subject to a constant separation rate, the normalized traction-separation relation would depend on the

normalized separation rate, $\bar{\delta} = \dot{\delta}t_0/(n_0^2r_0)$, in addition to $\bar{\varepsilon}$ and $\bar{\chi}$, as shown in Fig. 3.9 for two different separation rates.

Figure 3.9 (a-b) shows that the normalized traction-separation relation depends on the relative deviation $\bar{\chi}$. Compared to the case of a constant chain length ($\bar{\chi} = 0$), the initial interfacial stiffness increases slightly, the strength decreases, and the range of interactions increases, as $\bar{\chi}$ increases. In particular, the strength and range change more significantly under a relatively high separation rate. Figure 3.9 (c-d) shows the evolving chain length distributions as the interfacial separation increases for $\bar{\chi} = 0.1$. While the initial distribution is the same, the evolution depends on the separation rate. At a relatively low separation rate, the chain length distribution appears to retain the shape of a normal distribution, but the peak shifts slowly to the right, indicating that the shorter chains break faster. In contrast, at a high separation rate, the chain length distribution becomes highly distorted, with the shorter chains breaking much faster than the longer chains. The fast breaking of the short chains leads to a lower strength of the interface, whereas the presence of longer chains extends the range of interactions.

Since the rate of chain rupture varies with the chain length, the damage parameters evolve at different rates for different chain lengths. At the interface level, we define an overall damage parameter as: $D = 1 - N/N_0$, where N is the number of intact chains (regardless of the chain length) and can be calculated as

$$N = \int (1 - D_n)\rho_0(n)dn. \quad (3.25)$$

As shown in Fig. 3.9 (e-f), the evolution of the interfacial damage parameter depends on the relative deviation of the chain lengths as well as the separation rate. The interfacial damage grows faster at relatively low separations, due to breaking of the short chains. Then, the damage evolution becomes slower at large separations, due to the presence of

long chains. The effect is more significant for the higher separation rate, where the damage grows abruptly for the case of a constant chain length but becomes more gradual with the statistically distributed chain lengths. Therefore, by the present model, the chain length distribution has a profound influence on the damage evolution and the traction-separation relation of the interface.

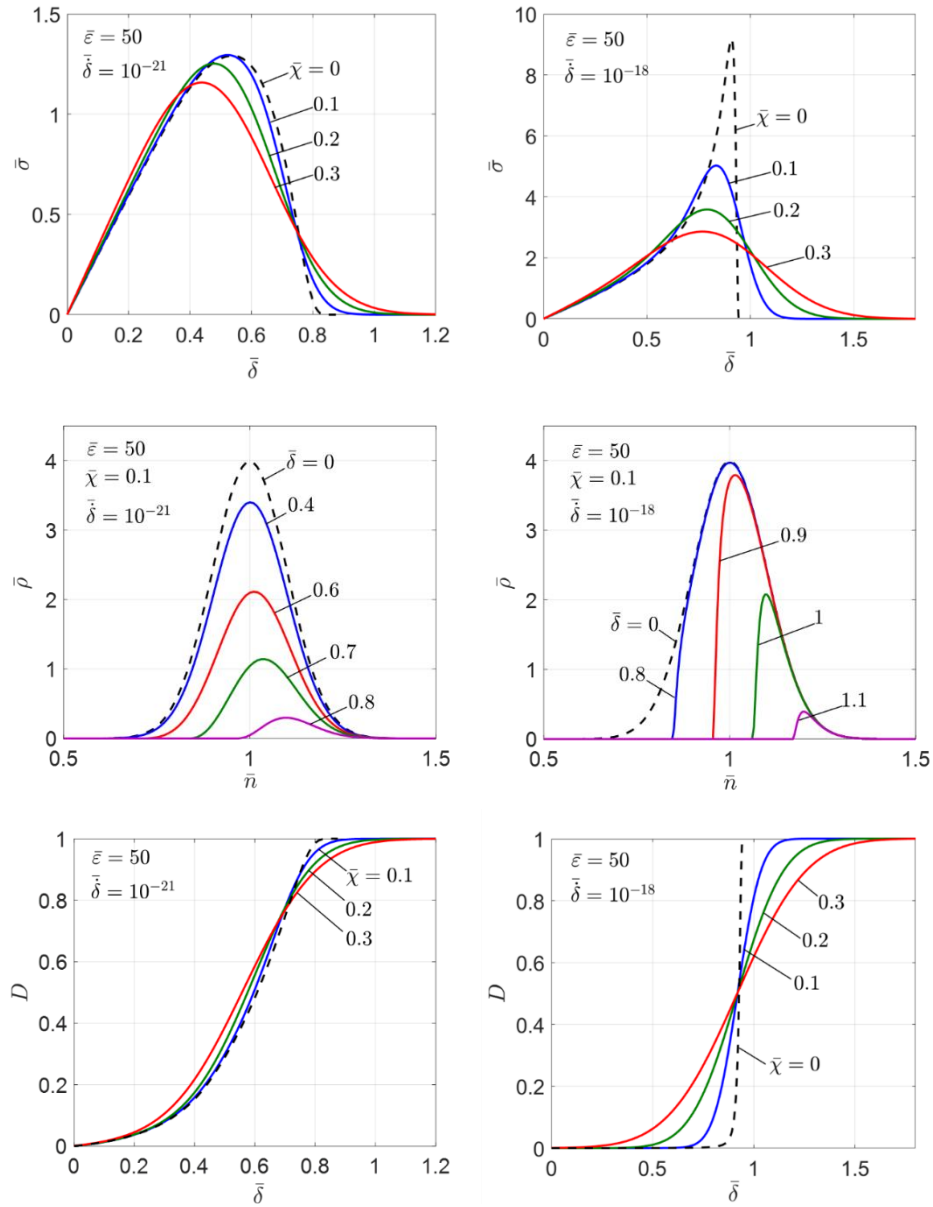


Figure 3.9 Normalized traction-separation relations (a-b), chain length distributions (c-d), and damage evolution (e-f) under a constant separation rate. (a,c,e) for a relatively low separation rate, while (b,d,f) for a high separation rate.

Three key parameters of the interfacial traction-separation relation can be predicted by the present model. First, the initial stiffness of the interface is independent of the separation rate but depends on the chain length distribution as

$$K_0 = \frac{3k_B T}{r_0^2} \int \frac{\rho_0(n)}{n} dn = \frac{3N_0 k_B T}{n_0 r_0^2} \bar{K}_0(\bar{\chi}), \quad (3.26)$$

where

$$\bar{K}_0(\bar{\chi}) = \frac{1}{\sqrt{2\pi\bar{\chi}}} \int \frac{1}{\bar{n}} \exp\left(-\frac{1}{2}\left(\frac{\bar{n}-1}{\bar{\chi}}\right)^2\right) d\bar{n}. \quad (3.27)$$

As shown in Fig. 3.10a, $\bar{K}_0 = 1$ for the case of a constant chain length ($\bar{\chi} = 0$) but increases slightly with increasing $\bar{\chi}$. Next, the peak traction as the interfacial strength is shown in Fig. 3.10b as a function of $\bar{\chi}$ at different separation rates. By integrating the traction-separation relation, we obtain the interfacial toughness ($\Gamma = \int_0^{\delta_f} \sigma d\delta$), as shown in Fig. 3.10c. Interestingly, while the interfacial strength may change significantly with the chain length distribution, especially at high separation rates, the interfacial toughness is less sensitive to the chain length distribution. Overall, both the strength and toughness decreases with increasing relative deviation, but the range of interactions also increases to partly compensate the decreasing strength so that the toughness does not change as much. This prediction appears to be consistent with experiments, where measurements of the interfacial toughness (or adhesion energy) are often commensurate among different methods or specimens, but the traction-separation relations could vary, which may be partly due to the statistical distributions of the chain lengths varying from specimen to specimen.

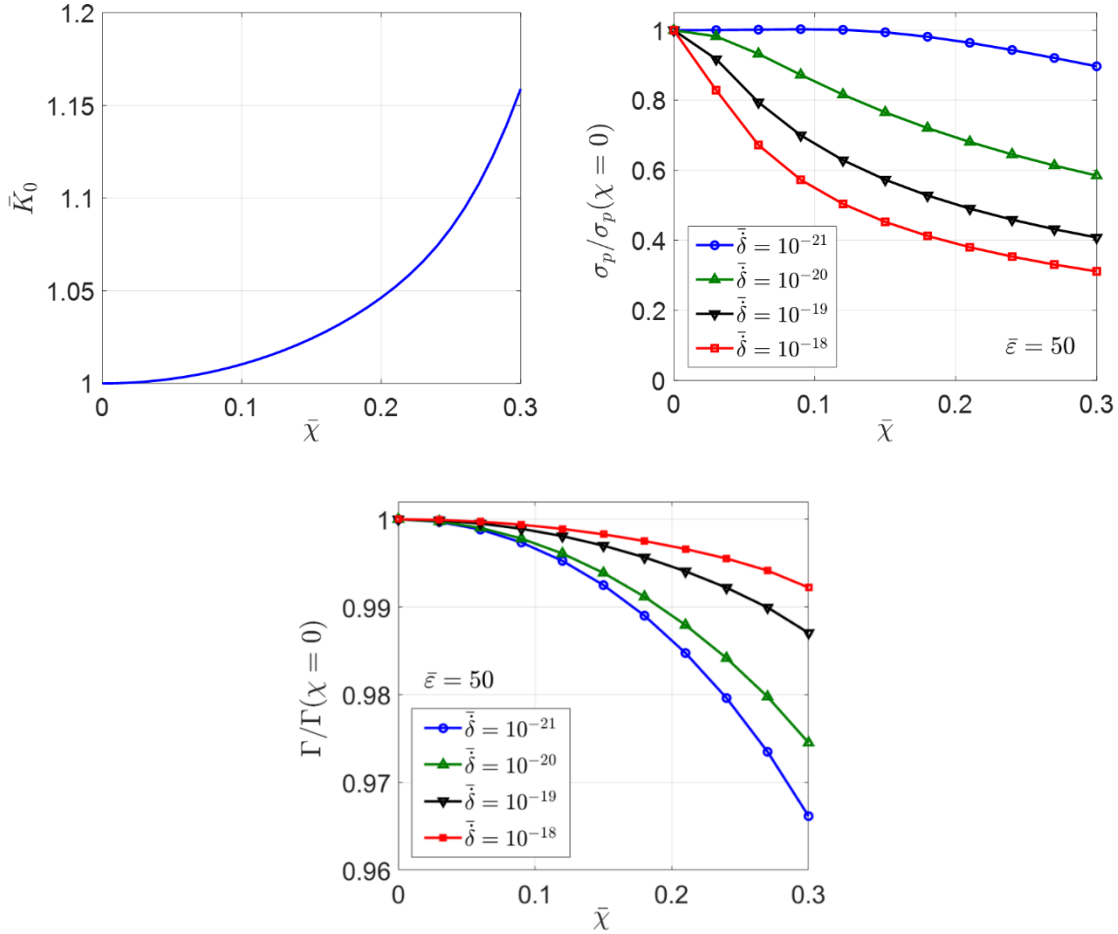


Figure 3.10 Effects of the relative deviation in statistically distributed chain lengths on the predicted interfacial properties: (a) the initial stiffness, (b) the strength, and (c) the toughness, all normalized with respect to the corresponding properties for a constant chain length ($\bar{\chi} = 0$).

3.5 Specimen level: Mode-I fracture of a silicon/epoxy interface

In this section, the multiscale interface model formulated in the previous sections (Sections 3.1-3.4) is compared to the rate-dependent fracture of a silicon/epoxy interface in mode-I experiments. For numerical simulations by the finite element method at the specimen level, the interface model is implemented as a user-defined interface (UINTER) subroutine in ABAQUS (see Appendices C and D), which is then used to define the surface

interactions between silicon and epoxy in the finite element analysis of the DCB experiments.

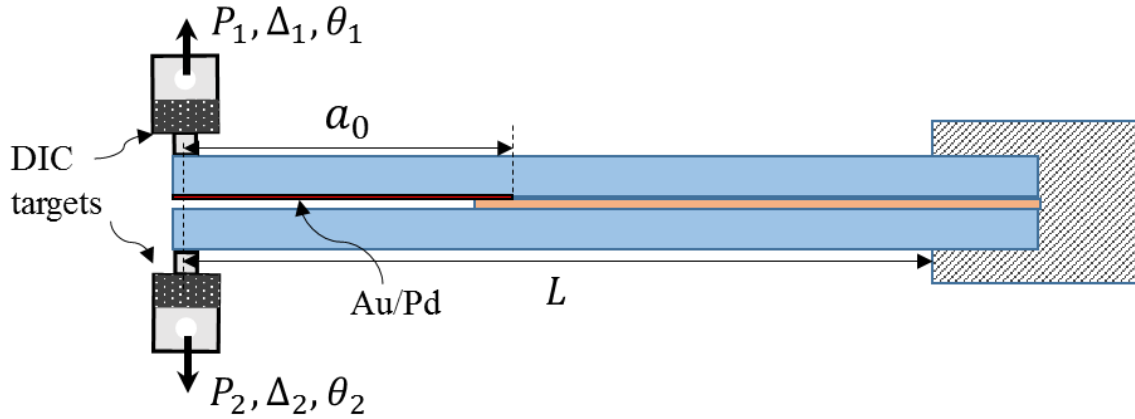


Figure 3.11 Schematic of a double cantilever beam (DCB) specimen, direct measurements including forces, displacements and rotations at the loading end.

The specimen (Fig. 3.11) consists of two silicon beams as adherends and a layer of epoxy (EP 30, MasterBond Inc.) as the adhesive. Each silicon beam has the dimensions: $L = 38$ mm (length), $b = 5$ mm (width) and $h = 1$ mm (thickness). The epoxy layer has a thickness of about $40 \mu\text{m}$ and a length of about 26 mm, leaving an initial crack of length $a_0 \approx 12$ mm. To help initiating an interfacial crack growth between silicon and epoxy, we coated a thin layer of Au/Pd (~ 15 nm thick) on part of the surface of the upper silicon beam, noting that the adhesion is relatively weak between the Au/Pd layer and the epoxy. The length of the Au/Pd coating was measured as the initial crack length (a_0) and is listed in Table 3.1 for all specimens. More details about the specimen preparation can be found in a previous work [139]. In the subsequent analysis, both silicon and epoxy are treated as linearly elastic with ($E = 130$ GPa, $\nu = 0.22$) for silicon and ($E_e = 2.4$ GPa, $\nu = 0.4$) for the epoxy, which can be justified by comparing the yield strength of the epoxy (~ 30 MPa) and the strength of the interface (< 12 MPa).

The experiments were conducted with a dual-actuator loading device (see more details in Chapter 4). The direct measurements include the opening displacements (Δ_i), forces (P_i), and rotation angles (θ_i), all at the opening end of the specimen, where $i = 1, 2$ denotes the upper and lower beams, respectively. In particular, the rotation angles were measured by digital image correlation (DIC). While the dual-actuator loading was designed for fracture experiments with arbitrary mode mix, symmetric loading conditions (i.e., $\Delta_1 = -\Delta_2$, $P_1 = -P_2$, $\theta_1 = -\theta_2$) were maintained for all specimens in this part of the study in order to ensure predominantly mode-I fracture of the interface. The end opening ($\Delta = \Delta_1 - \Delta_2 = 2\Delta_1$) was controlled with a constant rate ($\dot{\Delta}$) for each specimen, as listed in Table 3.1.

Table 3.1 Parameters used in the model at different separation rates

$\dot{\Delta}$ (mm/s)	a_0 (mm)	δ^* ($\mu\text{m/s}$)	J_{ss} (J/m^2)	K_0 ($\times 10^{12} \text{ N/m}^3$)	σ_p (MPa)
0.625	12.13	11.46	11.5	8.8	11.6
0.125	12.10	2.18	8.8	9.8	9.2
0.025	12.34	0.44	6.2	7.8	6.1
0.005	12.19	0.083	2.1	10.2	3.0
0.001	12.10	0.018	1.2	9.4	1.8

Following the method proposed by Wu et al. [56], the crack tip opening displacement (CTOD, δ^*) and the normal component of the J-integral (energy release rate) can be obtained for a symmetric DCB specimen as

$$\delta^* = 2\Delta_1 + \frac{P_1 a_0^3}{3EI} - 2a_0\theta_1 \quad (3.28)$$

$$J_1 = 2P_1\theta_1/b \quad (3.29)$$

where $\bar{E} = E/(1 - \nu^2)$ is the plane-strain modulus of silicon and $I = bh^3/12$. Then, the normal traction at the initial crack tip can be determined approximately as

$$\sigma^* = \partial J_1 / \partial \delta^* \quad (3.30)$$

We note that Eqs. (3.28)-(3.30) were derived from a linear elastic beam analysis with the two silicon beams interacting via a traction-separation relation that is unknown *a priori* [56].

By measuring a_0 , Δ_1 , P_1 , and θ_1 , we obtained from Eqs. (3.28)-(3.30) the CTOD (δ^*), the J-integral (J_1), and then the traction-separation relation, $\sigma^*(\delta^*)$, at the initial crack tip. Figure 3.12 (a-d) shows the force-displacement ($P_1 - \Delta_1$) curves, δ^* versus Δ_1 , J_1 versus δ^* , and the traction-separation relations, respectively. For each specimen, both the force and the CTOD first increased linearly with increasing Δ_1 , and then the force decreased after a peak and the CTOD increased at a much faster rate, where initiation of the crack growth was signified by the peak force. Thus, the local separation rate at the initial crack tip ($\dot{\delta}^*$) was proportional to the applied separation rate ($\dot{\Delta}$) at the loading point before the crack growth was initiated, after which the local separation rate increased and was no longer a constant. The J-integral in Fig. 3.12c first increased and then approached a plateau value as the steady-state energy release rate (J_{SS}), which is rate dependent. The extracted traction-separation relations in Fig. 3.12d are also rate dependent, typically with an initial stiffness (K_0) for the linear portion and a peak traction (σ_p) followed by a softening portion towards zero traction. The values of J_{SS} , K_0 and σ_p thus obtained for the five specimens are listed in Table 3.1 along with the local separation rates $\dot{\delta}^*$ (Fig. 3.12b, for the linear part only). Notably, both J_{SS} and σ_p increased with increasing separation rates, whereas K_0 did not exhibit a clear rate dependence. Similar results were reported in Chapter 2.

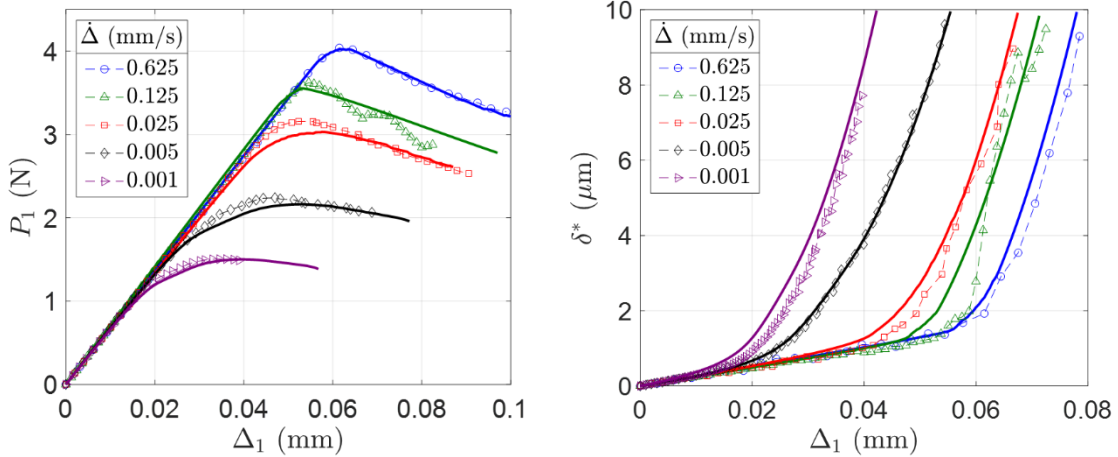
The measured load-displacement curves are typically linear before crack growth (Fig. 3.12a), based on which we can estimate the initial stiffness (K_0) of the interface using the beam-on-elastic-foundation [55] as:

$$P_1 = \frac{3\bar{E}I\Delta_1}{a^3} \left(1 + \frac{3}{\lambda a} + \frac{3}{(\lambda a)^2} + \frac{3}{2(\lambda a)^3} \right)^{-1} \quad (3.31)$$

where $a = a_0$ and $\lambda = (6K_0/(\bar{E}h^3))^{1/4}$. With the initial crack length (a_0) and the measured slope of the load-displacement curves, the values of K_0 can be determined, which turned out to be nearly identical to those obtained from the initial slope in the traction-separation relations (Fig. 3.12d). Furthermore, by the beam-on-elastic-foundation model, the local separation rate at the initial crack tip can be estimated as [139]

$$\dot{\delta}^* = \dot{\Delta} \left(\frac{2}{3}(1 + \lambda a)^2 + \frac{1}{3(1 + \lambda a)} \right)^{-1}, \quad (3.32)$$

which is consistent with the initial separation rate obtained by Eq. (6.1) or the linear part of Fig. 3.12b. We note that, unlike Eqs. (3.28)-(3.30), the beam-on-elastic-foundation model assumes that the two silicon beams interact via a linear traction-separation relation [55], and is thus limited to the linear portion of the interactions (before the initiation of crack growth).



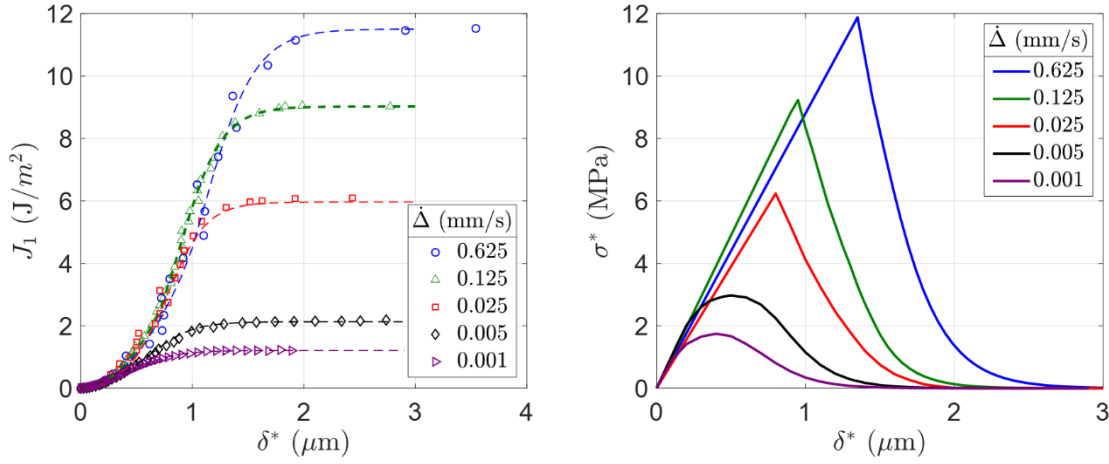


Figure 3.12 (a) Force-displacement curves under different separation rates (measurements in symbols and simulations in solid lines); (b) CTOD versus the end displacement (symbols by Eq. (6.1) and solid lines by simulations); (c) J-integral versus CTOD (data fitted by functions plotted as dashed lines); (d) Extracted crack tip traction-separation relations.

Next, we determine the parameters in the multiscale interface model. There are a total of six parameters: the bond energy (ε_0), bond length (r_0), chain density (N_0), average chain length (n_0), statistical deviation of chain lengths (χ), and the microscopic time scale (t_0). Among them, the time scale, as mentioned in Section 3.4, is set to be: $t_0 = \hbar/k_B T \sim 10^{-13}$ s for all specimens; here we take $k_B T = 0.0257$ eV for room temperature ($\sim 25^\circ\text{C}$). On the other hand, considering that the statistical distribution of chain lengths may vary from specimen to specimen, we allow different chain length deviations (χ) to be determined after the other parameters. Thus, we start by assuming $\chi = 0$ to determine the other four parameters: bond length (r_0), average chain length (n_0), chain density (N_0), and the bond energy (ε_0).

Recall that the peak stress and the toughness predicted by the present model (Fig. 3.8) are normalized by $\sigma_0 = N_0 k_B T / r_0$ and $\Gamma_0 = n_0 N_0 k_B T$, respectively. It is found that the two normalized quantities are closely correlated as shown in Fig. 3.13a, where the

results from different combinations of the normalized separation rate and bond energy nearly collapse onto one curve. This correlation enables us to determine the two quantities from the experiments as follows. A combination of the two normalized quantities can be related directly to the three dimensional quantities, namely

$$\bar{\Gamma}/\bar{\sigma}_p^2 = K_0\Gamma/(3\sigma_p^2) \quad (3.33)$$

where $K_0 = 3N_0k_B T/(n_0r_0^2)$. With $\Gamma = J_{ss}$ and the values listed in Table 3.1 as the dimensional quantities extracted from the experiments, we obtain $\bar{\Gamma}/\bar{\sigma}_p^2$ for each specimen. For example, with $J_{ss} = 11.5 \text{ J/m}^2$, $K_0 = 8.8 \times 10^{12} \text{ N/m}^3$, and $\sigma_p = 11.6 \text{ MPa}$ for the specimen with the highest separation rate ($\dot{\Delta} = 0.625 \text{ mm/s}$), we obtain $\bar{\Gamma}/\bar{\sigma}_p^2 = 0.25$ by Eq. (3.33). For comparison with the model predictions in Fig. 3.13a, we draw a straight line in the log-log plot ($\bar{\Gamma}/\bar{\sigma}_p^2 = 0.25$), which intersects with the predicted curve at one point with particular values of $\bar{\Gamma}$ and $\bar{\sigma}_p$, $\bar{\Gamma} = 0.94$ and $\bar{\sigma}_p = 1.94$ for this specimen. Then, with $\Gamma = J_{ss} = 11.5 \text{ J/m}^2$ and $\sigma_p = 11.6 \text{ MPa}$, we obtain that $\Gamma_0 = 12.23 \text{ J/m}^2$ and $\sigma_0 = 5.98 \text{ MPa}$. With these values, we obtain $n_0r_0 = \Gamma_0/\sigma_0 = 2.04 \text{ }\mu\text{m}$ and $N_0/r_0 = \sigma_0/k_B T = 1.47 \times 10^{23} \text{ m}^{-3}$. To continue without additional measurements, we assume a constant bond length for all specimens in this work as: $r_0 = 0.5 \text{ nm}$. Apparently, it is challenging (if not impossible) to determine this microscopic quantity solely based on macroscopic measurements. Nevertheless, with the constant bond length, we obtain $n_0 = 4007$ and $N_0 = 7.37 \times 10^{17} \text{ m}^{-2}$ for this specimen ($\dot{\Delta} = 0.625 \text{ mm/s}$). Hence, the local separation rate of $11.46 \text{ }\mu\text{m/s}$ at the initial crack tip corresponds to a normalized separation rate, $\bar{\delta} = \dot{\delta}t_0/(n_0^2r_0) = 1.43 \times 10^{-16}$, which is combined with the normalized toughness ($\bar{\Gamma} = 0.94$) to determine the bond energy (Fig. 3.8b), yielding a value of $\varepsilon_0 \sim 1.0 \text{ eV}$ ($\bar{\varepsilon} = 38.9$). Finally, to determine the statistical deviation of chain lengths (χ), we note that a small relative deviation ($\chi/n_0 < 0.1$) could be used to improve

the agreement between the numerical simulations and the experiments (Fig. 3.13b) without significantly altering the key properties of the interface (Fig. 3.10). In particular, Fig. 3.13b shows that the peak force in the simulated load-displacement curve decreases with increasing deviation and the transition from linear increasing to decreasing becomes more gradual. Following the same procedure, the model parameters are obtained for the five specimens as listed in Table 3.2.

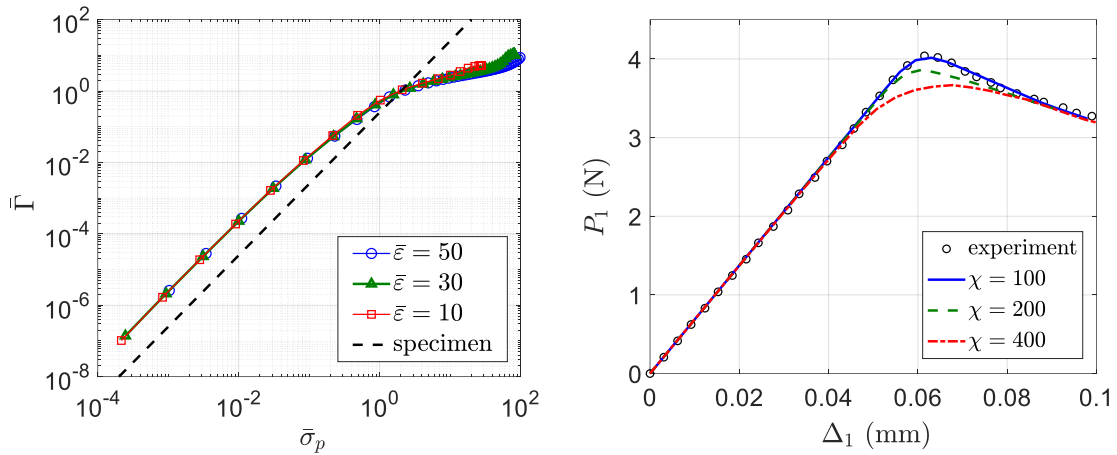


Figure 3.13 (a) Correlation between the normalized toughness and strength predicted by the model, intersecting the dashed line with $\bar{\Gamma}/\bar{\sigma}_p^2 = 0.25$ for one specimen ($\dot{\Delta} = 0.625$ mm/s); (b) Comparison of the force-displacement curves from experiment ($\dot{\Delta} = 0.625$ mm/s) and numerical simulations with different deviations of the chain lengths.

The model parameters for the five specimens provide a consistent picture of the silicon/epoxy interface, with an average chain length of $n_0 = 4154 \pm 238$, an areal chain density of $N_0 = 7.82 \pm 1.01$ ($\times 10^{17}$ m $^{-2}$), and a bond energy of $\epsilon_0 = 1.04 \pm 0.02$ eV. The statistical deviations of the chain lengths are relatively small ($\chi/n_0 < 0.1$), but could vary considerably from specimen to specimen. The areal chain density appears to be reasonable with an area of around 1 nm 2 per chain. The value of the bond energy is also quite

reasonable, although it is lower than the values associated with Si-C and Si-H bonds (~4.35 and 2.98 eV).

With the model parameters in Table II, we simulate the DCB experiments by the finite element method using ABAQUS. The finite element model consists of two silicon beams and an epoxy layer as shown schematically in Fig. 11, where the interactions between the epoxy and the upper silicon beam are described by the user-defined interface (UINTER) subroutine following the implementation of the rate-dependent interface model (see Appendix C for details). The numerical results are compared to the experiments in Fig. 3.12 (a and b) in terms of the force-displacement curves and the CTOD, respectively. Overall, the agreement is satisfactory for all five specimens. It is noted that the traction-separation relation in the present model depends on the local separation rate, which generally is not a constant for the DCB specimens (see Fig. 3.12b) and may vary along the interface. This is in contrast with the common assumption that the same traction-separation relation can be used to describe the fracture processes of the interface. In fact, such an assumption was used to derive Eq. (3.29) for the J-integral and Eq. (3.30) [56]. However, by the rate-dependent cohesive zone model, Eq. (3.30) is generally incorrect, and the J-integral must be calculated with a contour enclosing the interface from the initial crack tip to the clamped end, namely

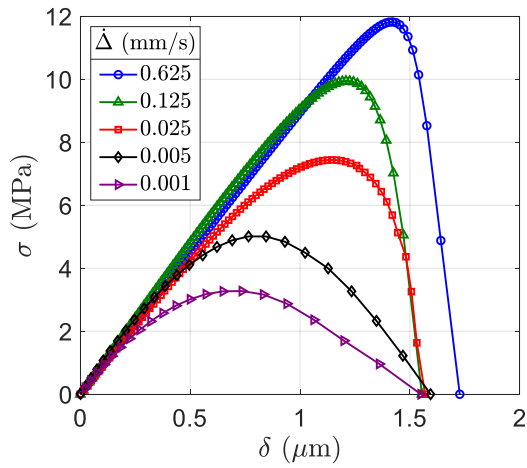
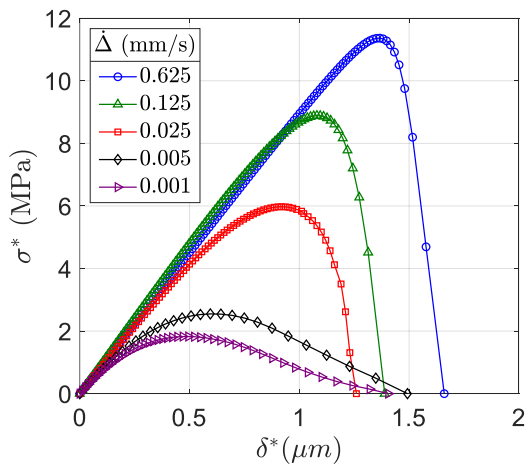
$$J_1 = \int_0^{L-a} \sigma \frac{\partial \delta}{\partial x} dx \quad (3.34)$$

where $x = 0$ at the initial crack tip (Fig. 3.11). By Eq. (3.34), as the crack grows, the J-integral increases and reaches a steady state value (Fig. 3.14c), a typical behavior for a fracture resistance curve (R-curve). Evidently, the J-integral for crack initiation corresponds to the traction-separation relation at the initial crack tip (Fig. 3.14a), and the

steady-state J-integral corresponds to the traction-separation relation (Fig. 3.14b) at a location slightly ahead of the initial crack tip.

Table 3.2 Model parameters determined and used in numerical simulations

$\dot{\Delta}$ (mm/s)	$\dot{\delta}^*$ ($\mu\text{m/s}$)	t_0 (s)	r_0 (nm)	n_0	N_0 ($\times 10^{17}$ m ⁻²)	ε_0 (eV)	χ
0.625	11.46	10 ⁻¹³	0.5	4008	7.37	1.00	100
0.125	2.18			3877	7.41	1.03	50
0.025	0.44			4065	6.41	1.06	50
0.005	0.083			4262	9.29	1.05	400
0.001	0.018			4560	8.63	1.05	450
Average						4154±238	7.82±1.01



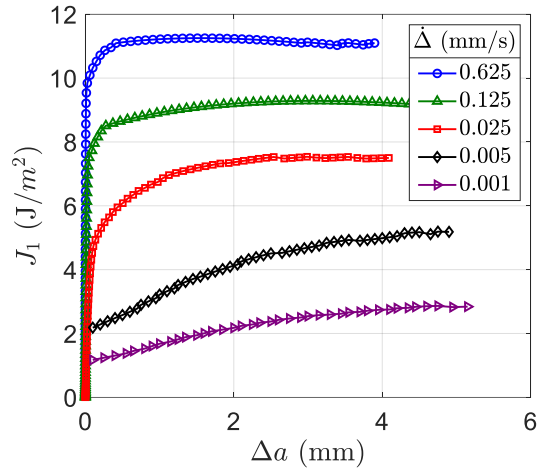


Figure 3.14 (a) Traction-separation relations at the initial crack tip; (b) Steady-state traction-separation relations; (c) Resistance curve obtained by Eq. (3.34).

Using the average values of the extracted model parameters (Table 3.2), we can predict the rate-dependent properties of the silicon/epoxy interface, as shown in Fig. 3.15. Here, the toughness and strength are plotted as functions of the local separation rate (assumed to be a constant). The statistical deviation of the chain lengths is taken to be zero or 450 as the lower/upper bounds among the specimens. Consistent with Fig. 3.10, it is found that such a chain length deviation has a minimal effect on the interfacial toughness over a wide range of the separation rate (Fig. 3.15a). The effect on the interfacial strength is appreciable for relatively high separation rates (Fig. 3.15b), with a lower strength due to the statistical deviation of chain lengths. The predicted toughness and strength are compared to those extracted directly from the DCB experiments including those in Chapter 2. While the agreement appears to be reasonable, it is noted that the local separation rate was not a constant in the DCB experiments except for the initially linear response. Moreover, in Chapter 2, these properties were extracted based on the beam on elastic foundation model assuming a linear traction-separation relation for the interface. In contrast, the properties in Table 3.1 were extracted without assuming a specific traction-

separation relation but assuming that the relation is the same everywhere along the interface. Neither is exactly the case by the rate-dependent cohesive zone model, but may be considered as reasonable approximations for a direct method to extract the traction-separation relations from the experiments. The rate-dependent cohesive zone model, once calibrated by the experiments with the model parameters (Table 3.2), can be used to predict the fracture of the interface under various conditions including monotonic and cyclic loadings, where the local separation rate may vary in time and location.

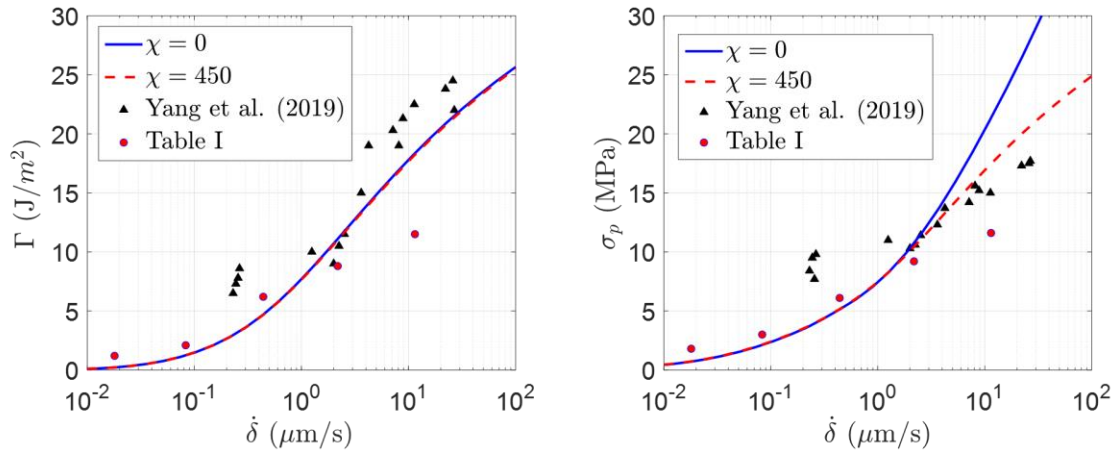


Figure 3.15 Rate-dependent fracture toughness (a) and strength (b) of the silicon/epoxy interface predicted by the model, in comparison with the values extracted directly from the DCB experiments (Table 3.1) and from the previous work [139].

3.6 Summary

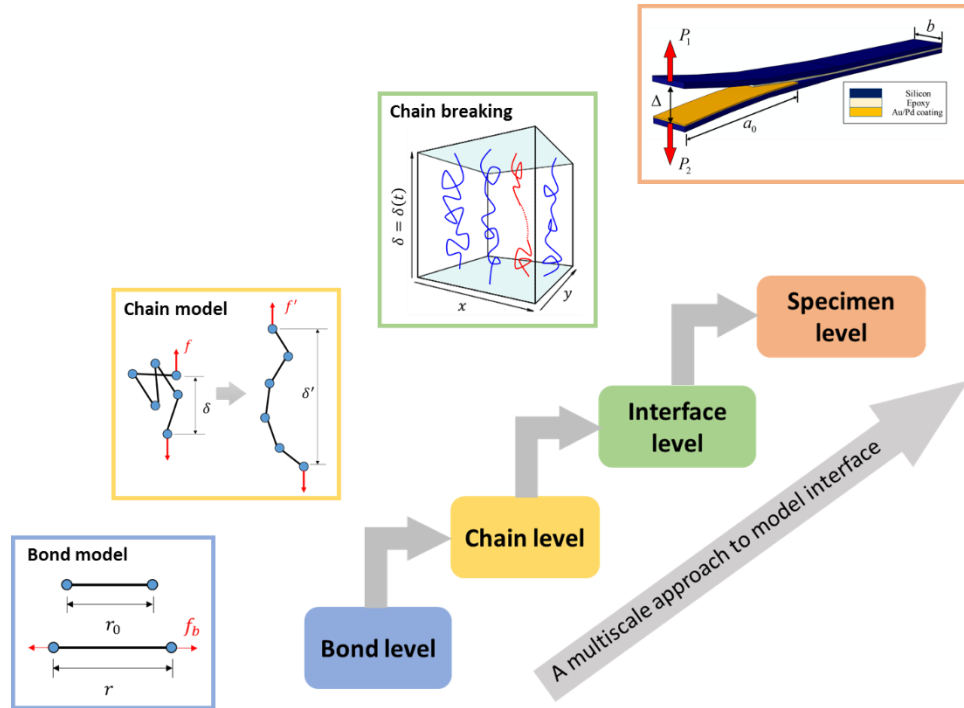


Figure 3.16 Schematic of the multiscale rate-dependent cohesive zone model.

This chapter presents a multiscale mechanism-based cohesive zone model for rate-dependent fracture of interfaces (Fig. 3.16). The model relates the interfacial properties (stiffness, strength and toughness) to the molecular structures in terms of the bond energy, bond length, chain length, areal chain density, and statistical deviation of chain lengths. While the Lennard-Jones potential energy is adopted to describe the individual bonds, other bond models can be used as part of the multiscale model. To account for the configurational entropy of long molecular chains, a modified freely jointed chain model is proposed, which allows bond stretching in a freely jointed chain. Again, other chain models may also be employed as part of the multiscale interface model. Next, the chain breaking process is modeled as a result of thermally activated bond rupture, with a microscopic time scale at the root of the time and rate-dependent behaviors. With a large number of identical chains

at the interface level, the survival probability of the chains is related to the damage parameter, and the traction-separation relation can be predicted under various conditions. For a constant separation rate in particular, both the strength and toughness increase with the increasing rate, while the stiffness is rate independent. Furthermore, the statistical distributions of the chain lengths at the interface are considered by assuming a normal distribution. The relative deviation of the chain length could decrease the strength but increase the range of interactions, with a minimal effect on the toughness.

To compare with experiments, the rate-dependent cohesive zone model is implemented as a user-defined interface (UINTER) in ABAQUS and then used to simulate the rate-dependent fracture of a silicon/epoxy interface in the DCB experiments. After the model parameters were extracted from the experiments, the numerical simulations show good agreements with the direct measurements. Moreover, the model parameters extracted from different specimens at different separation rates provide a consistent description of the molecular structures at the interface, which may be used to predict the fracture of the interface under various conditions including monotonic and cyclic loadings.

Chapter 4 Mixed-mode Rate Dependent Interfacial Fracture

In this chapter, we present and discuss a series of mixed-mode fracture experiments of an epoxy/silicon interface over a range of separation rates accomplished by a dual-actuator loading device. Measurements of the forces, as well as load-point normal and tangential displacements and rotations, were used to determine the normal and tangential components of the crack tip displacements and the corresponding components of the J-integral. This was made possible because the beams identically satisfied a so-called balance condition [56] that allows the extraction of the normal and shear components of the traction-separation relations to be decoupled and determined directly by taking the derivative of the corresponding components with respect to their complementary crack tip opening displacement. The resulting data set is a testimony to the efficiency of the approach. It contains some striking differences to some commonly made assumptions about the normal and shear components of mixed-mode traction-separation relations that should provide insights for further theoretical developments.

4.1 Design of Experiment

In the mixed-mode experiments conducted by Wu et al. [57], it was observed that the mode angle based on the components of the J-integral and the crack tip displacements evolved from the nominal value at the initial crack tip in a highly non proportional manner as the cohesive zone developed and the crack achieved steady state in spite of the fact that the loading was essentially proportional. A single actuator loading concept, coupled with asymmetrical specimen geometries, was used to achieve the ranges of mode angles that was considered. Using a dual actuator device allows for a single specimen geometry to be used, thereby simplifying specimen preparation, mode angle selection and potentially allowing for nominally non proportional loading paths to be followed.

4.1.1 Dual-actuator loading device

The dual-actuator device developed here (Fig. 4.1) consists of three parts; the support structure, the specimen mount and the data acquisition system.

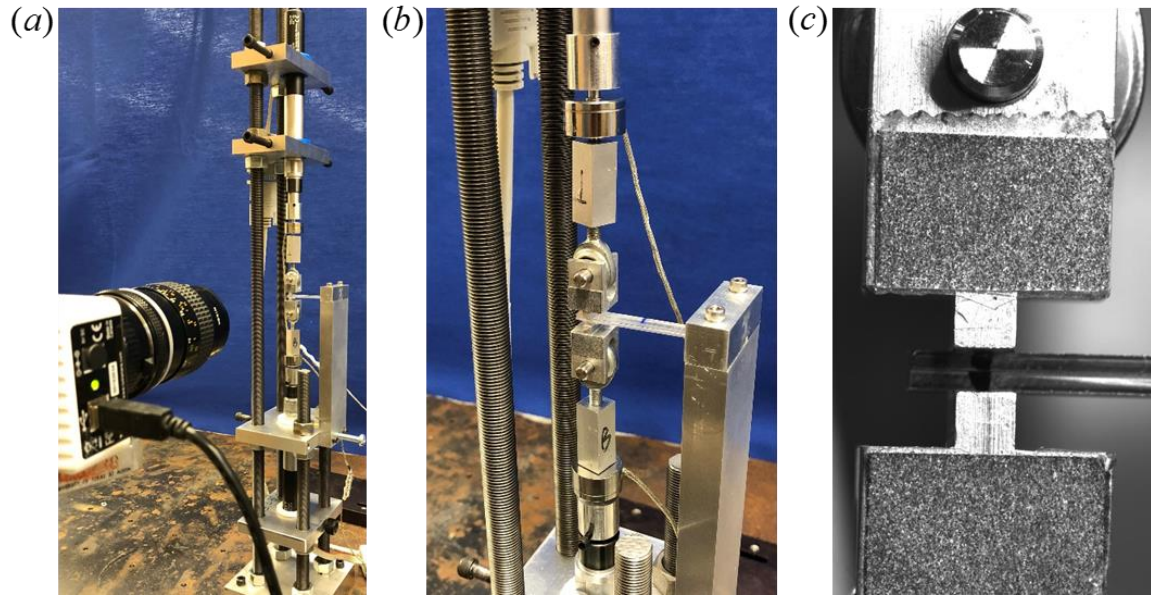


Figure 4.1 (a) Dual-Actuator Loading Device; (b) Specimen grips and installation; (c) An image of the DIC target taken by the camera during the experiment.

The rods of the support structure (Fig. 4.1a) are secured to a table using a thick aluminum block while aluminum clamps are used to grip the actuators and the specimen. Polymer sleeves protect the actuators and provide sufficient friction to react the loads on the specimen. The vertical support provides support for the clamped end of the specimen. Stress concentrations due to the clamp are mitigated by a layer of Teflon tape, thereby reducing the possibility of the clamped end of the specimen breaking. Two U-shaped loading tabs are bonded to the top and bottom surfaces of the specimen where the end-displacements are applied. Rod ends are then used to link the loading tabs to the load cells and the actuators (Fig. 4.1b). They allow for rotation and any relative lateral movement of

the loading tabs. Two DC motor actuators (PI M227.25), with a maximum extension capability of 25 mm and maximum travel velocity of 0.75 mm/s, are controlled using the controller (PI Mercury C-863) that receives commands via LabVIEW VI from a computer. The actuators are independently controlled in order to provide the specified end-displacement rates and their specifications are summarized in Table 4.1.

The measurement system consists of two load cells and a camera. The tension/compression load cells (Omega LCMFL-20N) are threaded onto an adapter which resides on the tips of each actuator. These load cells are connected to their respective Wheatstone bridges and amplifiers so that the voltage output from the load cells can be acquired via a data acquisition board that is controlled by the same LabVIEW program. As the actuator extends or contracts, the beams of the specimen experience a loading condition which causes a delamination to propagate while the corresponding tensile or compressive loads are registered using the load cells. DIC targets are attached to the two loading tabs in order to obtain the normal and tangential end-displacements and end-rotations (Fig. 4.1c). The motion of the targets are captured using a 2.2 megapixel CMOS camera (Lumenera LT225) with a framerate of 170 frames per second. However, while an experiment is running, the maximum rate is limited to 50 frames per second by the input/output characteristics of the computer. A lens (TEC-55 Computar) is used for magnifying the target and enhancing the precision of the DIC. Image acquisition is triggered in LabVIEW so that the actuator control and data acquisition of the load cell signals are all synchronized. The DIC analysis is conducted on selected regions of the two targets using GOM Correlate Software to obtain the end rotations and normal and tangential displacements at the loading point.

Table 4.1 Actuator specifications and property descriptions

PROPERTY	DESCRIPTION	SPECIFICATIO NS
Travel range	Maximum extension	25 mm
Design resolution	Resolution for position values recorded by the controller	0.0035 μm
Minimum incremental motion	Minimum extension of an actuator	0.05 μm
Maximum velocity	Maximum travel velocity	0.75 mm/s
Maximum force	Maximum force an actuator arm can withstand	± 40 N

Table 4.2 Relevant specimen geometry and materials properties

Geometries				
Width (mm)	Length (mm)	Initial crack length (mm)	Silicon thickness (mm)	Epoxy thickness (mm)
5.0	38.0	12.0	1.0	0.040

Materials			
Silicon elastic moduli (GPa)	Silicon Poisson's ratio	Epoxy elastic moduli (GPa)	Epoxy Poisson's ratio
130	0.22	2.4	0.34

4.1.2 Specimen preparation

The specimen consists of two silicon beams bonded by layer of epoxy (EP30, Master Bond Inc.). The 50×5 mm silicon strips were diced from silicon wafers. The epoxy was the same kind as used in the mode I experiments. The extracted interfacial strength (Fig. 2.15c) has proved that the plasticity of the epoxy was not triggered under symmetric loading condition. The mixed-mode loadings, on the other hand, can cause considerable amount of shear stress at the interface. In this work, both von Mises and Tresca yield criteria were adopted and used to check if plasticity in the epoxy layer had been triggered after the interfacial tractions were extracted (Fig. 4.18).

The fracture specimens were prepared following the procedures specified in Section 2.1.1, except that, in the current work, the initial crack length was fixed at ~12 mm from the loading point by coating a layer of Au/Pd film to the upper silicon beam (Fig. 4.2). The thickness of the epoxy layer was controlled by a steel spacer with a thickness of 40 μm . The coating layer has a smaller thickness of 15 nm, thereby providing a sharper crack front between the epoxy layer and the upper silicon beam. The benefit from specifying a common initial crack length across all specimens is to maintain a consistent relationship between the global separation rates at the loading point and the local ones at the crack tip, which will be discussed further in the Section 4.3.3. Further details regarding the specimen geometry and the material properties are provided in Table 4.2.

4.2 Analysis

In this section, three sets of analysis are presented for the mixed-mode fracture experiment. First, the energy-based fracture criterion is adopted to determine the critical load levels and associated end displacements and rotations under mixed-mode loading

conditions. This served as design parameters for the selection of load cells and actuators as well the constraints on the DIC system. It was followed by a mode-mix analysis that considered the elastic mismatch induced by the presence of the epoxy layer. Finally, a decoupled beam interaction analysis was implemented in order to determine the normal and tangential crack tip displacements, J-integrals for any loading configuration and, consequently, the traction-separation relations tractions of the silicon/epoxy interface.

4.2.1 *Critical load envelopes*

For the purpose of selecting actuators and load cells with appropriate ranges of measurement, the force and the displacement that are required to achieve interfacial fracture along different loading paths (mode-mix) are estimated based on beam analysis. The loading device design is based on a mixed-mode delamination criterion for the silicon/epoxy interface that is given by

$$G_I/\Gamma_I + G_{II}/\Gamma_{II} = 1, \quad (4.1)$$

where $0 \leq G_I \leq \Gamma_I$ and $0 \leq G_{II} \leq \Gamma_{II}$ and Γ_I and Γ_{II} are the mode I and mode II fracture toughness values of the interface. The mode I fracture toughness of the silicon/epoxy interface was taken to be 10 J/m^2 . In the parametric study that follows, critical envelopes were plotted at energy ratios $\Gamma_2/\Gamma_1 = 1, 5, 10$. The fracture mode-mix mode angle based on energy release rates is

$$\Psi = \tan^{-1} \sqrt{G_{II}/G_I}. \quad (4.2)$$

The specimen and loading configurations are depicted in Figure 4.2. Direct far-field measurements include forces, displacements and rotations at the loading points of both the upper and lower beams. For design purposes, the system is simplified by neglecting the presence of the epoxy layer and the corresponding free-body diagrams are given in Figure

4.2. The energy release rate at the crack tip can be written in terms of the applied forces [143] as

$$G = \frac{1}{2b} \left[\frac{(P_1 a_0)^2}{E_1 I_1} + \frac{(P_2 a_0)^2}{E_2 I_2} - \frac{(P_1 a_0 + P_2 a_0)^2}{q b E_2 h^3} \right], \quad (4.3)$$

where, $E_1 = E_2 = \bar{E}$ and $I_1 = I_2 = b h^3 / 12$. Here, $\bar{E} = E / (1 - \nu^2)$ denotes the plane-strain elastic modulus and b and h refer to the width and height of the silicon beams. The quantity q is a measure of the elastic and geometry mismatch in laminated beam system and its value is $2/3$ for the symmetrical double cantilever beam specimen. Equation (4.3) can be further partitioned into mode I and mode II components based on Williams [144], as

$$G_I = \frac{3(P_1 - P_2)^2 a_0^2}{\bar{E} b^2 h^3}, \quad (4.4)$$

$$G_{II} = \frac{9(P_1 + P_2)^2 a_0^2}{4\bar{E} b^2 h^3}. \quad (4.5)$$

Note that, for this symmetric specimen, Conroy, et al. [145] established that this portioning approach is consistent with the one [9] that is based on the use of stress intensity factors.

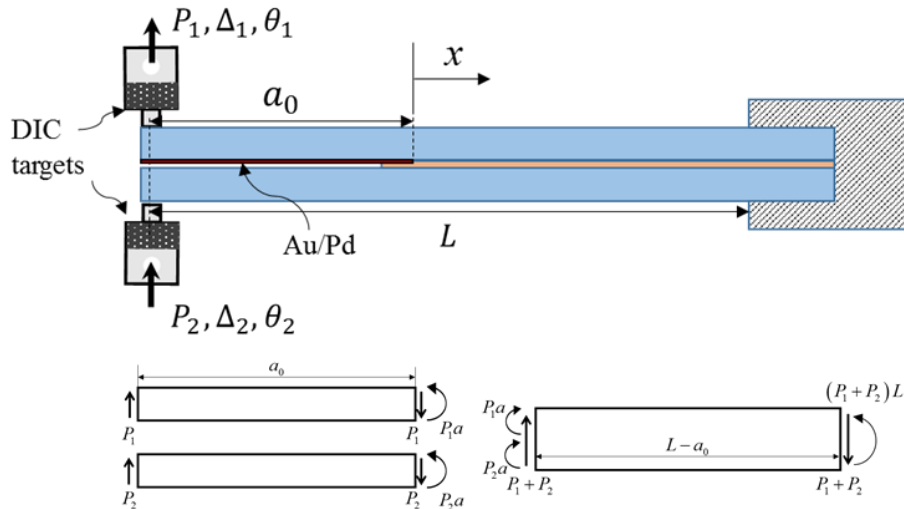


Figure 4.2 Loading configurations and free-body diagrams of the laminated beam (epoxy layer neglected).

Combining equations (4.1), (4.4) and (4.5), we obtain a critical load envelop (Fig. 4.3a) for each fracture toughness ratio, with each load pair (P_1, P_2) being the critical values of the forces that trigger fracture at the interface based on the mixed-mode fracture criterion (Eq. (4.1)). Two special cases, $P_1 = -P_2$ and $P_1 = P_2$, correspond to the mode I and mode II delamination, respectively. The envelope is symmetric with $P_1 + P_2 = 0$, but this only holds when the epoxy layer is ignored. The presence of the epoxy layer introduces an elastic mismatch between upper and lower silicon beams and causes an unsymmetrical loading path with alternate directions of the applied force. When $\Gamma_2/\Gamma_1 = 10$, the range of the critical forces is bounded by 20 N. For better measurement precision without exceeding the load limit, we chose a load cell with a 20 N capacity.

In order to establish a displacement envelope (Fig. 4.3b), we can replace the force terms in the equations (4.4) and (4.5) with the applied displacements using the following relations,

$$P_1 = \frac{3E_1I_1}{8a_0^3(1+2\beta)}(\Delta_1 + \beta(\Delta_1 - \Delta_2)) \quad (4.6)$$

$$P_2 = \frac{3E_2I_2}{8a_0^3(1+2\beta)}(\Delta_2 - \beta(\Delta_1 - \Delta_2)) \quad (4.7)$$

where, $\beta = (L^3/a_0^3 - 1)/8$. The above equations were derived under the assumption of the perfect bonding (no separation) between two beams except for the cracked portion ($x > 0$). The critical displacement at mode I fracture was estimated as 0.046 mm for both upper and lower beams. To ensure a reasonable amount of data (more than 20 data points) collected for each experiment, the displacement rates were selected as 0.001, 0.005, 0.025, 0.125 and 0.625 mm/s. The displacement envelope also suggested that the applied displacement is bounded by 1.5mm, which is 1/8 of the initial crack length (12 mm), thus using the beam equations under the small deflection assumption are justified.

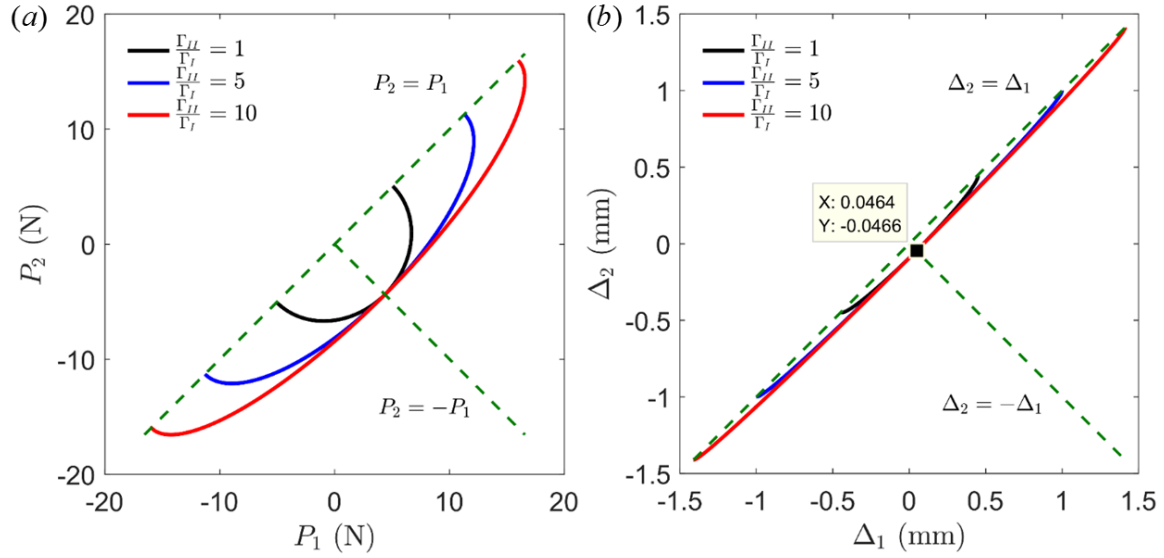


Figure 4.3 (a) Critical load envelope and (b) displacement envelope for different fracture toughness ratios (mode I fracture toughness assumed: 10 J/m²)

4.2.2 Mode mix analysis

The dual-actuator loading device offers the flexibility to control the motion of the upper and lower beams independently. Therefore, a full range of mode-mix angles is feasible by varying the loading point displacement ratio ($-1 \leq \Delta_2/\Delta_1 \leq 1$). Combining equations (4.2)-(4.7), the mode angle as a function of the applied displacement ratio is determined to be

$$\Psi = \tan^{-1} \left(\frac{2\sqrt{3}}{4+3L^*} \cdot \frac{\Delta_1 + \Delta_2}{\Delta_1 - \Delta_2} \right), \quad (4.8)$$

where, $L^* = \frac{1}{3} \left(\frac{L}{a_0} - 1 \right)^3 + \left(\frac{L}{a_0} - 1 \right)^2 + \left(\frac{L}{a_0} - 1 \right)$. By Eq. (4.8), when $\Delta_2/\Delta_1 = -1$, the specimen is subjected to symmetric opening displacements and mode I fracture is activated. On the other hand, pure mode II ($\Psi = 90^\circ$) occurs when $\Delta_2/\Delta_1 = 1$. By varying the applied displacement ratio between -1 and 1, we can obtain a full range of mode-mix angles (Fig. 4.4b). With Eq. (4.8), we can also examine the effect of the initial crack length on the mode-mix when the presence of epoxy is ignored. The mode angle is not affected by

the initial crack length at the two limiting cases $\Delta_2/\Delta_1 = -1, 1$. However, for the remaining loading paths ($-1 < \Delta_2/\Delta_1 < 1$), the mode angle does increase as the crack evolves as illustrated by the dotted lines in Fig. 4.4a.

The epoxy layer leads to an elastic mismatch at the interface and leads to a phase shift (Fig. 4.4b) in the crack tip mode-mix compared to the corresponding homogeneous system. The value of the phase shift can be determined semi-analytically as stated in Section 2.2.1. In addition, when the epoxy layer is accounted for in LEFM analyses, the mode angle depends on the crack length for a given displacement ratio, similar to the results already noted when simple beam theory was used: the mode angle initially increases with increasing crack length. However, there can be a sharp a transition where the mode angle changes drastically. We list four loading paths as examples to illustrate the variation of the mode angle (Fig. 4.4a). For all cases, the mode angle saturates when $a_0/L > 0.6$, which indicates that it is possible for the mode-mix to be independent of crack lengths in this region. The form of the transition is largely affected by the displacement ratio. When $\Delta_2/\Delta_1 = -1$, the mode angle is essentially constant at 13° before dropping to $\sim -4^\circ$. The change of sign suggests a change of the direction of the shear stress at the crack tip, and the decrease in the absolute value indicates a decrease in the mode II component. For $\Delta_2/\Delta_1 = 0$, the mode II component is strengthened without a change of direction. For $\Delta_2/\Delta_1 = 0.9$, the mode angle first rises to 90° , then flips to -90° and eventually saturates at -35° , which is smaller in magnitude than the steady state value that arises when $\Delta_2/\Delta_1 = 0.5$. Based on the LEFM results, maintaining a positive mode mix angle while achieving a fairly wide range of values of the mode-mix angle requires using an initial crack length that is about 1/3 of the total length (38 mm) and explains our use of 12 mm long initial cracks for all experiments.

With a view to exploring the full range of the mode-mix angles between 0° and 90° , the mixed-mode experiments in this study were conducted at five displacement ratios. The corresponding mode angles were based on LEFM analyses and are listed in Table 4.3. For each displacement ratio, five specimens were loaded at five displacement rates ranging from 0.001 mm/s to 0.625 mm/s.

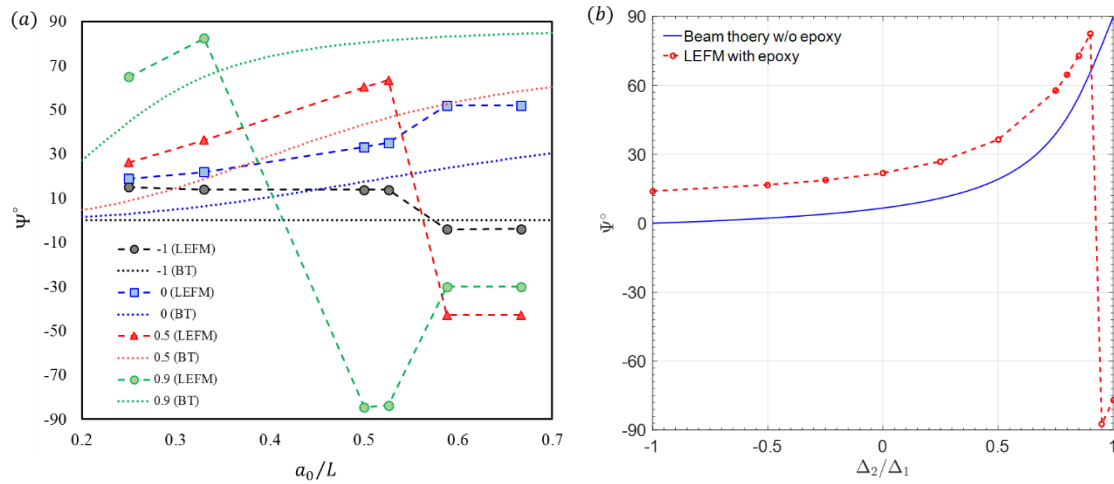


Figure 4.4 (a) Mode angle as a function of crack length (dotted lines obtained by beam theory and symbols obtained by LEFM analysis that included the epoxy); (b) Mode angle as a function of the prescribed displacement ratio ($a_0/L = 0.33$).

Table 4.3 Loading configurations and corresponding mode angle (estimated by LEFM)

Displacement ratio (Δ_2/Δ_1)	Mode angle
-1	14°
0.5	36°
0.7	50°
0.8	65°
0.95	90°

4.2.3 Crack tip displacements and J-integrals

Followed from Ouyang and Li [146] and Wu, et al. [56], the normal and shear interactions are decoupled by satisfying the balance condition (Eq. (A.9)). As a result, the governing equations (Eq. (A.10) and Eq. (A.15)) in the normal and shear directions are also decoupled.

From an elastic beam interaction analysis [56], the crack tip displacements are related to the far-field measurements as,

$$\delta_n^* = \tilde{\Delta} + \frac{\bar{P}a^3}{6D_1} - a(\theta_1 - \theta_2) \quad (4.9)$$

for the normal separation and

$$\delta_t^* = \tilde{U} - \frac{\bar{P}h_1a^2}{4D_1} \quad (4.10)$$

for the tangential separation. Here, $\tilde{\Delta} = \Delta_1 - \Delta_2$, $\tilde{U} = U_1 - U_2$, $\tilde{P} = P_1 - P_2$ and $\bar{P} = P_1 + P_2$. To differ from the separations at the newly formed crack tip, we use δ_{n0}^* and δ_{t0}^* to denote the separations at the initial crack tip. Correspondingly, the initial crack length a_0 should be used in the equations (4.9) and (4.10).

We consider a contour that encloses the interface region from the crack tip ($x = 0$) to the clamped end ($x = a - L$). By definition, J-integral can be derived as

$$J = \int_{a-L}^0 \sigma \cdot \frac{\partial \delta}{\partial x} dx. \quad (4.11)$$

Note that Eq. (4.11) is equivalent to an integral at the crack tip assuming the traction-separation relation is identical along the interface, so that

$$J = \int_0^{\delta^*} \sigma d\delta. \quad (4.12)$$

Following the derivation in the beam interaction analysis [56], we obtain the normal and shear components of J-integral as the following:

$$J_1 = \widehat{D} \left(\frac{P_1}{D_1} - \frac{P_2}{D_2} \right) (\theta_1 - \theta_2), \quad (4.13)$$

$$J_2 = \frac{\widehat{A}h_1}{2D_1} \bar{P}\tilde{U}, \quad (4.14)$$

with $\widehat{D} = \left(\frac{1}{D_1} + \frac{1}{D_2} \right)^{-1}$ and $\widehat{A} = \left(\frac{1}{E_1A_1} + \frac{1}{E_1A_1} + \frac{h_1^2}{4D_1} + \frac{h_2^2}{4D_2} \right)^{-1}$, where $A_i = E_i h_i$ is the axial stiffness and $D_i = E_i h_i^3 / 12$ is the bending stiffness of the beams.. Finally, the normal and shear tractions at the crack tip are determined by

$$\sigma^* = \frac{\partial J_1}{\partial \delta_n^*}, \quad (4.15)$$

$$\tau^* = \frac{\partial J_2}{\partial \delta_t^*}, \quad (4.16)$$

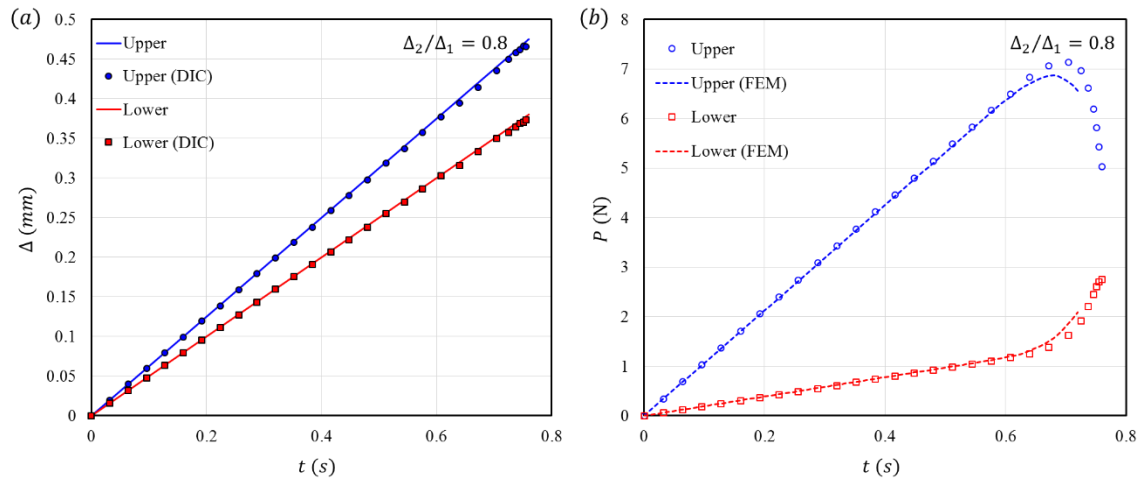
which completes the extraction of the traction-separation relations.

4.3 Results and Discussion

A total of 25 specimens (silicon/epoxy/silicon) were tested under a range of loading conditions. The values of the displacement ratio (Δ_2/Δ_1) that were considered were -1, 0.5, 0.7, 0.8 and 0.95. At each ratio, five displacement rates ($\dot{\Delta}_1$) were prescribed at the upper loading point: 0.001, 0.005, 0.025, 0.125 and 0.625 mm/s. For the nominally mode I case ($\Delta_2/\Delta_1 = -1$) specifically, the rates that were controlled are the opening rate ($\dot{\tilde{\Delta}}$). In this section, we first present the data and related analyses for one specimen ($\Delta_2/\Delta_1 = 0.8$, $\dot{\Delta}_1 = 0.625$ mm/s) following the steps as described in the Section 4.2.3. Then, we discuss the rate dependency and mode dependency of the fracture at the silicon/epoxy interface.

4.3.1 Direct measurements and crack tip traction-separation relations

The basic measurements are summarized in Figure 4.5. The nominal applied displacements compare well (Fig. 4.5a) with the DIC measurements. The close agreement between the two indicates that machine compliance was not an issue here. At the beginning, all quantities increase linearly with time, suggesting that the system is responding elastically. At $t = 0.7\text{s}$, nonlinearity can be observed among the measured forces, tangential displacements and rotations, indicating the start of crack growth at the interface. Due to the asymmetry in the loading conditions, the forces (Fig. 4.5b) behave differently at the loading points of the upper and lower beams. Once the force on the upper beam reached its peak, the rate of increase in load on the lower beam increased dramatically. This signifies a redistribution of the total force on the upper and lower beams as the crack grows. Although the normal displacements were increased at a prescribed rate, the tangential displacements (Fig. 4.5c) exhibit an accelerating separation following crack initiation. On the other hand, the relative rotation ($\theta_1 - \theta_2$) first linearly increases with time and then decreases as the crack starts to grow.



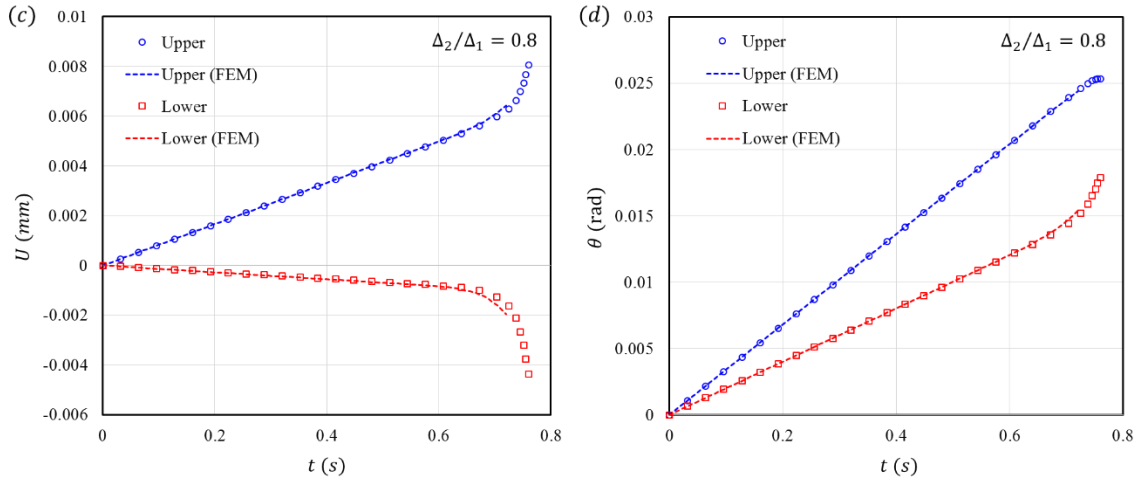


Figure 4.5 For both upper and lower beams: (a) Applied normal displacements compared with DIC measurements at the loading points; (b) Reaction forces at the loading points; (c) Tangential displacements obtained by DIC; (d) Rotations obtained by DIC. (For figures b-d, data are denoted by symbols and finite element results are denoted by dashed lines).

According to the beam on elastic foundation analysis (Appendix A), we can fit the initial linear portions of the load-displacement responses (Fig. 4.6a and Fig. 4.6b) based on the measured initial crack length and selected values for the normal and tangential stiffness of the elastic foundation. In this case, the values were similar with $K_n = 14.28 \times 10^{12}$ and $K_t = 16.25 \times 10^{12}$. In the past [65, 147], the foundation stiffness was obtained from ratio of the tensile modulus and thickness of the epoxy layer, based on a simple strength of materials argument. However, in the present work, the normal stiffness yielded by such an analysis was $71.4 \times 10^{12} \text{ N/m}^3$ or a factor of five larger than the one extracted from our beam on elastic foundation analysis. The ratio of the shear modulus and thickness of the epoxy was used to compute the tangential stiffness of the foundation at $26.7 \times 10^{12} \text{ N/m}^3$, yielding a difference that is less than a factor of two. Nonetheless, both results suggest that lower stiffness values reflect the presence of interfacial interactions that are more compliant than those of the bulk epoxy. This could be due to the formation of an interphase region, whose

presence has been postulated [148] due to the migration of the amido amine hardener to the interface and a resultant, off-stoichiometric cure close to the substrate.

Based on these results, the beam on elastic foundation analysis was subsequently used to monitor crack growth. Given the stiffness in both directions, the crack length was extracted (Fig. 4.6c) using Eqs. (A.16) and (A.19). The results indicate that, within measurement uncertainty, the two equations yield the same crack length over the entire experiment, implying that one crack front was shared by the normal and shear interactions, as noted by Wu, et al. [56].

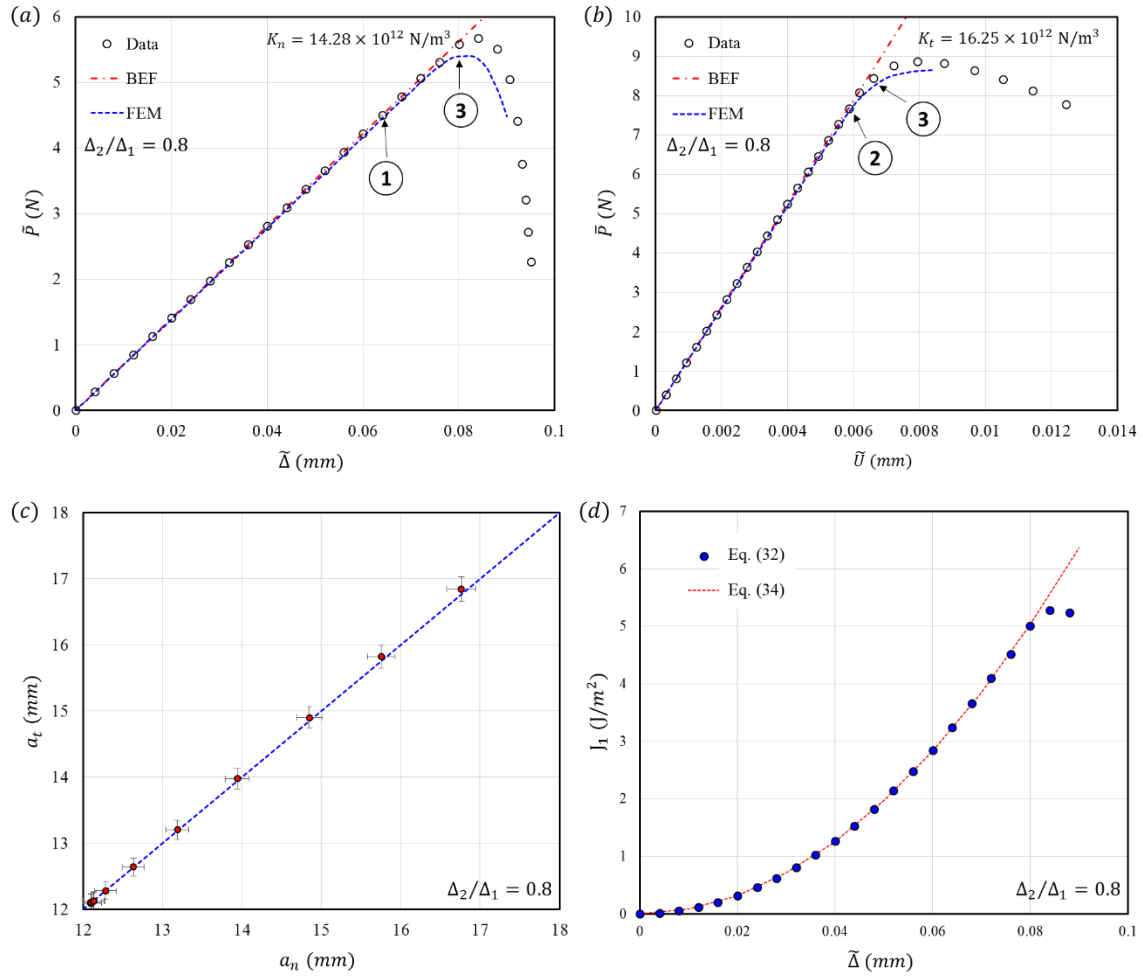


Figure 4.6 (a) Force difference (\tilde{P}) versus the normal separation ($\tilde{\Delta}$) at the loading point (red dashed line obtained by Eq. (A.16), blue dashed line obtained by FEM); (b) Force combination (\bar{P}) versus the tangential separation (\tilde{U}) at the loading point (red dashed line obtained by Eq. (A.19), blue dashed line obtained by FEM); (c) Crack lengths estimated by Eq. (A.16) and Eq. (A.19) (dashed line labeling $a_t = a_n$); (d) A comparison for J_1 obtained by Eq. (4.13) and Eq. (4.17).

In deriving the J-integrals via Eq. (4.12), we used the general formulation for the tractions in the cohesive zone and assumed that the traction-separation relations were the same at all locations within the cohesive zone. Up to the point where damage starts to occur ($\tilde{\Delta} = 0.08$ mm in Fig. 4.6d) and the load-displacement departs from linearity (Fig. 4.6a), the value of the J integral obtained by Eq. (4.13) is consistent (Fig. 4.6d) with the one obtained via beam theory [55]:

$$J_1 = \frac{3(\bar{P}a)^2}{Eb^2h^3} (1 + (\lambda_n a)^{-1})^2. \quad (4.17)$$

However, the picture becomes more complicated thereafter as will now be discussed.

Both the normal and shear components of the J-integral are plotted (Fig. 4.7a) versus applied displacement ($\tilde{\Delta}$). Both components initially exhibit a quadratic increase with applied displacement along with the total value of the J-integral ($J = J_1 + J_2$). However, once damage begins ($\tilde{\Delta} = 0.08$ mm), J_2 increases more quickly at the expense of J_1 (Fig. 4.7a), so that the J-integral reaches steady state. This behavior also manifests in the resistance curve (Fig. 4.7b). Based on the J-integral, the initial toughness (Γ_0), where the crack starts to grow, was 12.5 J/m², and the resistance reached the steady-state toughness (Γ_{ss}) of 16.1 J/m² once the crack had grown about 4 mm.

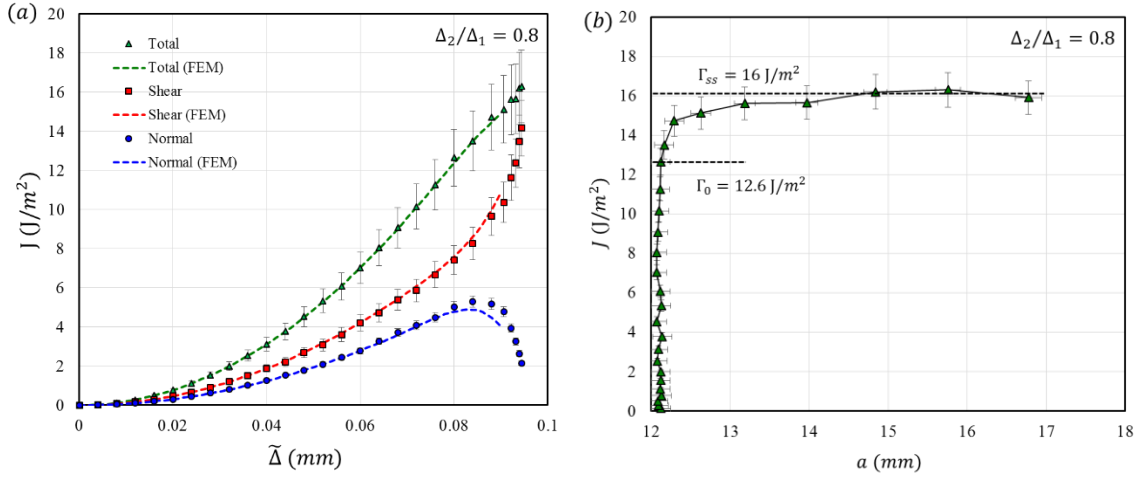


Figure 4.7 (a) Variation of J-integral components with applied displacement; (b) Resistance curve.

Following Eq. (4.9) and Eq. (4.10), the crack tip separations in both the normal and tangential directions were determined based on the far-field measurements. In preparation for the extraction of the traction-separation relations, we first plotted the normal and shear components of the J-integral versus their corresponding components of separation (Fig. 4.8a) up to the point where damage initiated ($\tilde{\Delta} = 0.08$ mm). The data was fitted to the functional form:

$$J_i = \begin{cases} K_i(\delta_{i0}^*)^2/2 \\ a/(1 + b \cdot \exp(-c\delta_{i0}^*)) \end{cases}, \quad (4.18)$$

where $i = 1, 2$ for the normal and shear interactions, respectively. The first part is a quadratic function to describe the initial elastic opening (Fig. 4.8a). This results in tractions that are linear in their respective separation. The second part is a logistic function that requires three fitting parameters. Another parameter that needs to be determined is the transition separation (δ_{i0}), at which the first part transitions to the second part. It was determined by satisfying continuity in both J-integral components (Fig. 4.8a) and tractions

(Fig. 4.8b). Unlike the commonly assumed traction-separation relations, this transition separation does not necessarily correspond to the maximum traction. For example (Fig. 4.8b), the normal and shear components of transition separation were 0.35 and 0.5 μm , respectively. This also suggests that the damage starts to accumulate towards the end of the rising portion of the traction-separation relation, which is consistent with the bond rupture kinetics model [139]. For this particular specimen, the maximum values of normal and shear tractions were 9.0 MPa and 12.6 MPa, respectively. The descending portion of the traction-separation relation ends approximately at 2 μm for both normal and shear interactions.

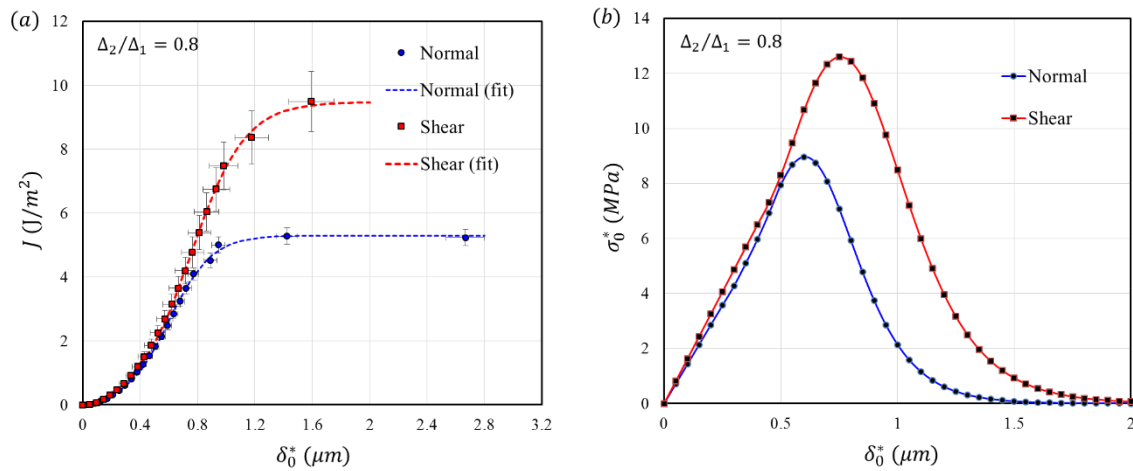


Figure 4.8 (a) J-integrals plotted versus the (initial) crack tip separations; (b) Crack tip traction-separation relations.

The variation of mode angle was considered in Figure 4.9 for a number of cases. The exercise is repeated here for the loading path $\Delta_2/\Delta_1 = 0.8$ as the crack grew during the experiment. The data marked J was obtained from the mode angle defined by Eq. (4.2) and using the J-integral values obtained from Eq. (4.13) and Eq. (4.14) as the crack grew. It is compared (Fig. 4.9) with the mode angle obtained from beam theory and the applied displacement ratio (Eq. (4.8)). This does not account for the presence of the epoxy,

whereas the LEFM analysis, which is also shown, did include the interlayer effect. It can be seen that the variation in mode angle during the development of the cohesive zone is bracketed by the beam theory and LEFM results. The development of the mode angle during crack growth can also be tracked via the crack tip displacements (CTD), if the definition of mode angle is based on

$$\Psi = \tan^{-1}(\delta_t^*/\delta_n^*). \quad (4.19)$$

This approach has been followed by groups in the past where the CTD values were able to be experimentally determined [17, 30] and data is marked as CTD in Figure 4.9.

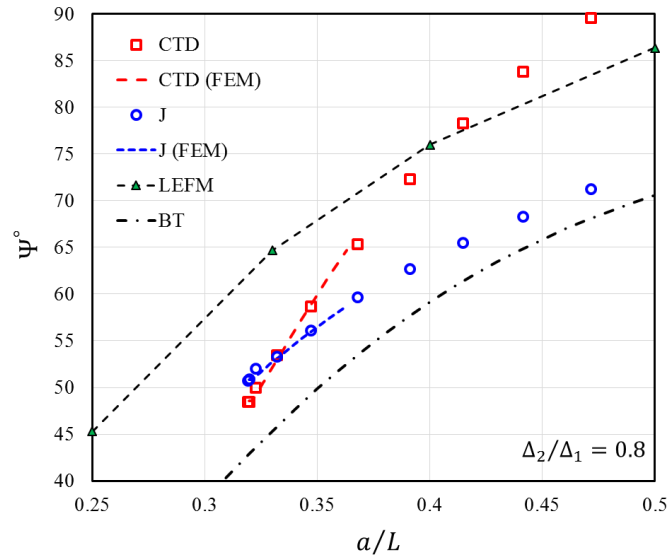


Figure 4.9 The variation in mode angle as the cohesive zone develops, based on beam theory (BT), LEFM, J-integral (Eq. (4.2)) and crack tip displacements (Eq. (4.19)).

As was seen in Figure 4.4, accounting for the presence of the epoxy in LEFM analyses consistently leads to higher mode angles than the beam theory (Eq. (4.8)) result, at least over the range of crack growth that was considered in this experiment. The increase in mode angle from the one obtained from beam theory was much smaller when the measure based on the components of the J-integral (Eq. (4.2)) was used. Since the J-

integral was determined based on the interactions between the beams, this result suggests that they mitigate the elastic mismatch induced by the epoxy layer. The variation in mode angle with crack extension that was based on crack tip displacements (Eq. (4.19)) initially matched the J-integral result, but soon grew faster and eventually exceeded the mode angles that were obtained from the LEFM analysis. This may mirror the more local nature of the measure based on crack tip displacements, which also reflect the damage that accumulates in the cohesive zone.

4.3.2 Loading rate effect

The steps described above were followed for each specimen that was tested. For illustration purposes, we now present the results at different applied displacement rates at an applied displacement ratio of $\Delta_2/\Delta_1 = 0.8$ or the same nominal mode angle.

From the elastic foundation analysis, we extracted the stiffness in both the normal and tangential directions (Table 4.4). The values are insensitive to changes in the applied displacement rate. Taking the average, the normal and tangential stiffness values are $K_n = (16.6 \pm 2.2) \times 10^{12}$ N/m³ and $K_t = (18.0 \pm 1.3) \times 10^{12}$ N/m³. These values were subsequently used to estimate the crack growth during the experiment (Eq. (A.16) and Eq. (A.19)) and to extract the traction-separation relations using Eq. (4.18).

Table 4.4 Stiffness of the elastic foundation in normal and tangential directions

Displacement rate $\dot{\Delta}_1$ (mm/s)	Normal stiffness K_n ($\times 10^{12}$ N/m ³)	Tangential stiffness K_t ($\times 10^{12}$ N/m ³)
0.001	16.9	17.8

0.005	18.8	19.4
0.025	13.9	19.6
0.125	19.3	16.8
0.625	14.3	16.3

The resistance curves are plotted for the current applied displacement ratio at five displacement rates in Figure 4.10. The total toughness is clearly rate-dependent. The energy required to drive a crack increases with the global displacement rate. This is true for both the initiation (Γ_0) and steady-state (Γ_{SS}) toughness values. The cohesive zone length, which is reflected in the transition from initiation to steady state, is also rate-dependent. The lower the displacement rate, the longer it takes for the cohesive zones to develop. Using Eqs. (4.9)-(4.10) and (4.13)-(4.16), along with the fitting procedures presented in the previous section, we extracted the traction-separation relations in the normal (Fig. 4.11a) and tangential (Fig. 4.11b) directions. The initial linear portion of the traction-separation is essentially rate-independent, as suggested by the discussion around stiffness values (Table 4.4). The strength (maximum traction) and critical separation (interaction range) are rate-dependent with both increasing with increasing applied displacement rate. Comparing the normal and shear interactions at each applied displacement rate, the stiffness, strength and the range of the interactions are consistently greater in the tangential direction for this loading condition.

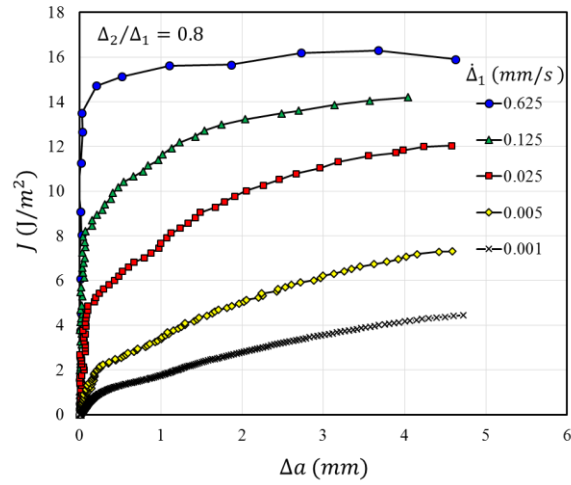


Figure 4.10 Resistance curves for specimens tested at different applied displacement rates.

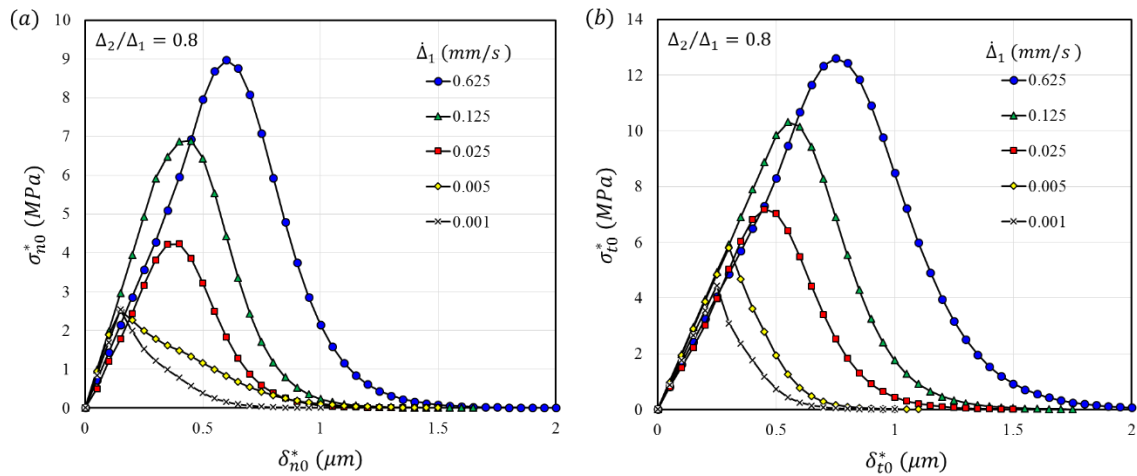


Figure 4.11 (a) Normal and (b) shear components of the traction-separation relations at the initial crack tip.

Following from the results shown in Figure 4.9, it is interesting to observe the evolution in the mode angle as the cohesive zone develops at each applied displacement rate. The mode angle at the initial crack tip is rate independent (Fig. 4.12a), no matter which measure of mode angle is used. Similar to the results shown in Figure 4.9, the mode angle at the initial crack tip is bounded by the values obtained from beam theory and LEFM.

Compared to a homogenous system (beam theory), the mode angle shift at the current displacement ratio is about $\sim 17^\circ$. On the other hand, the evolution of mode angle based on both J-integral is independent of the rate at which the displacements were applied. The same is true of the crack tip displacements, particularly in the initial stages of the development of the cohesive zone and there is no clear ordering of the trends by applied displacement rate later on (Fig. 4.12b).

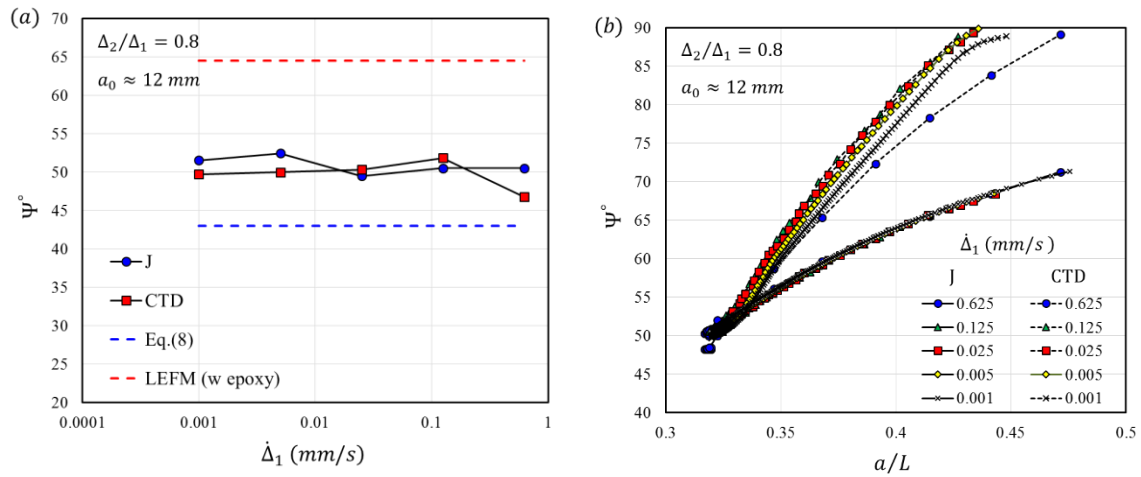


Figure 4.12 Crack tip mode angle at different applied displacement rates, (a) comparing mode angle measures at the initial crack length and (b) the effect of applied displacement rate on mode angle, based on J-integral and crack tip displacements, as the cohesive zone develops.

4.3.3 Global rate vs local rate

The displacement rate was controlled globally as a constant in each of the experiments that was conducted. Previously, we derived the local separation rate in mode I interface fracture based on the beam on elastic foundation analysis [139] through

$$\delta_n^* = \dot{\Delta} \left(\frac{2}{3} (1 + \lambda_n a)^2 + \frac{1}{3} (1 + \lambda_n a)^{-1} \right)^{-1}. \quad (4.20)$$

This equation relates the normal separation rate ($\dot{\delta}_n^*$) at each crack tip to the global separation rate ($\dot{\tilde{\Delta}}$). It clearly indicates that the local separation rate in the normal direction decreases with increasing crack length when the global rate is kept constant. Similarly, we can derive the local rate in the tangential direction based on Eq. (4.10) as

$$\dot{\delta}_t^* = \dot{\tilde{U}} \left(1 - \left(1 + \frac{2}{\lambda_t a} + \frac{2}{(\lambda_t a)^2} \right)^{-1} \right). \quad (4.21)$$

With a constant global tangential separation rate ($\dot{\tilde{U}}$), the local tangential rate ($\dot{\delta}_t^*$) also decreases with increasing crack length. However, since $\dot{\tilde{U}}$ is not controlled in the experiment, it was only constant (Fig. 4.5c) prior to the onset of damage. For this shear-dominant loading condition, once $\dot{\tilde{U}}$ starts to increase, it dominates and the local tangential rate increases as crack grows (Fig. 4.13a), while the local normal rate ($\dot{\delta}_n^*$) decreases with increasing crack length. For the current applied displacement ratio, the normal and tangential rates begin with similar values ($\sim 2 \mu\text{m/s}$) at the initial crack tip. Following crack growth, the increase of $\dot{\delta}_t^*$ is much larger than the decrease of $\dot{\delta}_n^*$, so that the magnitude of the vectorial separation rate ($\dot{\delta}^* = \sqrt{\dot{\delta}_n^2 + \dot{\delta}_t^2}$) also increases as the crack evolves. If the J-integral ($J = J_1 + J_2$) is plotted as a function of the log of the vectorial separation rate, the response (Fig. 4.13b) corresponds to the resistance curve (Fig. 4.10), apart from the logarithmic scale. When the crack tip remains in its initial position, the initial separation rate also remains constant as the J-integral increases. After reaching the initiation toughness (Γ_0), the crack advances and the local separation rate increases. Again, in direct correspondence to the resistance curves, the J-integral achieves steady state with respect to the vectorial crack tip separation rate. This is due to the rapidly increasing local separation rate. Alternatively, plotting the dependence of the steady state toughness on crack tip displacement rate in logarithmic form suggests (Fig. 4.13c) that there are two different rate dependent mechanisms at play. It should be also noted that we only

considered the elastic opening of the interface in deriving Eqs. (4.20) and (4.21). Once damage begins to occur, the estimate provided by these two equations will be smaller than the actual values. On the other hand, the confidence level in these equations is higher when the crack is at the initial position, as the damage zone has not developed yet.

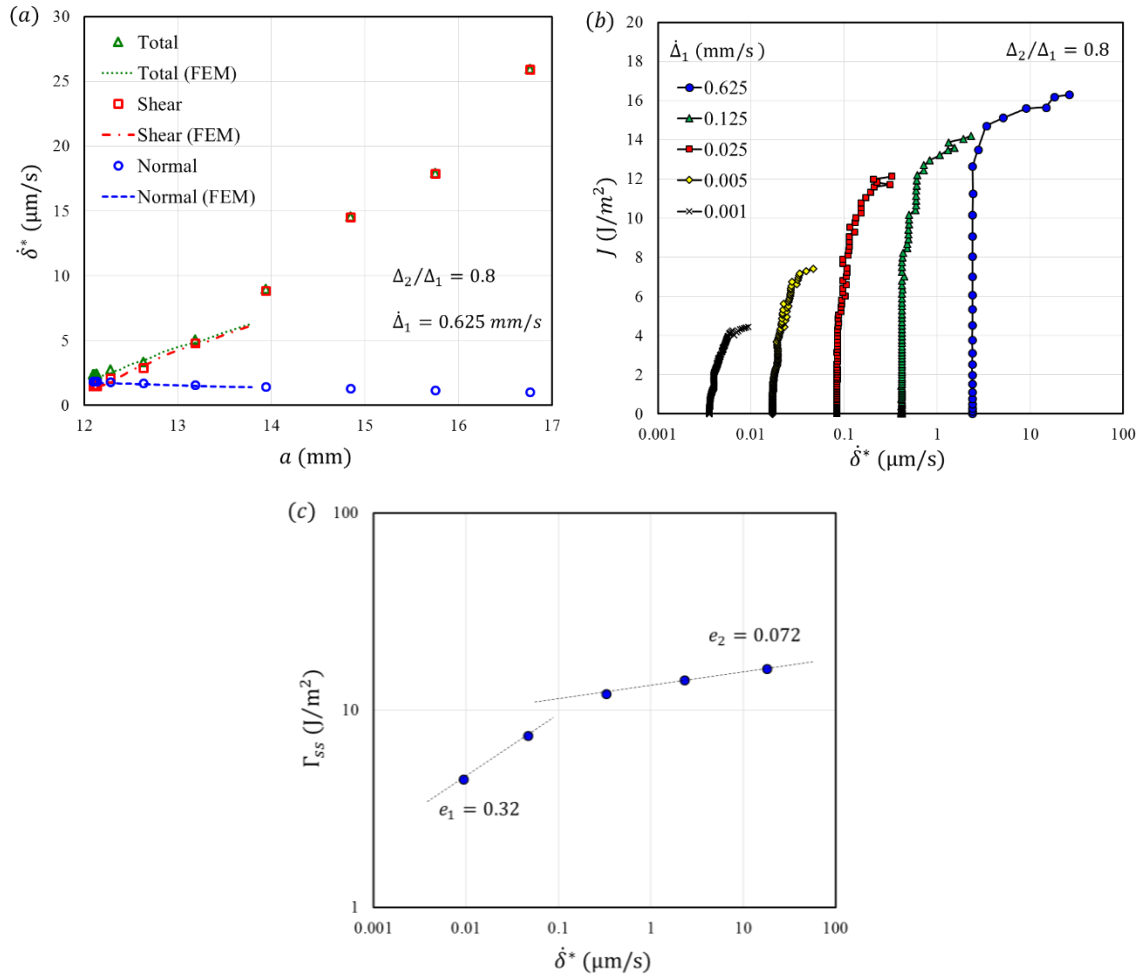


Figure 4.13 (a) Crack tip vectorial separation rate and its normal and shear components; (b) Toughness ($J = J_1 + J_2$) versus local separation rate ($\dot{\delta}^* = \sqrt{\dot{\delta}_n^2 + \dot{\delta}_t^2}$) at five displacement rates; (c) Steady state toughness (Γ_{ss}) versus the local separation rate with the slopes labeled as $e_1 = 0.32$ for the two lower rates, $e_2 = 0.072$ for the three higher rates.

4.3.4 *Loading mode effect*

So far, we have examined the rate effect for a particular applied displacement ratio ($\Delta_2/\Delta_1 = 0.8$). In this section, we focus on the effect of the applied displacement ratio on the interfacial properties and mode angle at the crack tip. We are also interested in the combined effect of the loading mode and loading rate on the initiation of fracture from the initial crack tip. The analyses described in previous sections were followed for specimens at each prescribed applied displacement ratio (Table 4.5).

Although it is not shown here, the interfacial stiffness values listed in Table 4.5 are the average and standard deviations across all rates as the rate-independent trend established in Table 4.4 and Figure 4.11 was repeated at all applied displacement ratios. However, these stiffness values exhibit a clear dependence on the applied displacement ratios. Both normal and tangential stiffness increase with increasing applied displacement ratio. The interaction is stiffened in the transition from mode I to mode II dominant fracture, which suggests that different interaction mechanisms are activated. It should be also noted that both components increase, but the values are similar at each displacement ratio. Though we initially assumed that the two spring relations in the normal and tangential directions were independent, the results suggest the possibility of a single spring that rotates with the mode angle and stiffens. Taking this idea one step further, we may consider replacing the spring with molecular chains, crosslinks or polymer ligaments that reflect the interaction between the epoxy and silicon.

Table 4.5 Interfacial stiffness in the normal and tangential directions

Displacement ratio Δ_2/Δ_1	Normal stiffness K_n ($\times 10^{12}$ N/m ³)	Tangential stiffness K_t ($\times 10^{12}$ N/m ³)
-1	9.27±1.1	8.2±1.4
0.5	12.6±0.8	13.0±0.9
0.7	13.5±1.4	14.8±1.5
0.8	16.6±2.2	18.0±1.3
0.95	19.0±2.0	21.8±1.9

The variation in local mode angles based on ($\Psi = \tan^{-1} \sqrt{J_2/J_1}$) at the initial crack is compared (Fig. 4.14a) with the measures from LEFM and beam theory as a function of the loading condition. At each applied displacement ratio, the average mode angle is bracketed by LEFM and beam theory predictions as the upper and lower bounds, respectively. The local mode angle increases as the crack evolves (Fig. 4.14b), except for the nominally mode I condition, where the mode angle remains essentially constant (consistent with Fig. 4.4a). Although it is not shown here, the independence of mode angle on the applied displacement rate (Fig. 4.12b) at $\Delta_2/\Delta_1 = 0.8$ was also observed under all the other loading conditions. Furthermore, following crack growth, the mode difference at the initial crack length is preserved for the three intermediate applied displacement ratios.

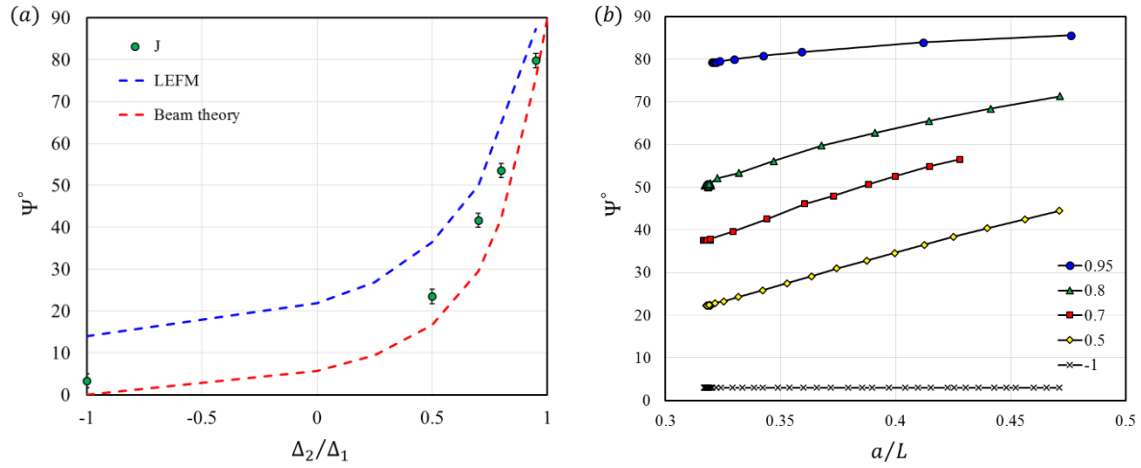


Figure 4.14 (a) Average values and deviation of mode angles ($\Psi = \tan^{-1} \sqrt{J_2 / J_1}$) obtained at the initial crack length compared with results from LEFM (with epoxy) and beam theory analyses; (b) Variation in mode angles during crack growth at five prescribed displacement ratios.

The variation of the initiation toughness (Γ_0) and its components at the onset of damage with the local separation rate and mode angle is now considered. We plot these quantities versus the corresponding crack tip separation rates at each displacement ratio (or nominal mode angle, as indicated in Fig. 4.15a). These double logarithmic plots suggest a power law rate dependence for the both components of the J-integrals. A constant exponent ($e_1 = e_2 = 0.34$) is observed for the normal component (Fig. 4.15a). Except for the nominally mode II condition, the rate dependence can be fitted by one power law function for all the other mode angles. The downward shift indicates a smaller multiplier for the nominal mode II case. The shear component is more complicated (Fig. 4.15b), as the multipliers are different for each mode angle. Except the nominally mode I case ($e_4 = 0.14$), a universal exponent ($e_3 = 0.25$) exists across all the other loading conditions, though it is not as strong as it was in the normal direction. The total (initiation) toughness does not exhibit a uniform power law rate dependence (Fig. 4.15c) across all loading

conditions. However, we were able to provide two power law functions as the upper ($e_5 = 0.25$) and lower ($e_6 = 0.28$) bounds. In conclusion, the initiation of fracture is clearly rate dependent, and the rate dependence is close to a power law relation. The rate dependence also depends on the mode angle at the crack tip and the interface is in general toughened as the mode angle increases.

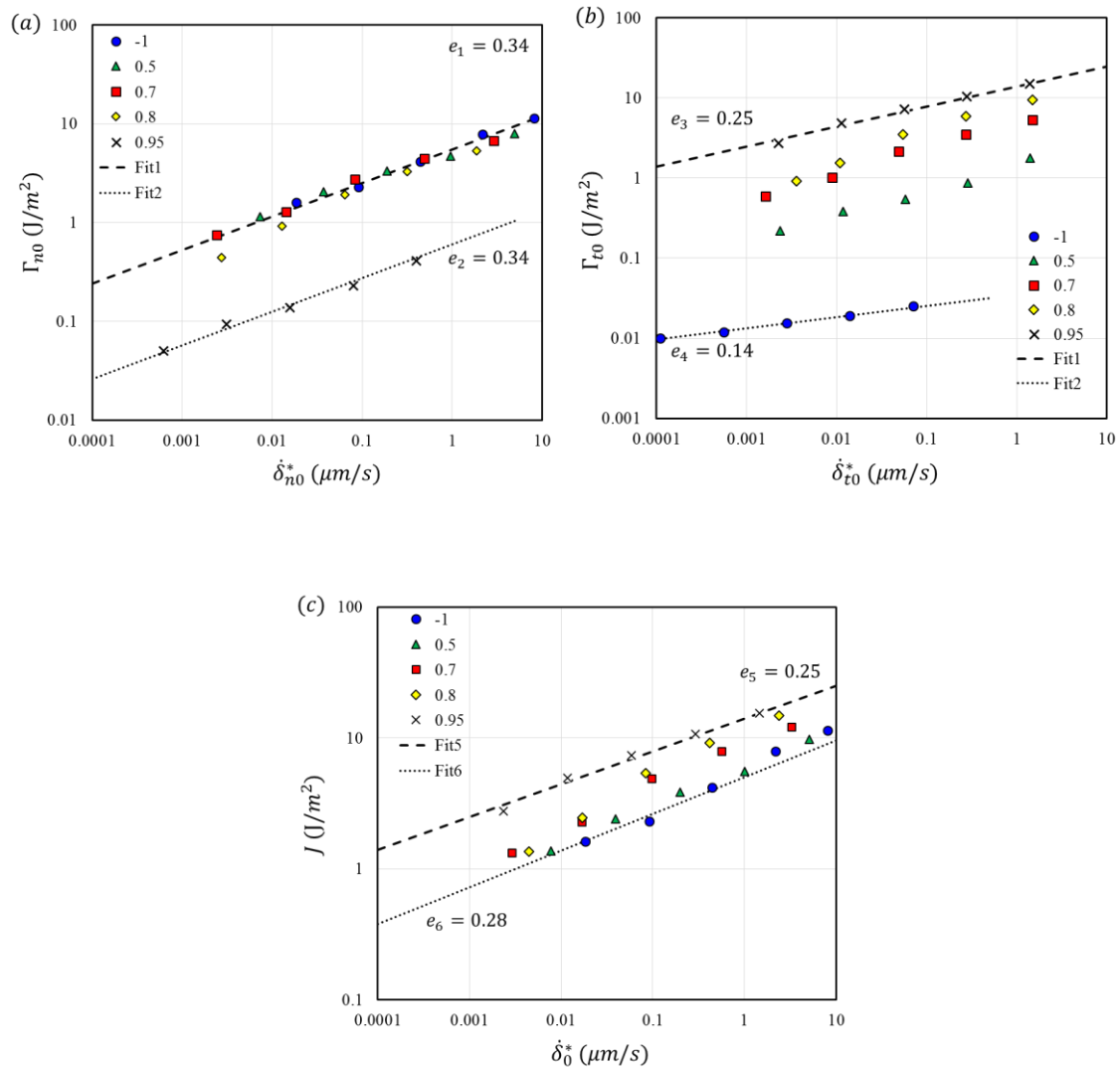


Figure 4.15 For all specimens, double logarithmic plots of the initiation toughness versus crack tip separation rate: (a) normal toughness versus normal rate, (b) shear toughness

versus tangential rate and (c) total toughness versus vectorial rate (upper and lower bounds fitted by power law functions with exponents labeled).

Other interfacial properties, such as the strengths (σ_0^*) and ranges (δ_c^*) of the interactions, are plotted versus local separation rate and mode angle via their normal and shear components (Fig. 4.16). Both components depend on the crack tip separation rate and mode angle. For the normal components, the rate dependence is stronger when the mode angle is closest to mode I. On the other hand, the shear components exhibit more rate effects in the nominally mode II case. For both normal and shear components, the mode dependence is intensified at higher local separation rates.

The paths that the J-integrals (J_2 versus J_1) and crack tip displacements (δ_t^* versus δ_n^*) followed as crack grew are plotted at five prescribed displacement ratios as shown in Figure 4.17. The initial response is proportional in both cases, indicating that the mode angle remains constant at the initial crack tip (Fig. 4.12a). After reaching the damage initiation, the crack started to grow and the local separation rate varied with crack length (Fig. 4.13a). Correspondingly, the paths that were followed deviate from the linear curve and shift toward mode II, except for the nominal mode I loading case ($\Delta_2/\Delta_1 = -1$), where both J-integrals and crack tip displacements are dominated by the normal components. The initial slope of the loading path is mainly determined by the prescribed displacement ratio. However, the transitions in the loading paths present more dependence on the variations of the local separation rates: As the crack grows, the increase in the tangential rate corresponds to the increases in J_2 and δ_t^* , the decrease in the normal rate corresponds to the decrease in J_1 and δ_n^* . In the nominally mode I case, the initial symmetry was preserved during the crack growth, and thus no apparent increase in the shear components was detected.

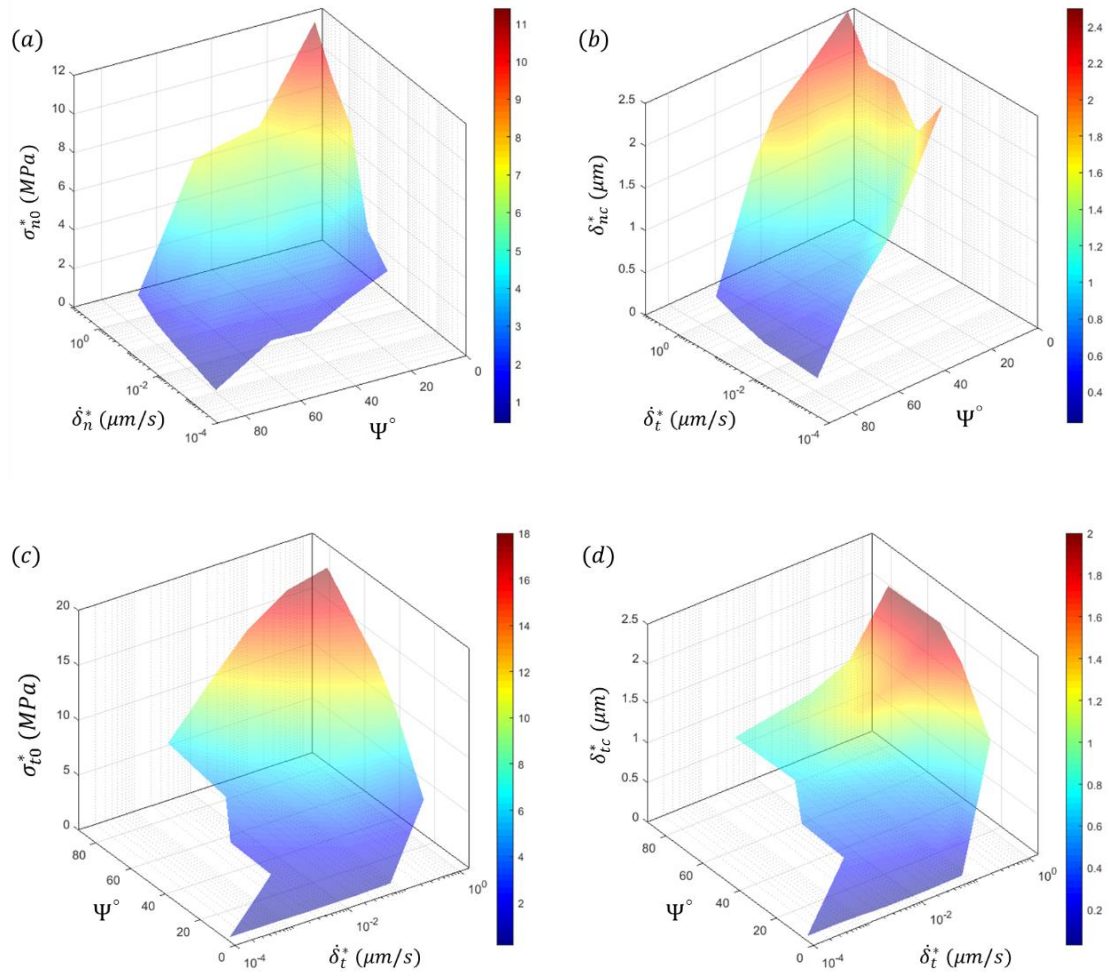


Figure 4.16 Surface plots of (a) normal strength (σ_{n0}^*), (b) normal critical separation (δ_{nc}^*), (c) shear strength (σ_{t0}^*) and (d) tangential critical separation (δ_{tc}^*), versus corresponding crack tip separation rates and mode angles.

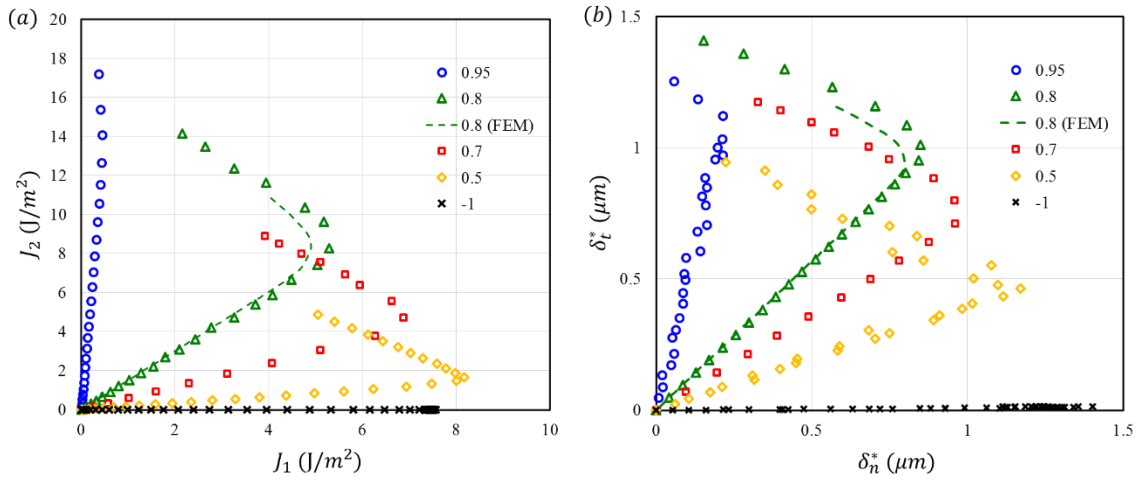


Figure 4.17 Loading path by (a) J-integrals and (b) crack tip displacements, at five prescribed displacement ratios with highest global rate.

4.3.5 Finite element validation

The analyses in Section 4.2.3 enables the direct extraction of the traction-separation relations using the crack tip displacements at the initial crack tip (Fig. 4.8 and Fig. 4.11). However, the normal and tangential components of the local separation rates varies with increasing crack length, which causes variations in the normal and shear components of the J-integrals (Fig. 4.7a) and may lead to traction-separation relations that vary along the cohesive zone. Nonetheless, it is still worthwhile to examine the validity of the extracted traction-separation relations.

The extracted traction-separation relations (Fig. 4.8b) were implemented at the interface between the upper silicon strip and the epoxy layer via an ABAQUS user-defined subroutine (UINTER). In the subroutine, a cohesive surface interaction was defined, where both the surface traction and Jacobian matrix are required as input variables. In a two-dimensional setting, the latter is defined by

$$J = \begin{bmatrix} \frac{\partial \sigma_n}{\partial \delta_n} & \frac{\partial \sigma_n}{\partial \delta_t} \\ \frac{\partial \sigma_t}{\partial \delta_n} & \frac{\partial \sigma_t}{\partial \delta_t} \end{bmatrix} \quad (4.22)$$

Following the balance condition, the off-diagonal terms were set to zero. The normal and shear components of the traction and stiffness are defined by first and second derivatives of the functional form of the J-integrals (Eq. (4.18)), respectively. Apart from the surface interaction, both silicon beams and epoxy layer were modeled by plane strain quadrilateral elements (CPE8), with the linear elastic properties that were defined in Table 4.2. Fixed boundary conditions were prescribed at the clamped end and the displacement ratio ($\Delta_2/\Delta_1 = 0.8$) was applied at the loading end, using the highest displacement rate ($\dot{\Delta}_1 = 0.625$ mm/s) that was used in the experiments.

The numerical results (labeled FEM) obtained by the finite element model were compared with the direct measurements in Figure 4.5. Close agreement can be observed during the linear portion of the response for the forces (Fig. 4.5b), tangential displacements (Fig. 4.5c) and rotations (Fig. 4.5d), before the deviation occurs approximately at $t = 0.64$ s. Recall that the traction-separation relations that were used in the finite element analysis were based on the assumption that both components of the J-integral achieved steady state behavior, which was in fact only true of the total J-integral. The deviation of the finite element solution from the measured responses is now explored.

The measured load-displacement responses (Fig. 4.6a-b) compare well with the finite element results in the linear portions of the responses. The load difference (\tilde{P}) obtained from the finite element solution (Fig. 4.6a) starts to deviate from the linear regime at point ① and reaches its peak at point ③ at a 4.8% lower load value than was measured. This could be due to the assumption that both components of the J-integral reached steady state for the extraction of the traction-separation relations. The peak value corresponds to

the instant at which the damage is complete and the normal and shear tractions (Fig. 4.18a) return to zero at the initial crack tip. Correspondingly, the force combination (\bar{P}) deviates (Fig 4.6b) from linearity at point ②, however, it continues to increase once separation at the initial crack tip is complete (point ③). Based on the measurements, the force combination eventually reaches a maximum, but it was not possible to obtain a solution in that portion of the response. This was due to the contact overclosure in the compressive region ahead of the cohesive zone.

The finite element solution for the two components of the J-integral were each determined by integrating the tractions and separations within the cohesive zone (Eq. (4.11)). They are consistent with the results obtained by using the beam kinematics (Eq. (4.13)-(4.14)) to determine the J-integral components (Fig. 4.7a). This is interesting because the latter are based solely on the elastic portions of each traction-separation relation and suggests that the damaging portions of the traction-separation relations did not contribute much to the finite element determination of the J-integral components. The finite element solutions for mode angles during the development of the cohesive zone were also consistent with measured values (Fig. 4.9). This was true for the mode angle measures based the components of both the J-integral and the crack tip displacement. The crack tip separation rates that were computed as the cohesive zone developed (Fig. 4.13a) were in agreement with the values that were extracted experimentally. The paths taken by the components of the J-integral and crack tip displacements from the finite elements solution for $\Delta_2/\Delta_1 = 0.8$ compare well (Fig. 4.17) with the measurements in the linear regime but do not capture portion of the response where the mode II components increase at the expense of the mode I components. This can again be traced to the steady state responses that were assigned to J_1 and J_2 .

As the cohesive zone begins to develop ahead of the crack tip, both crack tip tractions (Fig. 4.18a) increase linearly in concert with the load-displacement responses (Fig. 4.6a-b). The normal traction first reaches its maximum (point ①) and then decreases as the shear traction continues to increase until it reaches the shear strength (point ②). From then on, both the normal and shear tractions decrease until they vanish simultaneously (point ③). These two contrasting responses led, respectively, to the noted decrease in J_1 and increase in J_2 as the total value of the J-integral reached steady state (Fig. 4.7a). The contrasting responses were also responsible for the increase in the mode angle as the cohesive zone developed (Fig. 4.9).

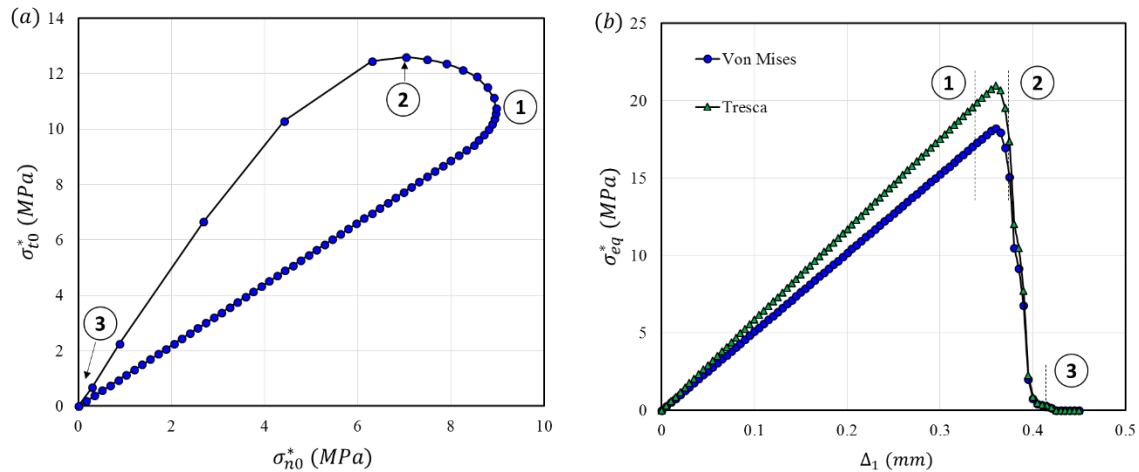


Figure 4.18 (a) Shear traction versus normal traction at the initial crack tip obtained by FEM; (b) Equivalent stress by von Mises yield criterion and Tresca yield criterion.

In order to address the possibility of yielding in the epoxy contributing to the nonlinear portions of the responses that have been examined, the stress level in the epoxy at the initial crack tip was evaluated by two yield criteria: von Mises and Tresca (Fig. 4.18b). The results were similar, with the Tresca criterion presenting a higher equivalent stress (~ 21 MPa). The yield strength of the epoxy under shear was 24 MPa, which gives rise to a von Mises yield strength ($\sigma_{eq} = \sqrt{3}\tau_y = 41.6$ MPa) and means that plastic

dissipation in the epoxy was not triggered at the initial crack tip as the cohesive zone developed. This particular loading configuration ($\Delta_2/\Delta_1 = 0.8, \dot{\Delta}_1 = 0.625 \text{ mm/s}$) was close to the upper bound of the fracture toughness (Fig. 4.15c) for the silicon/epoxy interface so that yielding is not expected in any of specimens that were tested and the development of damage was the sole contributor to the nonlinear portions of the responses.

4.3.6 *A simple extension of the rate-dependent cohesive zone model*

The proposed rate-dependent cohesive zone model (Chapter 3) may be used to simulate mixed mode fracture at the interface. Consider stretching a chain in the vectorial direction with an angle θ (Fig. 4.19). Along the chain direction, the chain force versus chain stretch and the damage process remain the same as discussed in Chapter 3. The traction and separation can be decomposed into its normal and shear components as

$$\bar{\sigma}_n = \bar{\sigma} \cos \theta, \bar{\sigma}_t = \bar{\sigma} \sin \theta, \quad (4.23)$$

$$\bar{\delta}_n = \bar{\delta} \cos \theta, \bar{\delta}_t = \bar{\delta} \sin \theta. \quad (4.24)$$

Integrating the traction-separation relation, the normal and shear components of the toughness are related to the toughness of the chain through

$$\bar{\Gamma}_n = \bar{\Gamma} \cos^2 \theta, \bar{\Gamma}_t = \bar{\Gamma} \sin^2 \theta. \quad (4.25)$$

Following this idea, the rate effect is incorporated through the bond rupture kinetics and both interfacial toughness and strength increase with increasing separation rates (Fig. 3.8). However, this simple extension leads to two consequences that do not fit with the experiments. First, the initial stiffness in the normal and tangential directions are the same as the initial stiffness of the chain. In addition, the damage parameter of the chain also determines the damage in its components, meaning the damage processes in the normal and shear interactions are always synchronized, which was not the case in Figures 4.17-18.

Finally, the total toughness is independent of the mode angle as implied by Eq. (4.25), which apparently contradicts the conclusions in Section 4.3.4. Therefore, further detailed analyses are required to better understand and simulate the mixed-mode rate-dependent interfacial fracture.

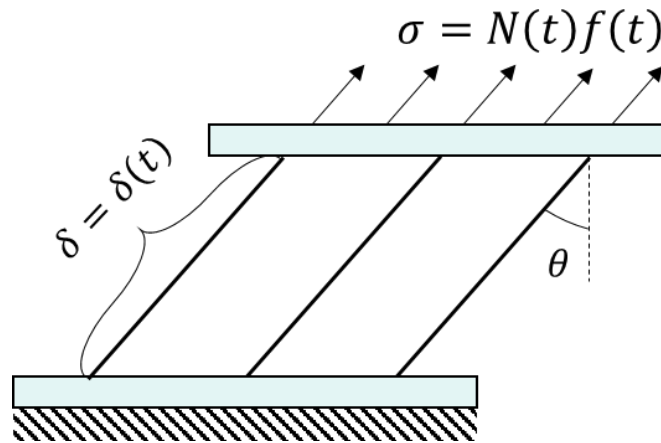


Figure 4.19 Schematic of chains being stretched with an angle θ .

4.4 Summary

This chapter presents a novel design for a dual-actuator loading device and its application in characterizing the rate dependent fracture for a silicon/epoxy interface under mixed mode loading conditions. The rate effect was examined by controlling the global displacement rate at the loading end. Different fracture mode conditions were achieved by varying the displacement ratio between the upper and lower beams. The mode angle at the crack tip was related to the applied displacement ratio by two sets of analyses: simple beam theory (epoxy ignored) and LEFM (epoxy considered). They are differed by a shift of $\sim 13^\circ$, with LEFM predicting a higher mode mix. Following from the decoupled beam interaction analysis, the balance condition was naturally satisfied via the symmetry of the specimen configuration (silicon/epoxy/silicon), thus enabling the decoupling of the normal and shear interactions. The interfacial properties (crack tip displacements, J-integrals and strengths)

were determined by a direct method using only far-field measurements, including the load point forces, displacements and rotations. The latter two were obtained by exploiting DIC to achieve better resolution. The beam on elastic foundation analysis was extended to incorporate shear interactions, and then was used to estimate the interfacial stiffness and crack length.

The toughness, interfacial strength and interaction range generally increased with increases in the separation rates. The exception was the interfacial stiffness, which was believed to be rate independent for any given mode angle. However, both normal and tangential stiffness did increase with increasing mode angle. This stiffening behavior may indicate that different interaction mechanisms are at play in a transition from mode I to mode II fracture. The rate dependence of the initiation toughness followed power law. A constant exponent was found in fitting the normal component of the initiation toughness, while only upper and lower bounds were available in the total toughness and its shear component. The local mode angle at the crack tip increased as the cohesive zone developed.

Both local separation rate and mode angle vary with crack length, which leads to the variation of interfacial properties as cohesive zone develops. Beam on elastic analysis were successfully used to estimate the normal and tangential rate at the current crack tip, which exhibited a decrease in the normal rate and an increase in the tangential rate as cohesive zone develops. This may explain the observed contrasting behavior of the J-integral components as the total reached steady state. As a result, the mode angle increases with crack extension, which was confirmed by two different definitions (crack tip displacements and J-integrals). The mode angle defined by J-integrals was well bracketed between the LEFM (upper bound) and simple beam theory (lower bound). On the other

hand, the definition by crack tip displacements coincided only at the initial crack tip, and then grew faster and exceeds the LEFM estimation.

The direct extraction is based on the assumption that traction-separation relations are uniform across the interface, which is not the case for the rate dependent fracture as the local rate is constantly evolving with crack extension. Nonetheless, the extraction is still valid at the initial crack tip and this has been validated via a finite element implementation with the traction-separation relation extracted at the initial crack tip. To better simulate rate dependent fracture under mixed mode loading conditions, further study is needed in developing an intrinsically rate dependent cohesive zone model.

Chapter 5 Conclusions and Future Work

This dissertation addresses the rate dependent fracture of a silicon/epoxy interface. The bulk epoxy was characterized under uniaxial tension and simple shear, which suggested that it was behaving as a glassy polymer within the range of the separation rates considered in this work. Therefore, the observed rate dependence was attributed to the silicon/epoxy interface [40, 109, 133, 134].

In Chapter 2, mode I rate dependent interfacial fracture was presented by DCB experiments conducted under ramp displacement control at the loading end. Given the force and displacement measurements, three methods were explored for analyzing the data. First, a beam on elastic foundation (BEF) analysis was used to extract the interfacial stiffness and estimate crack lengths and crack tip separation rates, as well as the J-integral under nominally mode I conditions. Second, an iterative approach [55] was adopted to extract the interfacial traction-separation relations. A bilinear form was assumed for the traction-separation relation, so that linear softening described the development of damage as the cohesive zone developed. There are three characteristic parameters in a bilinear traction-separation relation: initial stiffness, strength and toughness. The stiffness was chosen from the BEF analysis, while the latter two were obtained via numerical simulations and iteration with the load-displacement response as the metric for successful parameter selection. The interfacial properties obtained by first two methods exhibited similar rate dependence: both the interfacial strength and toughness increased with increasing crack tip separation rates. Motivated by this observation, a third approach, based on bond rupture kinetics, was developed to model the observed rate dependent fracture in a bottom-up manner. A layer of molecular bonds at the interface was taken as the link between the silicon and epoxy surfaces. The interfacial stiffness obtained from the BEF analysis was

adopted to describe the elastic deformation of the interfacial bonds. Instead of setting a maximum traction or a critical separation, the damage followed from a thermally activated bond rupture process, where the level of damage was evaluated by the survival probability in a statistical context [114, 119]. The survival probability explicitly depends on the energy barrier. In this portion of work, we assumed the energy barrier linearly decreased with increasing applied tractions [116, 117]. The interfacial bonds were linked to the interfacial TSR and naturally fits with the cohesive zone model. By implementing the rate dependent cohesive zone model in a finite difference framework (Appendix B), we were able to simulate the DCB experiments. With four parameters, close agreements were achieved between the numerical simulations and direct measurements, although one of the parameters, the critical stress, had to be adjusted at different crack tip separation rates.

Continuing the effort in the development of a mechanism-based, rate dependent model, a multiscale framework was proposed in Chapter 3, consisting of four levels: bond level, chain level, chain breaking kinetics and interface level. For the bond level, a Lennard-Jones potential energy function was adopted to define the bond energetics. At the chain level, the configurational entropy of a chain was described by the freely joined chain (FJC) theory. The underlying assumption in the FJC theory that the bonds of a chain are regarded as rigid links that results in an infinitely large stiffness when the chain approaches the fully straightened configuration, which conflicts with the bond energetics. To address this issue, a modified FJC model [123] was adopted to incorporate both chain entropy and bond energetics by allowing bond deformation while stretching a chain. As a result, the total free energy depends on both chain stretch and bond stretch. For a given chain stretch, the bond stretch can be determined through a minimization of the total free energy. Specifically for the LJ bond energy function, there exists a critical chain stretch, above which no equilibrium states can be found. The critical chain stretch may not be reached practically,

because damage can be accumulated following the bond rupture kinetics while the chain is stretched. Instead of relying on a linearized model (Chapter 2), we defined the energy barrier based on the Gibbs free energy, so that the energy barrier following this definition nonlinearly decreases with increasing applied force. Finally at the specimen level, a statistically distributed chain length was considered and the normal distribution was used in this work. To compare with the experiments, the model was implemented as a user-defined interface (Appendix C, D) in ABAQUS and then used to simulate the rate-dependent fracture of a silicon/epoxy interface in the mode I fracture experiments. Once the model parameters had been extracted from selected experiments, the numerical simulations show good agreements with the direct measurements over all separation rates.

In Chapter 4, we presented the design and related analyses for a dual-actuator loading device, which was used to characterize the rate dependent fracture of silicon/epoxy interface under mixed mode loading conditions. Direct measurements, including forces, displacements and rotations, were recorded at the loading end with the latter two measured by digital image correlation. For specimens with material and geometry symmetries, the decoupled beam analysis [56, 146] was exploited to extract the crack tip traction-separation relations. The results indicate the interface was toughened in both the normal and shear directions as the separation rates were increased. After reaching the initiation toughness, the crack grows and the local separation rate varies with crack extension. In this work, the crack length and local separation rates were estimated by a BEF analysis. Generally in the mixed-mode loading cases, although the global separation rate was held constant in the normal direction, the global tangential separation rate initially remained constant and then increased as the crack grew. As a result, the local separation rate decreased in the normal direction while it increased in the tangential direction. The trend was consistent with the observed relations of the normal and shear components of J-integrals with respect to the

crack extension. As a consequence, the mode angle also increased from the initial mode mix towards mode II as the crack propagated. The nominal mode I loading (symmetric opening) was an exception, where the mode angle remained nominally mode I and the shear components of local separation rate and J-integrals were negligible compared to normal components. In the end, we validated the analyses by implementing the extracted crack tip traction-separation relations via a user-defined interface in ABAQUS. The initially close agreement justified the use of decoupled beam analysis and BEF analysis at the initial crack tip that were used in the extraction of the traction-separation relations. The subsequent deviation suggests a requirement for traction-separation relations that are dependent on the local separation rate in order to better simulate the mixed mode interfacial fracture that was observed here.

Finally, in order to provide some perspective on this work, the following suggestions are made for future work:

- The development of a rate dependent cohesive zone model that is capable of simulating the observed characteristics of fracture under mixed mode conditions. The one presented in Chapter 2 works well for mode I conditions, however, problems arise if it is applied to the mixed mode fracture without further modifications. Nonetheless, the idea of a multiscale framework and the thermally activated bond rupture kinetics may be still followed in the mixed mode case.
- The design of a fracture experiment that provides control of the local separation rate. The experiments conducted here followed ramps in normal displacement at the loading end, which, as discussed in Chapter 4, caused variations in the local normal and tangential separation rates. It would be interesting to see if steady state crack propagation can be achieved with constant local separation rates. This may

be feasible (at least in the normal direction) by adding a feedback loop in the control system so that the global displacement rate can be updated in real time in order to maintain a constant local separation rate based on the BEF analysis.

- Another aspect of the previous point is that non proportional loading paths can be followed in order to examine the development of damage as the cohesive zone develops and the crack grows.
- The characterization of the interfacial fracture at different temperatures. The change of temperature can cause the change in the mechanical behavior of the epoxy due to viscoelasticity. It may also affect the interfacial properties. The multiscale chain breaking model naturally presents a temperature dependence and experiment with temperature control may be considered to examine the model.

Appendix A: Beam on elastic foundation model

In line with Gowrishankar, et al. [55] and Wu, et al. [58], we extend the capability of the beam on elastic foundation model by considering both the normal and shear interactions at the interface. Two sets of linear springs link the upper and lower beams with independent spring constants: normal stiffness K_n and shear stiffness K_t . The tractions at the interface are then linearly related to the respective separations through

$$\sigma_n = K_n \delta_n, \quad (\text{A.1a})$$

$$\sigma_t = K_t \delta_t. \quad (\text{A.1b})$$

Now consider an infinitesimal section (Fig. A1) of the bonded part of the specimen ($x < 0$). The displacement fields in top and bottom adherends are approximately

$$u_1(x, z_1) = u_{10} - z_1 \frac{dw_1}{dx}, w_1 = w_1(x, 0), \quad (\text{A.2a})$$

$$u_2(x, z_2) = u_{20} - z_2 \frac{dw_2}{dx}, w_2 = w_2(x, 0), \quad (\text{A.2b})$$

where u_{i0} ($i = 1, 2$) are the axial displacements at the neutral axis of each adherend, and w_i ($i = 1, 2$) is the lateral deflection of each adherend. As a result, the relative normal and shear separations at the interface are,

$$\delta_n = w_1 - w_2, \quad (\text{A.3a})$$

$$\delta_t = u_{1b} - u_{2t}, \quad (\text{A.3b})$$

respectively, with

$$u_{1b} = u_{10} + \frac{h_1}{2} \frac{dw_1}{dx}, \quad (\text{A.4a})$$

$$u_{2t} = u_{20} - \frac{h_2}{2} \frac{dw_2}{dx}. \quad (\text{A.4b})$$

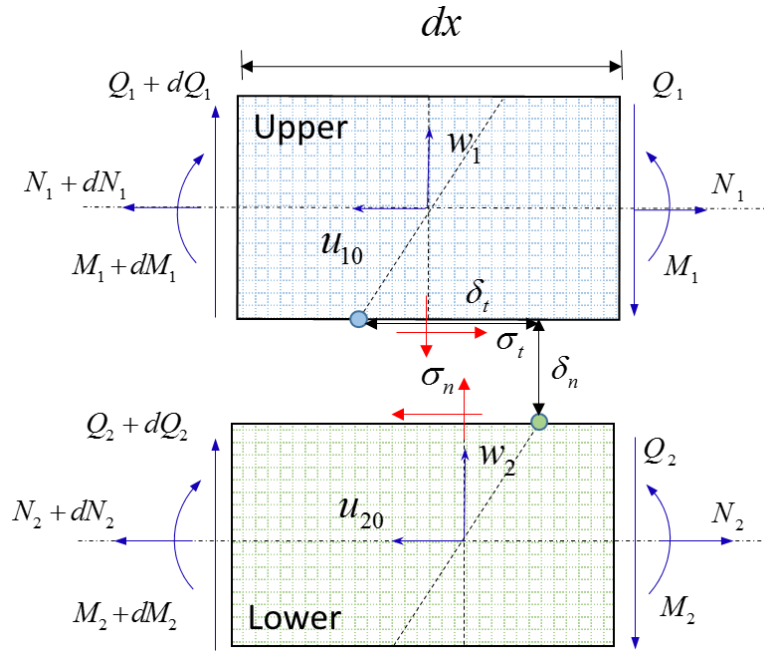


Figure A1 Infinitesimal beam elements and internal forces

The free body diagram yields the following equilibrium equations:

$$\sigma_n = -\frac{dQ_1}{dx} = \frac{dQ_2}{dx}, \quad (\text{A.5a})$$

$$\sigma_t = \frac{dN_1}{dx} = -\frac{dN_2}{dx}, \quad (\text{A.5b})$$

$$\frac{dM_1}{dx} = Q_1 + \sigma_t \frac{h_1}{2}, \quad (\text{A.5c})$$

$$\frac{dM_2}{dx} = Q_2 + \sigma_t \frac{h_2}{2}. \quad (\text{A.5d})$$

Simple beam theory yields the following kinetic equations for the upper and lower beams ($i = 1, 2$):

$$N_i = A_i \frac{du_{i0}}{dx}, \quad (\text{A.6a})$$

$$M_i = D_i \frac{d^2 w_i}{dx^2}, \quad (\text{A.6b})$$

where $A_i = \bar{E}_i h_i$ is the axial stiffness and $D_i = \bar{E}_i h_i^3 / 12$ is the bending stiffness of the beams.

In the normal direction, we can take the second derivative of (A.3a) and use the second equation in (A.6b) to obtain

$$\delta_n^{(2)} = \frac{d^2 w_1}{dx^2} - \frac{d^2 w_2}{dx^2} = \frac{M_1}{D_1} - \frac{M_2}{D_2}. \quad (\text{A.7})$$

We can further take the third and the fourth derivatives of (A.7) and use the equations in (A.5) to obtain

$$\delta_n^{(3)} = \frac{1}{D_1} \left(Q_1 + \sigma_t \frac{h_1}{2} \right) - \frac{1}{D_2} \left(Q_2 + \sigma_t \frac{h_2}{2} \right), \quad (\text{A.8a})$$

$$\delta_n^{(4)} = - \left(\frac{1}{D_1} + \frac{1}{D_2} \right) \sigma_n + \left(\frac{h_1}{2D_1} - \frac{h_2}{2D_2} \right) \frac{d\sigma_t}{dx}. \quad (\text{A.8b})$$

Apparently, the normal and shear tractions are coupled in (A.8b). We adopt the balance condition as stated in Ouyang and Li [146] and Wu, et al. [56],

$$h_1/D_1 = h_2/D_2, \quad (\text{A.9})$$

and obtain the following governing equation in the normal direction,

$$\hat{D} \delta_n^{(4)} + \sigma_n = 0, \quad (\text{A.10})$$

with $\hat{D} = \left(\frac{1}{D_1} + \frac{1}{D_2} \right)^{-1}$.

Similarly, in the shear direction, we first combine the kinematics (A.3b, A.4b) and (A.6a), which yields the following relation,

$$\delta_t^{(1)} = \frac{N_1}{A_1} - \frac{N_2}{A_2} + \left(\frac{h_1}{2} \frac{M_1}{D_1} + \frac{h_2}{2} \frac{M_2}{D_2} \right). \quad (\text{A.11})$$

Taking derivative of (A.11) and combining the equilibrium equations in (A.5), we obtain the following,

$$\delta_t^{(2)} = \left(\frac{h_1}{2D_1} Q_1 + \frac{h_2}{2D_2} Q_2 \right) + \left(\frac{1}{A_1} + \frac{1}{A_1} + \frac{h_1^2}{4D_1} + \frac{h_2^2}{4D_2} \right) \sigma_t. \quad (\text{A.12})$$

Note that the shear forces are related to the normal traction in (A.5a). Thus we can integrate the normal traction to obtain the shear forces as,

$$Q_1(x) = -P_1 - \int_0^x \sigma_n dx, \quad (\text{A.13a})$$

$$Q_2(x) = -P_2 + \int_0^x \sigma_n dx. \quad (\text{A.13b})$$

Combining (A.12) and (A.13), we obtain

$$\delta_t^{(2)} + \left(\frac{P_1 h_1}{2D_1} + \frac{P_2 h_2}{2D_2} \right) - \left(\frac{h_1}{2D_1} - \frac{h_2}{2D_2} \right) \int_0^x \sigma_n dx = \left(\frac{1}{A_1} + \frac{1}{A_1} + \frac{h_1^2}{4D_1} + \frac{h_2^2}{4D_2} \right) \sigma_t. \quad (\text{A.14})$$

Again, we enforce the balance condition (A.9) and obtain the governing equation in the shear direction as

$$\hat{A} \delta_t^{(2)} - \sigma_t = -\bar{P} \frac{\hat{A} h_1}{2D_1}. \quad (\text{A.15})$$

with $\bar{P} = P_1 + P_2$ and $\hat{A} = \left(\frac{1}{A_1} + \frac{1}{A_1} + \frac{h_1^2}{4D_1} + \frac{h_2^2}{4D_2} \right)^{-1}$.

For $0 < x < a$ (Fig. 4.2), the interface is traction-free and hence $\sigma_n = \sigma_t = 0$. For $x \geq 0$, we follow the elastic foundation assumption so that Eq. (A.1) are used to relate the tractions to the separations at the interface. The governing equation in the normal direction (A.10) has been solved in detail in Gowrishankar, et al. [55] and a relation between the force difference ($\tilde{P} = P_1 - P_2$) and the normal separation at the loading point ($\tilde{\Delta} = \Delta_1 - \Delta_2$) was obtained as

$$\tilde{P} = \frac{6\hat{D}}{a^3} \left(1 + \frac{3}{\lambda_n a} + \frac{3}{(\lambda_n a)^2} + \frac{3}{2(\lambda_n a)^3} \right)^{-1} \tilde{\Delta}, \quad (\text{A.16})$$

with $\lambda_n = \left(\frac{6K_n}{Eh_1^3}\right)^{1/4}$.

The governing equation (A.15) in shear direction is solved in a similar manner. Subject to the boundary conditions: $\delta_t(x = a) = \tilde{U}$ and $\delta_t'(x = a) = 0$, we obtain the tangential separation for the traction-free region ($0 < x < a$) as

$$\delta_t(x) = \tilde{U} - \frac{\bar{P}h_1a^2}{4D_1}\left(1 - \frac{x}{a}\right)^2, \quad (\text{A.17})$$

where $\tilde{U} = U_1 - U_2$ is the tangential separation at the loading point. For $x < 0$, the shear traction is related to the tangential separation through (A.1b). Equation (A.15) is then solved by enforcing the continuity condition: $\delta_t(x = 0^-) = \delta_t(x = 0^+)$ and $\delta_t'(x = 0^-) = \delta_t'(x = 0^+)$, which leads to

$$\bar{P} = \frac{2D_1}{h_1} \left(\frac{a^2}{2} + \frac{a}{\lambda_t} \tanh(\lambda_t(L - a)) + \frac{1}{\lambda_t^2} \left(1 - \frac{1}{\cosh(\lambda_t(L - a))} \right) \right)^{-1} \tilde{U}, \quad (\text{A.18})$$

with $\lambda_t = \sqrt{\hat{A}^{-1}K_t}$. It should be noted that the kernel $\lambda_t(L - a)$ in (A.18) represents a ratio between the bonded length ($L - a$) and a length scale $\lambda_t^{-1} \sim \sqrt{h_e h_1 / (G_e / E_1)}$, given that the shear stiffness of the elastic foundation can be approximated by $K_t \sim G_e / h_e$. For the material system ($h_e \sim 0.04 \text{ mm}$, $h_1 = 1 \text{ mm}$, $G_e / E_1 = 1/130$ and $a_0 \sim 12 \text{ mm}$) in this study, the ratio is relatively large (~ 10), and hence the equation (A.18) can be simplified as

$$\bar{P} = \frac{2D_1}{h_1} \left(\frac{a^2}{2} + \frac{a}{\lambda_t} + \frac{1}{\lambda_t^2} \right)^{-1} \tilde{U}. \quad (\text{A.19})$$

Thus far, we obtain two equations (A.16) and (A.19) that establish the relations between the force (P_i) and displacement (Δ_i, U_i) measurements at the loading points. In this dissertation (Chapter 4), these relations are used for two purposes: (1) Extract the normal and tangential stiffness at the interface given the initial crack length (Fig. 4.6a); (2)

Estimate the crack length given the normal and tangential stiffness at the interface (Fig. 4.6c).

Appendix B: A finite difference implementation of bond rupture kinematics in a DCB specimen

Using the finite difference method, we discretize the normalized beam equation (2.20) as

$$\bar{\delta}_{k+2} - 4\bar{\delta}_{k+1} + 6\bar{\delta}_k - 4\bar{\delta}_{k-1} + \bar{\delta}_{k-2} = -4(\Delta\bar{x})^4(1 - D_k)\bar{\delta}_k \quad (\text{B.1})$$

where, $\Delta\bar{x} = (\bar{L} - \bar{a})/n$ and $0 \leq k \leq n$ (with node 0 at the crack tip and node n at the clamped end of the beam). To discretize the boundary conditions, three dummy nodes are used, $(\bar{\delta}_{-2}, \bar{\delta}_{-1})$ for the crack tip and $(\bar{\delta}_{n+1})$ for the clamped end. The continuity conditions at the crack tip ($\bar{x} = 0$) are discretized as:

$$\bar{\delta}_0 = \bar{\delta}^*,$$

$$\bar{\delta}_1 - \bar{\delta}_{-1} = -2\Delta\bar{x}\bar{\theta}^*,$$

$$\bar{\delta}_1 - 2\bar{\delta}_0 + \bar{\delta}_{-1} = \frac{3(\Delta\bar{x})^2}{\bar{a}^2} \left(2\bar{t} - \bar{\delta}_0 + \bar{a} \frac{\bar{\delta}_1 - \bar{\delta}_{-1}}{2\Delta\bar{x}} \right),$$

$$\bar{\delta}_2 - 2\bar{\delta}_1 + 2\bar{\delta}_{-1} - \bar{\delta}_{-2} = \frac{6(\Delta\bar{x})^3}{\bar{a}^3} \left(2\bar{t} - \bar{\delta}_0 + \bar{a} \frac{\bar{\delta}_1 - \bar{\delta}_{-1}}{2\Delta\bar{x}} \right), \quad (\text{B.2})$$

and the clamped boundary conditions at $\bar{x} = \bar{L} - \bar{a}$ are:

$$\bar{\delta}_n = 0,$$

$$\bar{\delta}_{n+1} - \bar{\delta}_{n-1} = 0. \quad (\text{B.3})$$

The second equation in (B.3) indicates that $\bar{\delta}_{n+1} = \bar{\delta}_{n-1}$, and thus for $k = n - 1$ Eq. (B.1) becomes:

$$7\bar{\delta}_{n-1} - 4\bar{\delta}_{n-2} + \bar{\delta}_{n-3} = -4(\Delta\bar{x})^4(1 - D_{n-1})\bar{\delta}_{n-1}. \quad (\text{B.4})$$

The corresponding rate equations can be obtained by taking time derivatives of (B.1), (B.2) and (B.4) as:

$$\begin{aligned}
\dot{\delta}_{k+2} - 4\dot{\delta}_{k+1} + 6\dot{\delta}_k - 4\dot{\delta}_{k-1} + \dot{\delta}_{k-2} &= -4(\Delta\bar{x})^4 \left[(1 - D_k)\dot{\delta}_k - \dot{D}_k\bar{\delta}_k \right], \\
\left(1 - \frac{3\Delta\bar{x}}{2\bar{a}}\right)\dot{\delta}_1 - 2\dot{\delta}_0 \left(1 - \frac{3(\Delta\bar{x})^2}{2\bar{a}^2}\right) + \left(1 + \frac{3\Delta\bar{x}}{2\bar{a}}\right)\dot{\delta}_{-1} &= \frac{6(\Delta\bar{x})^2}{\bar{a}^2}, \\
\dot{\delta}_2 - 2\dot{\delta}_1 \left(1 + \frac{3(\Delta\bar{x})^2}{2\bar{a}^2}\right) + \frac{6(\Delta\bar{x})^3}{\bar{a}^3}\dot{\delta}_0 + 2\dot{\delta}_{-1} \left(1 + \frac{3(\Delta\bar{x})^2}{2\bar{a}^2}\right) - \dot{\delta}_{-2} &= \frac{12(\Delta\bar{x})^3}{\bar{a}^3}, \\
7\dot{\delta}_{n-1} - 4\dot{\delta}_{n-2} + \dot{\delta}_{n-3} &= -4(\Delta\bar{x})^4 \left[(1 - D_{n-1})\dot{\delta}_{n-1} - \dot{D}_{n-1}\bar{\delta}_{n-1} \right], \tag{B.5}
\end{aligned}$$

which consist of $n + 2$ equations ($k = 0, 1, \dots, n - 2$ in the first equation) and can be re-written in a matrix form as:

$$\mathbf{M}\dot{\boldsymbol{\delta}} = \mathbf{f} \tag{B.6}$$

where $\dot{\boldsymbol{\delta}} = (\dot{\delta}_{-2}, \dot{\delta}_{-1}, \dot{\delta}_0, \dots, \dot{\delta}_{n-1})^T$ and

$$\mathbf{M} = \begin{bmatrix} -1 & 2\left(1 + \frac{3(\Delta\bar{x})^2}{2\bar{a}^2}\right) & \frac{6(\Delta\bar{x})^3}{\bar{a}^3} & -2\left(1 + \frac{3(\Delta\bar{x})^2}{2\bar{a}^2}\right) & 1 & \dots & 0 & 0 \\ 0 & \left(1 + \frac{3\Delta\bar{x}}{2\bar{a}}\right) & -2\left(1 - \frac{3(\Delta\bar{x})^2}{2\bar{a}^2}\right) & \left(1 - \frac{3\Delta\bar{x}}{2\bar{a}}\right) & 0 & \dots & 0 & 0 \\ 1 & -4 & 6 + 4(\Delta\bar{x})^4(1 - D_0) & -4 & 1 & \dots & 0 & 0 \\ \vdots & \vdots & \vdots & \vdots & \vdots & \ddots & \vdots & \vdots \\ 0 & 0 & 0 & 0 & 0 & \dots & -4 & 1 \\ 0 & 0 & 0 & 0 & 0 & \dots & 6 + 4(\Delta\bar{x})^4(1 - D_{n-2}) & -4 \\ 0 & 0 & 0 & 0 & 0 & \dots & -4 & 7 + 4(\Delta\bar{x})^4(1 - D_{n-1}) \end{bmatrix}$$

$$\mathbf{f} = \begin{pmatrix} \frac{12(\Delta\bar{x})^3}{\bar{a}^3} \\ \frac{6(\Delta\bar{x})^2}{\bar{a}^2} \\ 4(\Delta\bar{x})^4\dot{D}_0\bar{\delta}_0 \\ \vdots \\ 4(\Delta\bar{x})^4\dot{D}_{n-1}\bar{\delta}_{n-1} \end{pmatrix} \tag{B.7}$$

By Eq. (2.24), the rate of damage evolution at each node is:

$$\dot{D}_k = \frac{t_1}{t_0} (1 - D_k) \exp\left(-\frac{\varepsilon_0}{k_{BT}} (1 - \bar{\delta}_k)\right). \tag{B.8}$$

Thus, given $\bar{\delta}$ and \mathbf{D} at all nodes, we calculate the damage rate $\dot{\mathbf{D}}$ by (B.8) and then the separation rate $\dot{\bar{\delta}}$ by (B.6). The separation and damage are then updated for the next time step as: $D_k^{(i+1)} = D_k^{(i)} + \dot{D}_k^{(i)} \cdot \Delta \bar{t}$ and $\bar{\delta}_k^{(i+1)} = \bar{\delta}_k^{(i)} + \dot{\bar{\delta}}_k^{(i)} \cdot \Delta \bar{t}$. For numerical stability and accuracy, the time step was chosen as: $\Delta \bar{t} = 10^{-3} / \max(\dot{D}_k, \dot{\bar{\delta}}_k)$, and a total number of 1001 nodes ($n = 1000$) were used to discretize the beam from $\bar{x} = 0$ to $\bar{x} = \bar{L} - \bar{a}$.

At each time step, the normalized CTOD is $\bar{\delta}^* = \bar{\delta}_0$, and the normalized CTOA is $\bar{\theta}^* = -(\bar{\delta}_1 - \bar{\delta}_{-1}) / (2\Delta \bar{x})$. Then, by Eq. (2.22), the normalized force at the loading point ($\bar{x} = -\bar{a}$) is:

$$\bar{P} = \bar{t} - \bar{\delta}^* + \frac{\bar{a}}{2\Delta \bar{x}} (\bar{\delta}_1 - \bar{\delta}_{-1}), \quad (\text{B.9})$$

where $\bar{P} = \frac{2a^3}{3\kappa l_0} P$.

Appendix C: A finite element implementation of the multiscale rate-dependent cohesive zone model

A two-dimensional, tri-layer finite element model was constructed in ABAQUS in order to simulate the mode I experiments. Both silicon beams and epoxy layer were modeled by plane strain quadrilateral elements (CPE8), with linearly elastic properties ($E = 130$ GPa, $\nu = 0.22$ for silicon and $E_e = 2.4$ GPa, $\nu = 0.4$ for the epoxy). The epoxy layer was tied to the bottom silicon beam, while the interface between the epoxy and the upper silicon beam was modeled by a user-defined surface-to-surface interaction with a master (silicon) and a slave (epoxy). The epoxy layer was densely meshed (at least 10 elements in the thickness direction) to avoid being penetrated by the master surface. In this work, the rate-dependent cohesive zone model was implemented as a user-defined subroutine (Appendix D) to describe the interactions between the master-slave surface nodes. Unlike a typical cohesive zone model, the present model does not prescribe a specific form of the traction-separation relation. Instead, the traction is calculated following the history of separation and damage evolution.

Given the relative displacements between the surface nodes, the tractions and the tangent stiffness are calculated by the user subroutine. In addition, the damage parameters must be updated based on the rate equation, Eq. (5.2). The implementation procedure is summarized as follows:

- 1) With the input separation δ at the current step, the chain stretch $\lambda = \delta/(nr_0)$ is obtained for each chain length (n). Then, the corresponding bond stretch (λ_b) and the end force f are calculated by solving Eq. (3.9) and Eq. (3.10), respectively.
- 2) Next, the energy barrier for chain breaking is numerically solved based on (3.13) and Eq. (3.11). Alternatively, one can use the approximate formulation as in Eq. (3.14).

- 3) The rate of the change of the damage parameter for the current chain (D_n) is then available through Eq. (3.22). We can update the current damage parameter based on the damage rate and the previous value.
- 4) For statistically distributed chain length, steps 1-3 are repeated for chains with different chain lengths. The chain force (same as bond force) and damage parameter for each chain length are needed for calculating the stress at the current node by Eq. (3.23). The tangent stiffness $\partial\sigma/\partial\delta$ can be obtained by numerical differentiation, with the tractions and separations of the current and previous steps.

To reduce the cost of numerical calculations, especially the one induced by solving the inverse Langevin function, we can pre-solve the Eq. (3.9) and Eq. (3.10) for a range of chain stretches with relatively fine increments (e.g., $\delta\lambda/\lambda = 10^{-5}$), and save the results to a file. Then we can call the file in order to obtain the bond stretch and bond force based on the current chain stretch through interpolation of the nearest upper and lower bounds. Given that both bond stretch and bond force increase monotonically with the chain stretch before the maximum bond force (above which the chain is instantaneously broken), the binary search algorithm can be applied to find the nearest bounds with significantly less time.

This implementation may require large memory, depending on the selected distribution. For chains with different chain lengths, we need to (at least) store the damage parameters (D_n) as state variables (STATEV) for each chain length at the current step and use them in the next subroutine call. When both average chain length (n_0) and chain length deviation (χ) are relatively large, more state variables are required by the subroutine and we may need to increase the memory allocation limit if needed.

Appendix D: User-defined interface subroutine (UINTER)

```
subroutine uinter(stress, ddsddr, amki, amski, flux, ddfddt, ddsddt,
1   ddfddr, statev, sed, sfd, spd, svd, scd, pnewdt, rdisp, drdisp,
2   temp, dtemp, predef, dpred, time, dtime, freqr, ciname, slname,
3   msname, props, coords, aLocalDir, drot, area, chrLength, node, ndir,
4   nstatv, npred, nprops, mcrd, kstep, kinc, kit, linper, lOpenClose,
5   lState, lSdi, lPrint)

include 'aba_param.inc'

dimension stress(ndir), ddsddr(ndir, ndir), flux(2), ddfddt(2, 2),
$   ddsddt(ndir, 2), ddfddr(2, ndir), statev(nstatv), rdisp(ndir),
$   drdisp(ndir), temp(2), dtemp(2), predef(2, npred), dpred(2, npred),
$   time(2), props(nprops), coords(mcrd), aLocalDir(mcrd, mcrd),
$   drot(2, 2), amki(ndir, ndir), amski(ndir, ndir)

character*80 ciname, slname, msname

parameter(TOLER = 1.d-5, ZERO = 0.d0, ONE = 1.d0, TWO = 2.d0,
$   HALF = ONE/TWO, T0 = 1d-13, BOLT = 1.38d-23)

real(kind=8) delta_n, delta_t, delta, sigma_0, K_0, rho,
$   kn, kt, tn, tt, dam, tbar,
$   frac, Eb, lambda, lambda_b, f_chain

integer(kind=8) ch_max, ch_min, n_min, n_max, idx, n, curr_n

real(kind=8), dimension(10000) :: lmc, lmbc, fc, barr
real(kind=8), dimension(10000) :: damage_array
CHARACTER(*), PARAMETER :: fileplace = "/PATH/TO/FILE"

C   Read the MAP
open(unit=2, file=fileplace, status='old', action='read')
do i = 1, len(file)
    read(2, *) lmc(i), lmbc(i), fc(i), barr(i)
end do
close(2)

C   Material properties
ch_den = props(1)
bd_len = props(2)
dist_m = props(3)
dist_k = props(4)
temp   = props(5)

C   Local variables
ch_max = dist_m + 4 * dist_k
ch_min = dist_m - 4 * dist_k
n_max  = ch_max - ch_min + 1
n_min  = 1
delta_n = -rdisp(1)
```

```

delta_t = rdisp(2)
tbar    = ZERO
sigma_0 = BOLT * temp * ch_den / bd_len
K_0     = 3 * BOLT * temp * ch_den / (bd_len ** 2)
flag    = statev(n_max + 1)

do n = n_min, n_max
  damage_array(n) = statev(n)
end do

C Damage completed?
if (flag == 1) then
  kn = 0
  kt = 0
  tn = 0
  tt = 0
else
  delta = sqrt(max(ZERO, un) ** 2 + ut ** 2)
  do n = n_min, n_max
    dam = damage_array(n)
    curr_n = n + ch_min - 1
    if (dam < ONE .and. abs(dam - ONE) > TOLER) then
      lambda = del / curr_n / bd_len

C Search the index corresponding to the current chain stretch
      call locate(lmc, lm, len, idx)
      f_chain = fc(idx)
      Eb = barr(idx)

C Interpolation
      if (idx < len) then
        frac = (lm - lmc(idx)) / (lmc(idx + 1) - lmc(idx))
        f_chain = f_chain + (fc(idx + 1) - fc(idx)) * frac
        Eb = Eb + (barr(idx + 1) - barr(idx)) * frac

C If index out of bound, chain broke, set energy barrier -1
      else
        Eb = -1
      end if

C Update damage for current chain length
      if (exp(Eb) < curr_n .or. Eb == -1) then
        dam = 1
      else
        dam = dam + curr_n * (1 - dam) * exp(-Eb) * dt / T0
      end if
      if (dam > ONE .or. abs(ONE - dam) < TOLER) then
        dam = ONE
      end if
    end if

C chain length density
    call norm_pdf(curr_n, dist_m, dist_k, rho)

C Update stress for current chain length
    tbar = tbar + f_chain * rho * (ONE - dam)

C Update damage for current chain length
  end do

```

```

        damage_array(n) = dam
    end do
end if
C Check if damage completed
do n = n_min, n_max
    if (abs(damage_array(n) - ONE) > TOLER) then
        exit
    end if
    if (n .eq. n_max) then
        flag = 1
    end if
end do

C Update stress and stiffness
if (flag .ne. 1) then
    if (un .le. 0) then
        kn = ONE
        tn = kn * un
        tt = tbar
    else
        tn = tbar * un / delta
        tt = tbar * ut / delta
        kn = (tn - statev(n_max + 3)) / drdisp(1)
    end if
    kt = (tt - state(n_max + 5)) / drdisp(2)
end if

C Cache all damage states
do n = n_min, n_max
    statev(n) = damage_array(n)
end do

C Return stiffness
ddsddr(1,1) = kn * K_0
ddsddr(2,2) = kt * K_0
C Return stress
stress(1) = -tn * sigma_0
stress(2) = tt * sigma_0
C Update state variables
statev(1 + n_max) = flag
statev(2 + n_max) = un
statev(3 + n_max) = tn
statev(4 + n_max) = ut
statev(5 + n_max) = tt
return
end

C Locate the chain force based on given chain stretch
subroutine locate(lmc, lm, len, idx)
real(kind=8) lm
integer(kind=8) lo, hi, len, idx, mid, sum
real(kind=8), dimension(len) :: lmc
lo = 1

```

```

hi = len
do while (lo + 1 < hi)
  sum = lo + hi
  if (mod(sum, 2) == 0) then
    mid = sum / 2
  else
    mid = (sum - 1) / 2
  end if
  if (lmc(mid) > lm) then
    hi = mid
  else if (lmc(mid) < lm) then
    lo = mid
  else
    lo = mid
  exit
end if
end do
idx = lo
return
end

```

C Normal distribution

```

subroutine norm_pdf(n0, mu, ka, rho)
integer(kind=8) n0, mu, ka
real(kind=8) rho, tmp
tmp = -real((n0 - mu)**2) / 2 / real(ka**2)
rho = exp(tmp) / sqrt(2*3.1415927) / ka
return
end

```

References

- [1] X. Feng, M. A. Meitl, A. M. Bowen, Y. Huang, R. G. Nuzzo, and J. A. Rogers, "Competing fracture in kinetically controlled transfer printing," *Langmuir*, vol. 23, pp. 12555-12560, 2007/12/01 2007.
- [2] S. R. Na, J. W. Suk, L. Tao, D. Akinwande, R. S. Ruoff, R. Huang, *et al.*, "Selective Mechanical Transfer of Graphene from Seed Copper Foil Using Rate Effects," *ACS Nano*, vol. 9, pp. 1325-1335, 2015/02/24 2015.
- [3] T. Yoon, W. C. Shin, T. Y. Kim, J. H. Mun, T.-S. Kim, and B. J. Cho, "Direct measurement of adhesion energy of monolayer graphene as-grown on copper and its application to renewable transfer process," *Nano letters*, vol. 12, pp. 1448-1452, 2012.
- [4] W. G. Knauss, "Fracture mechanics and time dependent strength of adhesive joints," *J. Comp. Mat.*, vol. 5, pp. 39-61, 1975.
- [5] H. Cheng, J. Wu, Q. Yu, H.-J. Kim-Lee, A. Carlson, K. T. Turner, *et al.*, "An analytical model for shear-enhanced adhesiveless transfer printing," *Mechanics Research Communications*, vol. 43, pp. 46-49, 7// 2012.
- [6] D. P. Makhecha, R. K. Kapania, E. R. Johnson, D. A. Dillard, G. C. Jacob, and J. M. Starbuck, "Rate-Dependent Cohesive Zone Modeling of Unstable Crack Growth in an Epoxy Adhesive," *Mechanics of Advanced Materials and Structures*, vol. 16, pp. 12-19, 2009.
- [7] M. Williams, "The stresses around a fault or crack in dissimilar media," *Bulletin of the seismological society of America*, vol. 49, pp. 199-204, 1959.
- [8] J. R. Rice, "Elastic Fracture Mechanics Concepts for Interfacial Cracks," *J. Appl. Mech*, vol. 55, pp. 98-103, 1988.
- [9] J. W. Hutchinson and Z. Suo, "Mixed mode cracking in layered materials," *Advances in Applied mechanics*, vol. 29, pp. 63-199., 1992.
- [10] J. S. Wang and Z. Suo, "Experimental-determination of interfacial toughness curves using Brazil-nut-sandwiches," *Acta Metallurgica Et Materialia*, vol. 38, pp. 1279-1290, Jul 1990.
- [11] A. Evans, M. Rühle, B. Dalgleish, and P. Charalambides, "The fracture energy of bimaterial interfaces," *Metallurgical Transactions A*, vol. 21, pp. 2419-2429, 1990.
- [12] Y. S. Chai and K. M. Liechti, "Asymmetric shielding in interfacial fracture under in-plane shear," *Journal of Applied Mechanics*, vol. 59, pp. 295-304, 1992.
- [13] A. G. Evans and J. W. Hutchinson, "Effects of non-planarity on the mixed mode fracture resistance of bimaterial interfaces," *Acta Metall.*, vol. 37, pp. 909-916, 1989.
- [14] J. G. Swadener and K. M. Liechti, "Asymmetric shielding mechanisms in the mixed-mode fracture of a glass/epoxy interface," *Journal of Applied Mechanics*, vol. 65, pp. 25-29, Mar 1998.
- [15] J. P. Parmigiani and M. D. Thouless, "The effects of cohesive strength and toughness on mixed-mode delamination of beam-like geometries," *Engineering Fracture Mechanics*, vol. 74, pp. 2675-2699, 2007.

- [16] R. B. Sills and M. D. Thouless, "The effect of cohesive-law parameters on mixed-mode fracture," *Engineering Fracture Mechanics*, vol. 109, pp. 353-368, 2013/09/01/ 2013.
- [17] I. Mohammed and K. M. Liechti, "Cohesive zone modeling of crack nucleation at bimaterial corners," *Journal of the Mechanics and Physics of Solids*, vol. 48, pp. 735-764, Apr 2000.
- [18] D. S. Dugdale, "Yielding of steel sheets containing slits," *Journal of the Mechanics and Physics of Solids*, vol. 8, pp. 100-104, 1960/05/01/ 1960.
- [19] G. I. Barenblatt, "The Mathematical Theory of Equilibrium Cracks in Brittle Fracture," in *Advances in Applied Mechanics*. vol. 7, H. L. Dryden, T. von Kármán, G. Kuerti, F. H. van den Dungen, and L. Howarth, Eds., ed: Elsevier, 1962, pp. 55-129.
- [20] G. Sih and J. Rice, "The bending of plates of dissimilar materials with cracks," *Journal of Applied Mechanics*, vol. 31, pp. 477-482, 1964.
- [21] A. Needleman, "An analysis of tensile decohesion along an interface," *Journal of the Mechanics and Physics of Solids*, vol. 38, pp. 289-324, 1990.
- [22] X.-P. Xu and A. Needleman, "Numerical simulations of dynamic crack growth along an interface," *International journal of fracture*, vol. 74, pp. 289-324, 1996.
- [23] A. V. Mello and K. M. Liechti, "The effect of self-assembled monolayers on interfacial fracture," *Journal of Applied Mechanics*, vol. 73, pp. 860-870, 2006.
- [24] N. Valoroso and R. Fedele, "Characterization of a cohesive-zone model describing damage and de-cohesion at bonded interfaces. Sensitivity analysis and mode-I parameter identification," *International Journal of Solids and Structures*, vol. 47, pp. 1666-1677, 2010.
- [25] M. Samimi, J. Van Dommelen, and M. Geers, "A three-dimensional self-adaptive cohesive zone model for interfacial delamination," *Computer methods in applied mechanics and engineering*, vol. 200, pp. 3540-3553, 2011.
- [26] T. Ungsuwarungsri and W. G. Knauss, "The role of damage-softened material behavior in the fracture of composites and adhesives," *International Journal of Fracture*, vol. 35, pp. 221-241, 1987/11/01 1987.
- [27] B. F. Sorensen, "Cohesive law and notch sensitivity of adhesive joints," *Acta Materialia*, vol. 50, pp. 1053-1061, 2002.
- [28] S. Li, M. D. Thouless, A. M. Waas, J. A. Schroeder, and P. D. Zavattieri, "Use of mode-I cohesive-zone models to describe the fracture of an adhesively-bonded polymer-matrix composite," *Composites Science and Technology*, vol. 65, pp. 281-293, Feb 2005.
- [29] S. Li and M. D. Thouless, "Mixed-mode cohesive-zone models for fracture of an adhesively bonded polymer matrix composite," *Engineering Fracture Mechanics*, vol. 73, pp. 64-78, 2006.
- [30] B. F. Sorensen and P. Kirkegaard, "Determination of mixed mode cohesive laws," *Engineering Fracture Mechanics*, vol. 73, pp. 2642-2661, Nov 2006.
- [31] J. L. Högberg, B. F. Sorensen, and U. Stigh, "Constitutive behaviour of mixed mode loaded adhesive layer," *International Journal of Solids and Structures*, vol. 44, pp. 8335-8354, 2007.

- [32] R. Campilho, M. Banea, J. Neto, and L. Da Silva, "Modelling of single-lap joints using cohesive zone models: effect of the cohesive parameters on the output of the simulations," *The Journal of Adhesion*, vol. 88, pp. 513-533, 2012.
- [33] X. Li, R. Tao, M. Alfano, and G. Lubineau, "How variability in interfacial properties results in tougher bonded composite joints by triggering bridging," *International Journal of Solids and Structures*, 2019/11/27/ 2019.
- [34] P. H. Geubelle and J. S. Baylor, "Impact-induced delamination of composites: a 2D simulation," *Composites Part B: Engineering*, vol. 29, pp. 589-602, 1998/09/01/ 1998.
- [35] B. Blackman, H. Hadavinia, A. J. Kinloch, and J. Williams, "The use of a cohesive zone model to study the fracture of fibre composites and adhesively-bonded joints," *International journal of fracture*, vol. 119, pp. 25-46, 2003.
- [36] R. Amacher, J. Cugnoni, J. Botsis, L. Sorensen, W. Smith, and C. Dransfeld, "Thin ply composites: Experimental characterization and modeling of size-effects," *Composites Science and Technology*, vol. 101, pp. 121-132, 2014.
- [37] L. P. Canal, M. Alfano, and J. Botsis, "A multi-scale based cohesive zone model for the analysis of thickness scaling effect in fiber bridging," *Composites Science and Technology*, vol. 139, pp. 90-98, 2017.
- [38] C. Blondeau, G. Pappas, and J. Botsis, "Influence of ply-angle on fracture in antisymmetric interfaces of CFRP laminates," *Composite Structures*, vol. 216, pp. 464-476, 2019.
- [39] A. Shirani and K. M. Liechti, "A calibrated fracture process zone model for thin film blistering," *International Journal of Fracture*, vol. 93, pp. 281-314, 1998.
- [40] K. M. Liechti, A. Shirani, R. G. Dillingham, F. J. Boerio, and S. M. Weaver, "Cohesive Zone Models of Polyimide/Aluminum Interphases," *J. Adhesion*, vol. 73, pp. 259-297, 2000.
- [41] W. Li and T. Siegmund, "Numerical study of indentation delamination of strongly bonded films by use of a cohesive zone model," *CMES: Computer Modeling in Engineering & Sciences*, vol. 5, pp. 81-90, 2004.
- [42] Y. Yan and F. Shang, "Cohesive zone modeling of interfacial delamination in PZT thin films," *International Journal of Solids and Structures*, vol. 46, pp. 2739-2749, 2009.
- [43] J.-Y. Faou, G. Parry, S. Grachev, and E. Barthel, "How does adhesion induce the formation of telephone cord buckles?," *Physical review letters*, vol. 108, p. 116102, 2012.
- [44] P. Lin, F. Shen, A. Yeo, B. Liu, M. Xue, H. Xu, *et al.*, "Characterization of interfacial delamination in multi-layered integrated circuit packaging," *Surface and Coatings Technology*, vol. 320, pp. 349-356, 2017.
- [45] S. Jain, K. M. Liechti, and R. T. Bonnecaze, "Cohesive zone models to understand the interface mechanics of thin film transfer printing," *Journal of Applied Physics*, vol. 125, p. 075301, 2019/02/21 2019.
- [46] K. L. Johnson, Kendall, K., and Roberts, A. D., "Surface energy and the contact of elastic solids," *Proceedings of the Royal Society of London. Series A, Mathematical and Physical Sciences*, vol. 324, pp. 301-313, 1971.

- [47] D. Maugis, "Adhesion of spheres: The JKR-DMT transition using a Dugdale model," *Journal of Colloid and Interface Science*, vol. 150, pp. 243-269, 1992.
- [48] J. Baney and C.-Y. Hui, "A cohesive zone model for the adhesion of cylinders," *Journal of adhesion science and technology*, vol. 11, pp. 393-406, 1997.
- [49] K.-S. Kim, R. McMeeking, and K. Johnson, "Adhesion, slip, cohesive zones and energy fluxes for elastic spheres in contact," *Journal of the Mechanics and Physics of Solids*, vol. 46, pp. 243-266, 1998.
- [50] D. Xu and K. M. Liechti, "Analytical and experimental study of a circular membrane in adhesive contact with a rigid substrate," *International Journal of Solids and Structures*, vol. 48, pp. 2965-2976, 2011.
- [51] J. W. Suk, S. R. Na, R. J. Stromberg, D. Stauffer, J. Lee, R. S. Ruoff, *et al.*, "Probing the adhesion interactions of graphene on silicon oxide by nanoindentation," *Carbon*, vol. 103, pp. 63-72, 7// 2016.
- [52] B. F. Sorensen and T. K. Jacobsen, "Determination of cohesive laws by the J integral approach," *Engineering Fracture Mechanics*, vol. 70, pp. 1841-1858, 2003.
- [53] L. Sorensen, J. Botsis, T. Gmür, and L. Humbert, "Bridging tractions in mode I delamination: Measurements and simulations," *Composites Science and Technology*, vol. 68, pp. 2350-2358, 2008/09/01/ 2008.
- [54] Y. Zhu, K. M. Liechti, and K. Ravi-Chandar, "Direct extraction of rate-dependent traction-separation laws for polyurea/steel interfaces," *International Journal of Solids and Structures*, vol. 46, pp. 31-51, 2009.
- [55] S. Gowrishankar, H. Mei, K. M. Liechti, and R. Huang, "A comparison of direct and iterative methods for determining traction-separation relations," *International Journal of Fracture*, vol. 177, pp. 109-128, 2012.
- [56] C. Wu, R. Huang, and K. M. Liechti, "Simultaneous extraction of tensile and shear interactions at interfaces," *Journal of the Mechanics and Physics of Solids*, vol. 125, pp. 225-254, 2019/04/01/ 2019.
- [57] B. N. Cox and D. B. Marshall, "The determination of crack bridging forces," *International Journal of Fracture*, vol. 49, pp. 159-176, June 01 1991.
- [58] C. Wu, S. Gowrishankar, R. Huang, and K. M. Liechti, "On determining mixed-mode traction–separation relations for interfaces," *International Journal of Fracture*, vol. 202, pp. 1-19, 2016.
- [59] N. Valoroso and L. Champaney, "A damage-mechanics-based approach for modelling decohesion in adhesively bonded assemblies," *Engineering Fracture Mechanics*, vol. 73, pp. 2774-2801, 2006.
- [60] D. Xie and A. M. Waas, "Discrete cohesive zone model for mixed-mode fracture using finite element analysis," *Engineering fracture mechanics*, vol. 73, pp. 1783-1796, 2006.
- [61] N. Chandra, H. Li, C. Shet, and H. Ghonem, "Some issues in the application of cohesive zone models for metal–ceramic interfaces," *International Journal of Solids and Structures*, vol. 39, pp. 2827-2855, 2002.

- [62] Y. Freed and L. Banks-Sills, "A new cohesive zone model for mixed mode interface fracture in bimetals," *Engineering Fracture Mechanics*, vol. 75, pp. 4583-4593, 2008.
- [63] S. Jain, S. R. Na, K. M. Liechti, and R. T. Bonnecaze, "A cohesive zone model and scaling analysis for mixed-mode interfacial fracture," *International Journal of Solids and Structures*, vol. 129, pp. 167-176, 2017/12/15/ 2017.
- [64] S. Jain, T. Yang, M. Negley, S. R. Na, K. M. Liechti, and R. T. Bonnecaze, "A parametric cohesive zone beam theory analysis of mixed-mode graphene transfer," *International Journal of Adhesion and Adhesives*, vol. 89, pp. 129-138, 2019.
- [65] M. F. Kanninen, "An augmented double cantilever beam model for studying crack propagation and arrest," *International Journal of Fracture*, vol. 9, pp. 83-92, 1973.
- [66] R. Olsson, "A simplified improved beam analysis of the DCB specimen," *Composites Science and Technology*, vol. 43, pp. 329-338, 1992.
- [67] F. Ozdil and L. Carlsson, "Beam analysis of angle-ply laminate DCB specimens," *Composites Science and Technology*, vol. 59, pp. 305-315, 1999.
- [68] A. De Morais, "Novel cohesive beam model for the End-Notched Flexure (ENF) specimen," *Engineering Fracture Mechanics*, vol. 78, pp. 3017-3029, 2011.
- [69] S. Bennati, P. Fisicaro, and P. S. Valvo, "An enhanced beam-theory model of the mixed-mode bending (MMB) test—Part II: Applications and results," *Meccanica*, vol. 48, pp. 465-484, 2013.
- [70] S. Bennati, P. Fisicaro, and P. S. Valvo, "An enhanced beam-theory model of the mixed-mode bending (MMB) test—Part I: Literature review and mechanical model," *Meccanica*, vol. 48, pp. 443-462, 2013.
- [71] S. Jain, S. R. Na, K. M. Liechti, and R. T. Bonnecaze, "Characteristic scaling equations for softening interactions between beams," *International Journal of Fracture*, vol. 201, pp. 1-9, 2016.
- [72] J. Xie, A. M. Waas, and M. Rassaian, "Closed-form solutions for cohesive zone modeling of delamination toughness tests," *International Journal of Solids and Structures*, vol. 88, pp. 379-400, 2016.
- [73] L. K. Jain, K. A. Dransfield, and Y.-W. Mai, "Effect of reinforcing tabs on the mode I delamination toughness of stitched CFRPs," *Journal of composite materials*, vol. 32, pp. 2016-2041, 1998.
- [74] S. Marzi, A. Rauh, and R. M. Hinterhölzl, "Fracture mechanical investigations and cohesive zone failure modelling on automotive composites," *Composite Structures*, vol. 111, pp. 324-331, 2014.
- [75] T. Brussat, S. Chiu, and S. Mostovoy, "Fracture mechanics for structural adhesive bonds," LOCKHEED-CALIFORNIA CO BURBANK1977.
- [76] R. Joannic and B. Chartier, "A device for utilising the DCB test geometry at intermediate opening velocities," *Le Journal de Physique IV*, vol. 10, pp. Pr9-249-Pr9-254, 2000.
- [77] G. Hug, P. Thevenet, J. Fitoussi, and D. Baptiste, "Effect of the loading rate on mode I interlaminar fracture toughness of laminated composites," *Engineering Fracture Mechanics*, vol. 73, pp. 2456-2462, 2006.

- [78] V. Sundararaman and B. D. Davidson, "An unsymmetric double cantilever beam test for interfacial fracture toughness determination," *International journal of solids and structures*, vol. 34, pp. 799-817, 1997.
- [79] H. Cao and A. Evans, "An experimental study of the fracture resistance of bimaterial interfaces," *Mechanics of materials*, vol. 7, pp. 295-304, 1989.
- [80] P. Charalambides, H. Cao, J. Lund, and A. Evans, "Development of a test method for measuring the mixed mode fracture resistance of bimaterial interfaces," *Mechanics of materials*, vol. 8, pp. 269-283, 1990.
- [81] H. Wang and T. Vu-Khanh, "Use of end-loaded-split (ELS) test to study stable fracture behaviour of composites under mode II loading," *Composite Structures*, vol. 36, pp. 71-79, 1996.
- [82] R. Mahajan and K. Ravi-Chandar, "An experimental investigation of mixed-mode fracture," *International Journal of fracture*, vol. 41, pp. 235-252, 1989.
- [83] F. Xiao, C.-Y. Hui, and E. Kramer, "Analysis of a mixed mode fracture specimen: the asymmetric double cantilever beam," *Journal of Materials Science*, vol. 28, pp. 5620-5629, 1993.
- [84] J. R. Reeder and J. H. Crews, "Mixed-mode bending method for delamination testing," *AIAA Journal*, vol. 28-7, pp. 1270-1276, 1989.
- [85] G. Fernlund and J. Spelt, "Mixed-mode fracture characterization of adhesive joints," *Composites science and technology*, vol. 50, pp. 441-449, 1994.
- [86] B. D. Davidson and F. O. Sediles, "Mixed-mode I–II–III delamination toughness determination via a shear–torsion–bending test," *Composites Part A: Applied Science and Manufacturing*, vol. 42, pp. 589-603, 2011/06/01/ 2011.
- [87] Z. Suo, G. Bao, and B. Fan, "Delamination R-curve phenomena due to damage," *Journal of the Mechanics and Physics of Solids*, vol. 40, pp. 1-16, 1992.
- [88] B. F. Sørensen and T. K. Jacobsen, "Large-scale bridging in composites: R-curves and bridging laws," *Composites Part A: Applied Science and Manufacturing*, vol. 29, pp. 1443-1451, 1998.
- [89] J. E. Lindhagen and L. A. Berglund, "Application of bridging-law concepts to short-fibre composites Part 1: DCB test procedures for bridging law and fracture energy," *Composites Science and Technology*, vol. 60, pp. 871-883, 2000.
- [90] T. Jacobsen and B. F. Sørensen, "Mode I intra-laminar crack growth in composites—modelling of R-curves from measured bridging laws," *Composites Part A: Applied Science and Manufacturing*, vol. 32, pp. 1-11, 2001.
- [91] B. Sørensen and T. Jacobsen, "Delamination of fibre composites: determination of mixed mode cohesive laws," *Compos Sci Tech*, vol. 69, pp. 445-56, 2009.
- [92] G. A. Pappas and J. Botsis, "Variations on R-curves and traction-separation relations in DCB specimens loaded under end opening forces or pure moments," *International Journal of Solids and Structures*, 2019.
- [93] K. M. Liechti and W. G. Knauss, "Crack propagation at material interfaces: I. Experimental technique to determine crack profiles," *Experimental Mechanics*, vol. 22, pp. 262-269, 1982.

- [94] Y. S. Chai and K. M. Liechti, "Biaxial loading experiments for determining interfacial fracture toughness," *Journal of Applied Mechanics*, vol. 58, pp. 680-687, 1991.
- [95] A. W. Mello and K. M. Liechti, "A piezoelectric biaxial loading device for interfacial fracture experiments," *Experimental Mechanics*, vol. 44, pp. 495-501, 2004.
- [96] H. K. Singh, A. Chakraborty, C. E. Frazier, and D. A. Dillard, "Mixed mode fracture testing of adhesively bonded wood specimens using a dual actuator load frame," *Holzforschung*, vol. 64, pp. 353-361, 2010.
- [97] W. G. Knauss and G. U. Losi, "Crack Propagation in a Nonlinearly Viscoelastic Solid With Relevance to Adhesive Bond Failure," *Journal of Applied Mechanics*, vol. 60, pp. 793-801, 1993.
- [98] P. Rahul-Kumar, A. Jagota, S. J. Bennison, S. Saigal, and S. Muralidhar, "Polymer Interfacial Fracture Simulations using Cohesive Elements," *Acta Materialia*, vol. 47, pp. 4161-4169, 1999.
- [99] P. G. de Gennes, "Soft Adhesives," *Langmuir*, vol. 12, pp. 4497-4500, 1996/01/01 1996.
- [100] L. Kogan, C. Y. Hui, and A. Ruina, "Theory of Chain Pull-Out and Stability of Weak Polymer Interfaces. 1," *Macromolecules*, vol. 29, pp. 4090-4100, 1996/01/01 1996.
- [101] D. B. Xu, C. Y. Hui, E. J. Kramer, and C. Creton, "A micromechanical model of crack growth along polymer interfaces," *Mechanics of Materials*, vol. 11, pp. 257-268, 1991/05/01/ 1991.
- [102] C. M. Landis, T. Pardoen, and J. W. Hutchinson, "Crack velocity dependent toughness in rate dependent materials," *Mechanics of Materials*, vol. 32, pp. 663-678, Nov 2000.
- [103] K. Liechti and J.-D. Wu, "Mixed-mode, time-dependent rubber/metal debonding," *Journal of the Mechanics and Physics of Solids*, vol. 49, pp. 1039-1072, 2001/05/01/ 2001.
- [104] C. Xu, T. Siegmund, and K. Ramani, "Rate-dependent crack growth in adhesives: I. Modeling approach," *International Journal of Adhesion and Adhesives*, vol. 23, pp. 9-13, 2003/01/01/ 2003.
- [105] X. Zhang, Y.-W. Mai, and R. G. Jeffrey, "A cohesive plastic and damage zone model for dynamic crack growth in rate-dependent materials," *International Journal of Solids and Structures*, vol. 40, pp. 5819-5837, 2003/10/01/ 2003.
- [106] G. Giambanco and G. Fileccia Scimemi, "Mixed mode failure analysis of bonded joints with rate-dependent interface models," *International Journal for Numerical Methods in Engineering*, vol. 67, pp. 1160-1192, 2006/08/20 2006.
- [107] S. Marzi, O. Hesebeck, M. Brede, and F. Kleiner, "A Rate-Dependent Cohesive Zone Model for Adhesively Bonded Joints Loaded in Mode I," *Journal of Adhesion Science and Technology*, vol. 23, pp. 881-898, 2009/01/01 2009.
- [108] I. K. Mohammed, M. N. Charalambides, and A. J. Kinloch, "Modeling the effect of rate and geometry on peeling and tack of pressure-sensitive adhesives," *Journal of Non-Newtonian Fluid Mechanics*, vol. 233, pp. 85-94, 2016/07/01/ 2016.

- [109] M. Rakestraw, M. Taylor, D. Dillard, and T. Chang, "Time dependent crack growth and loading rate effects on interfacial and cohesive fracture of adhesive joints," *The Journal of Adhesion*, vol. 55, pp. 123-149, 1995.
- [110] A. Ghatak, K. Vorvolakos, H. She, D. L. Malotky, and M. K. Chaudhury, "Interfacial rate processes in adhesion and friction," *Journal of Physical Chemistry B*, vol. 104, pp. 4018-4030, 2000.
- [111] D. E. Spearot, K. I. Jacob, and D. L. McDowell, "Non-local separation constitutive laws for interfaces and their relation to nanoscale simulations," *Mechanics of Materials*, vol. 36, pp. 825-847, 2004/09/01/ 2004.
- [112] G. Lake and A. Thomas, "The strength of highly elastic materials," *Proceedings of the Royal Society of London. Series A. Mathematical and Physical Sciences*, vol. 300, pp. 108-119, 1967.
- [113] R. Rivlin and A. G. Thomas, "Rupture of rubber. I. Characteristic energy for tearing," *Journal of polymer science*, vol. 10, pp. 291-318, 1953.
- [114] L. Freund, "Characterizing the resistance generated by a molecular bond as it is forcibly separated," *Proceedings of the National Academy of Sciences*, vol. 106, pp. 8818-8823, 2009.
- [115] H. A. Kramers, "Brownian motion in a field of force and the diffusion model of chemical reactions," *Physica*, vol. 7, pp. 284-304, 1940.
- [116] A. Zhurkov, "Kinetic concept of the strength of solids," *Int. J. Fract. Mech.*, vol. 1, pp. 311-323, 1965.
- [117] G. Bell, "Models for the specific adhesion of cells to cells," *Science*, vol. 200, pp. 618-627, 1978.
- [118] E. Evans and K. Ritchie, "Dynamic strength of molecular adhesion bonds," *Biophysical journal*, vol. 72, pp. 1541-1555, 1997.
- [119] L. B. Freund, "Brittle crack growth modeled as the forced separation of chemical bonds within a K-field," *Journal of the Mechanics and Physics of Solids*, vol. 64, pp. 212-222, 2014.
- [120] Y. Wei, "A stochastic description on the traction-separation law of an interface with non-covalent bonding," *Journal of the Mechanics and Physics of Solids*, vol. 70, pp. 227-241, 2014.
- [121] J. Qian, J. Lin, G.-K. Xu, Y. Lin, and H. Gao, "Thermally assisted peeling of an elastic strip in adhesion with a substrate via molecular bonds," *Journal of the Mechanics and Physics of Solids*, vol. 101, pp. 197-208, 2017/01/01/ 2017.
- [122] W. Kuhn and F. Grün, "Beziehungen zwischen elastischen Konstanten und Dehnungsdoppelbrechung hochelastischer Stoffe," *Kolloid-Zeitschrift*, vol. 101, pp. 248-271, 1942.
- [123] Y. Mao, B. Talamini, and L. Anand, "Rupture of polymers by chain scission," *Extreme Mechanics Letters*, vol. 13, pp. 17-24, 2017.
- [124] Y. Mao and L. Anand, "A theory for fracture of polymeric gels," *Journal of the Mechanics and Physics of Solids*, vol. 115, pp. 30-53, 2018.
- [125] B. Li and N. Bouklas, "A variational phase-field model for brittle fracture in polydisperse elastomer networks," *International Journal of Solids and Structures*, vol. 182, pp. 193-204, 2020.

- [126] Y.-M. Liang and K. Liechti, "Toughening mechanisms in mixed-mode interfacial fracture," *International journal of solids and structures*, vol. 32, pp. 957-978, 1995.
- [127] S. C. Hung and K. M. Liechti, "An evaluation of the Arcan specimen for determining the shear moduli of fiber-reinforced composites," *Experimental Mechanics*, vol. 37, pp. 460-468, 1997.
- [128] A. J. Kinloch and J. G. Williams, "Crack blunting mechanisms in polymers," *Journal of Materials Science*, vol. 15, pp. 987-996, 1980.
- [129] J. G. Williams and J. M. Hodgkinson, "Crack-blunting mechanisms in impact tests on polymers," *Proceedings of the Royal Society of London. A. Mathematical and Physical Sciences*, vol. 375, pp. 231-247, 1981.
- [130] J. G. Swadener, Liechti, K. M., and de Lozanne, A. L., "The intrinsic toughness and adhesion mechanism of a glass/epoxy interface," *Journal of Mechanics and Physics of Solids*, vol. 47, pp. 223-258, 1999.
- [131] P. Hänggi, P. Talkner, and M. Borkovec, "Reaction-rate theory: fifty years after Kramers," *Reviews of modern physics*, vol. 62, p. 251, 1990.
- [132] V. Tvergaard and J. W. Hutchinson, "On the toughness of ductile adhesive joints," *Journal of the Mechanics and Physics of Solids*, vol. 44, pp. 789-800, 1996/05/01/ 1996.
- [133] L. H. Sharpe, "The interphase in adhesion," *The Journal of Adhesion*, vol. 4, pp. 51-64, 1972.
- [134] L. T. Drzal, "The interphase in epoxy composites.," *Advances in Polymer Science*, pp. 75, 1-32, 1986.
- [135] S. K. Khanna, K. Paruchuri, P. Ranganathan, S.B. Yedla, and R.M. Winter, "Investigation of Nanomechanical Properties of the Interphase in Glass Fiber Reinforced Polyester Composite Using Nanoindentation," *ASME Journal of Engineering Materials and Technology*, vol. 125, pp. 90-96, 2003.
- [136] J. G. D. Williams, M. E.; James, M. R.; Morris W. L., "Properties of the interphase in organic matrix composites," *Material Science and Engineering A*, pp. 126, 305-312, 1990.
- [137] Z. Liu, J. A. Moore, and W. K. Liu, "An extended micromechanics method for probing interphase properties in polymer nanocomposites," *Journal of the Mechanics and Physics of Solids*, vol. 95, pp. 663-680, 10// 2016.
- [138] J. Neggers, J. P. M. Hoefnagels, O. Van Der Sluis, and M. G. D. Geers, "Multi-scale experimental analysis of rate dependent metal–elastomer interface mechanics," *Journal of the Mechanics and Physics of Solids*, vol. 80, pp. 26-36, 2015.
- [139] T. Yang, X. Yang, R. Huang, and K. M. Liechti, "Rate-dependent Traction-separation Relations for a Silicon/Epoxy Interface Informed by Experiments and Bond Rupture Kinetics," *Journal of the Mechanics and Physics of Solids*, 2019/06/25/ 2019.
- [140] A. P. Wiita, S. R. K. Ainavarapu, H. H. Huang, and J. M. Fernandez, "Force-dependent chemical kinetics of disulfide bond reduction observed with single-molecule techniques," *Proceedings of the National Academy of Sciences*, vol. 103, pp. 7222-7227, 2006.

- [141] T. Ackbarow, X. Chen, S. Keten, and M. J. Buehler, "Hierarchies, multiple energy barriers, and robustness govern the fracture mechanics of alpha-helical and beta-sheet protein domains," *Proc Natl Acad Sci U S A*, vol. 104, pp. 16410-5, Oct 16 2007.
- [142] I. V. Pobelov, K. P. Lauritzen, K. Yoshida, A. Jensen, G. Mészáros, K. W. Jacobsen, *et al.*, "Dynamic breaking of a single gold bond," *Nature Communications*, vol. 8, p. 15931, 07/17/online 2017.
- [143] J. W. Hutchinson and Z. Suo, "Mixed Mode Cracking in Layered Materials," *Advances in Applied Mechanics*, vol. 29, pp. 63-191, 1991.
- [144] J. Williams, "End corrections for orthotropic DCB specimens," *Composites Science and Technology*, vol. 35, pp. 367-376, 1989.
- [145] M. Conroy, A. Kinloch, J. Williams, and A. Ivankovic, "Mixed mode partitioning of beam-like geometries: A damage dependent solution," *Engineering Fracture Mechanics*, vol. 149, pp. 351-367, 2015.
- [146] Z. Ouyang and G. Li, "Nonlinear interface shear fracture of end notched flexure specimens," *International Journal of Solids and Structures*, vol. 46, pp. 2659-2668, 2009.
- [147] C. L. Chow, C. W. Woo, and J. L. Sykes, "On the determination and application of COD to epoxy-bonded aluminum joints," *Journal of Strain Analysis for Engineering Design*, vol. 14, pp. 37-42, 1979.
- [148] M. R. Vanlandingham, R. F. Eduljee, and J. W. Gillespie Jr., "Relationships between stoichiometry, microstructure, and properties for amine-cured epoxies," *Journal of Applied Polymer Science*, vol. 71, pp. 699-712, 1999.

Vita

Tianhao Yang was born in Liaoning Province, China. In 2010, he entered Beihang University and received his B.E. degree in 2014. In September 2014, he joined the University of Texas at Austin pursuing a Ph.D. degree in Aerospace Engineering.

Permanent email: thyang@utexas.edu

This dissertation was typed by Tianhao Yang.